INVESTIGATION OF PHASE TRANSFORMATIONS IN TRANSITION METAL DICHALCOGENIDES DURING SYNTHESIS AND POST GROWTH

A dissertation presented to

The Academic Faculty

by

Neha Kondekar

In Partial Fulfillment

of the Requirements for the Degree

Doctor of Philosophy

in Materials Science and Engineering

Georgia Institute of Technology

August 2020

INVESTIGATION OF PHASE TRANSFORMATIONS IN TRANSITION METAL DICHALCOGENIDES DURING SYNTHESIS AND POST-GROWTH

Approved by:

Dr. Matthew McDowell, Advisor
School of Materials Science and Engineering,
Georgia Institute of Technology

Dr. Faisal Alamgir
School of Materials Science and Engineering,
Georgia Institute of Technology

Dr. Eric Vogel
School of Materials Science and Engineering,
Georgia Institute of Technology

Dr. Mark Losego
School of Materials Science and Engineering,
Georgia Institute of Technology

Dr. Satish Kumar
George W. Woodruff School of
Mechanical Engineering,
Georgia Institute of Technology

Date Approved: July 14, 2020

This thesis is dedicated to my Aai, Pappa, Rohit, and friends who became family

Acknowledgments

They say it's not the destination, but the journey that you remember. For me, the journey to this dissertation was a very happy one, made possible with the love and support of innumerous mentors, friends, colleagues and family. First and foremost, I would like to thank my advisor, Dr. Matthew McDowell, for his guidance through the process. As one of his first graduate students, I was fortunate to learn with the guru in the lab. It was an exciting adventure to grow as a curious but tactful scientist with him beside me. As I complete my journey, I hope a few things that I learned from Matt will always stay with me – curiosity bundled with enthusiasm, patience for a thorough study, and most importantly, getting your hands dirty. His approach of questioning results again and again, not rushing to conclusions, is something that I have worked hard to emulate. Whenever I did something new in the lab, I remember being less excited about the results and more afraid that I won't be able to answer all of Matt's pointed questions regarding what happened and why. This rigorous training that I received while working with Matt and the McDowell lab prepares me for a responsible scientist career wherever I go next. Thank you, Matt!

Secondly, I would like to thank Dr. Garimella or as he likes to be called, Dr. G. Very serendipitously, we met at a graduate student recruitment session and that started the journey of me seeking his advice, we discussed not just graduate school but also the journey after. From aiming to be a professional baker to a technology person, Dr. Garimella patiently sat through my rants as I went through the different phases of graduate school and I would like to say a big 'Thank You' to him for that. He always made time to ask me how I was doing, both mentally and academically, which made me realize that even the busiest of people can take out time for those they care about.

I would also like to thank my committee members – Dr. Eric Vogel, Dr. Faisal Alamgir, Dr. Mark Losego, and Dr. Satish Kumar who took out time from their busy schedules to give very valuable advice throughout the process.

I would like to share a very famous duplet in Hindi written by the poet, Kabir :

गुरू गोविन्द दोऊ खड़े, काके लागूं पांय।

बलिहारी गुरू अपने, गोविन्द दियो बताय।।

Translated, it means – "If both God and my teacher were standing in front of me, I would seek blessings from my teacher first; because without the teacher, I would never know who God was." I am fortunate to have been mentored by Matt, Dr. G, my committee members, and several more people, with whom even a short interaction would have been helpful.

It goes without saying that where I am today would not have been possible had my family not believed in me. My father, Dr. Pravin Kondekar is a Professor himself, and his support through my Ph.D. program was immense. He kept me motivated by being on top of the latest materials research news and would often share the applications engineered with the help of graduate research. He would always be the one to ask what excites me about my research and that 'self-reflection' helped me understand the contribution of graduate research to the society and kept me spirited through the ups and downs. My mother, Dr. Pratibha Kondekar somehow always knew what I was up to, even when she was ~8000 miles away. There was not a day when she didn't inquire about my meals, my gym, and my 'me' time. When things in the lab wouldn't work out, my mom would have a new solution to get me up and going. My brother, Rohit Kondekar, always had my back, be it preparing for job-interviews or finding the new diet plan; even when figuring out how to deal with very tricky situations at work. Shilali and Shibali kept me sane by cooking all the delicious eating Indian food during those relaxing road-trips.

The long and arduous journey would not have been possible without friends by my side in the lab. Firstly, Matthew Boebinger, who started in the lab with me, helped me immensely. From setting up the lab, preparing for qualifying exams to discussing the right way of filling out graduation forms, I am grateful to Matthew for his help all along. Pralav mastered all the characterization tools at Georgia Tech and sped up my experiments, while also being my idea bouncing wall. Both of us came up with several ideas for tech both inside and outside the lab and I am thankful to have had a buddy like him for the same. Lan, who joined the lab as a sophomore was immensely resourceful for all the CAD, 3D printing, and Python coding. She would always be a call or text away for any electronic design need and I am very grateful to her for taking time from her busy undergrad schedule for that. Francisco always had things to talk about, be it politics, graduate student life, or the latest Twitter trend, and I cherish all the coffee chats I have had with him. Sang with his jokes and great boba tea recommendations was an amazing buddy to discuss the 'Ph.D. after-life' with. Trevor and Miranda diligently helped me with experiments in the lab. Michael, Akila, Jack, Jared, Stephanie, Kelsey, Tim, Emily and Tom, all became a part of the McDowell lab family and I will miss all the fun activities we had as a group.

The long technical journey to writing this dissertation would not have been possible without several state-of-the-art equipment that the Institute of Electronics and Nanotechnology (IEN) at Georgia Tech offered. Walter Henderson and Rathi helped me start my long journey with the XPS and always answered my never-ending questions patiently. David Tavakoli and his Sublime-donut Fridays as well as the occasional baked treats and Tiramisu kept me cheerful throughout. David also helped me with all kinds of XRD and I am grateful to have learnt a lot about crystal analysis from him. Todd Walters had the best jokes to make the 5,000+ hours spent at the IEN memorable and training on the SEM will always be memorable. Eric Woods was never

annoyed by my weekend tool repair requests, Mengkun Tian always had the sleight of hand to fix the STEM's focus; them along with Erin Prowett, Charlie Suh and Charlie Turgeon always managed to find solutions to get the tools up and running.

Last but not the least, I would like to thank my friends who became my family in this new country, new place. The road-trips with Hamza and the Mstreet family let me explore this beautiful country in a very short time. Hamza was never more than a phone call away, be it for coffee chats or heated debates. Supriya and Shreya were the best roommates that I have ever had and, from dancing to cooking together, I will cherish all the memories I made with them. Pedro, Jyotsna, Ming, Apaar, Girish, Rakshith, and Namrata always had the best hangouts plans and our weekends were packed with fun activities. Sampada, Aman, Diksha, Rohit, Sharvaree and Sameer kept me sane with their conversations even though they were 8000 miles away. I was fortunate to be surrounded by amazing friends who supported each other in the best and worst of times.

I am happy to have made so many memories and I will miss this Georgia Tech family.

Table of Contents

List of Figures

List of Symbols and Abbreviations

MoS_2	Molybdenum Disulfide
WS_2	Tungsten Disulfide
NiS_x	Nickel Sulfide
µm	Micrometer or 10^{-6} m
nm	Nanometer or 10^{-9} m
Å	Angstrom or 10^{-10} m
eV	Electron Volt
BE	Binding Energy
TMDC	Transition Metal Dichalcogenide
XPS	X-ray Photoelectron Spectroscopy
TEM	Transmission Electron Microscopy
STEM	Scanning Transmission Electron Microscopy
GIXRD	Grazing Incidence X-ray Diffraction
PL	Photoluminescence
ΔG_f^o	Gibbs Free Energy of Formation
ΔG_{rxn}	Gibbs Free Energy of Reaction
TGA	Thermogravimetric Analysis
DSC	Differential Scanning Calorimetry
AFM	Atomic Force Microscopy
DFT	Density Functional Theory
FFT	Fast Fourier Transform
SAED	Selected Area Electron Diffraction

HER	Hydrogen Evolution Reaction
HDS	Hydrodesulfurization
γ	Surface Energy
χ	Electronegativity
CVD	Chemical Vapor Deposition
LPCVD	Low Pressure Chemical Vapor Deposition
APCVD	Atmospheric Pressure Chemical Vapor Deposition
MoO_3	Molybdenum Oxide
S	Elemental Sulfur
$(NH_4)_2MoS_4$ or ATM	Ammonium Tetra-thio Molybdate
PTAS	Perylene-3,4,9,10-tetracarboxylic acid tetrapotassium salt
$F_{16}CuPc$	Copper(II) hexadecafluoro phthalocyanine
vdWE	van der Waals Epitaxy
vdWR	van der Waals Rheotaxy

Summary

Transition metal dichalcogenides (TMDCs) are promising candidates for use in beyond-Moore electronics, photovoltaics, sensing, and energy storage devices. The highly anisotropic crystal structure of TMDCs is characterized by chemically active edge sites and relatively inert basal plane layers, which are bonded to each other by weak van der Waals forces. To tailor TMDCs' electronic, chemical and optical properties for different applications, careful control of their crystallographic orientation, composition, and layer thickness is required. While the commercialization of electronic devices requires uniform TMDC growth over large areas, enhancement of catalytic activity necessitates that as many edge sites as possible are exposed to the surface. To ensure optimal operation of TMDC-based transistors, engineering the interface with different contact metals (including at elevated temperatures and in the presence of surface oxides) is important to reduce the resulting contact resistance across the interface. Furthermore, the presence of other metals can influence the final morphology of TMDC crystallites during their synthesis and alter their resulting properties. In all these cases, to obtain optimal optoelectronic and catalytic properties, understanding the role of metal/TMDC interfaces in controlling the properties and performance of these materials is crucial.

The first part of this dissertation discusses experiments in which MoS_2 crystals with different crystallographic surface orientations are interfaced with other materials (Li, Ge or Ag). It then proceeds to explore – using data obtained from *in situ* X-ray photoelectron spectroscopy (XPS) – the interfacial phase transformations that occur during interface formation. Reactions across horizontally aligned MoS_2 layers are compared with vertically aligned MoS_2 layers (i.e., predominantly edge sites exposed). An important finding is that the edge sites feature a native surface oxide that prevents the reaction between Ge and MoS_2, but the same oxide is not sufficient

to prevent the reactive Li species from reducing MoS_2 to Mo metal. Ag shows very little reaction with either of the samples. The material with exposed basal planes features surface defects (vacancies, steps, ledges etc.) that act as sites for the onset of interfacial transformations, which occur readily with Ge and Li. Using the Ni-MoS_2 system, further investigations were performed on the influence of elevated temperatures on interfacial reactions. Overall, the results show that MoS_2 orientation affects the extent of interfacial reaction in the case of some contact materials, but not in others; furthermore, the varied chemistry of different MoS_2 surfaces likely contributes to these differences.

Next, the influence of Ni on the growth of crystalline MoS_2 is investigated using *in situ* transmission electron microscopy (TEM). An amorphous MoS_2 precursor is annealed on different substrates – including on Ni films of varying thicknesses – to nucleate and grow polycrystalline MoS_2. The results indicate that Ni assists lateral growth of MoS_2 crystals, as they end up being approximately 10 times larger than those without Ni. Other transition metals (Fe, Cu and Co) were also examined, but only Ni caused a significant change in the MoS_2 crystallite size. Based on *in situ* TEM observations and other *ex situ* results, it is postulated that this result is due to Ni atoms or NiS_x clusters increasing the mobility of Mo and S atoms at the MoS_2 edge planes, which enables faster edge growth rates.

In the third section, knowledge gained from the fundamental *in situ* studies of the Ni-MoS_2 system is used to selectively pattern MoS_2 growth during chemical vapor deposition (CVD) onto Si substrates featuring 300 nm SiO_2 on their surface. Growth of MoS_2 on thin (~2 nm) patterned Ni films but not on the surrounding SiO_2/Si substrate was observed. Au thin films were also used to seed growth of MoS_2 crystals, but once nucleated, MoS_2 crystals preferred to grow over the SiO_2/Si substrate. Utilizing the different interactions of MoS_2 with these different materials during

growth, crystalline MoS_2 was selectively grown over Ni regions which in turn were contacted by Au regions. This configuration was utilized to demonstrate fabrication of transistor structures. Further studies are needed to explore the effects of Ni dopants on the electronic properties of patterned devices.

Overall, this dissertation elucidates the dynamic structural and phase evolution of MoS_2 crystals both during synthesis, as well as upon interfacing the as-grown crystallites with different materials. The combination of *in situ* and *ex situ* measurements provide important observations of the dynamic phase transformations during and after growth. These results help to fill a knowledge gap that exists regarding the engineering of TMDC materials: prior work has provided understanding of the atomic-scale structure of active TMDCs for catalysis and optoelectronic applications, but the best pathways to synthesize and engineer these materials are not always clear. These findings provide a basis for future engineering of TMDC crystal size and morphology via addition of different transition metals as well as stabilization of phases across TMDC heterointerfaces. This phase engineering could be important for a range of applications, including catalysis and next-generation electronic and optical devices.

CHAPTER 1. Introduction and Motivation

1.1 Layered Transition Metal Dichalcogenides – Chemistry and Structure

Transition metal dichalcogenides (TMDCs) are layered MX_2 type compounds with M being a transition metal (Mo, W, etc.) and X a chalcogen atom (S, Se or Te).[1–3] Figure 1a shows the possible elemental building blocks of MX_2 type layered compounds.[1] One layer of M atoms is sandwiched between two layers of X atoms with the layers loosely bonded through van der Waals forces but strong, covalent bonds within each layer.[3–6] The two most common crystal structures these TMDCs form with are trigonal prismatic (2H) or octahedral (1T), as shown in Figure 1(b).[7] The 2H phase features an ABA stacking sequence, while the 1T phase features an ABC stacking sequence. The dimerized 1T' phase forms under the application of strain to the 1T phase.[8] Usually, the thermodynamically stable phase is 2H while 1T and 1T' are metastable.[7] The unique anisotropy in the chemical bonding allows for easy separation of monolayer TMDCs which have significantly different properties from their 3D or bulk counterparts due to quantum confinement effects.[9] For bulk TMDCs, indirect band gaps are predicted to be 1.23 eV (MoS_2), 1.09 eV ($MoSe_2$), 1.32 eV (WS_2), 1.21 eV (WSe_2) correspondingly, while their monolayer counterparts undergo an indirect to direct band gap transition increasing the band gap range to 1.5–2.0 eV.[10–12] Graphene, on the other hand, does not feature a sizable band gap for logic applications and needs surface functionalization to introduce a band gap of 0.25 eV,[13,14] which in turn degrades the electronic properties by introducing defects.[15] The exceptional ability to engineer optoelectronic properties by altering physicochemical structure has made TMDCs attractive for a wide range of applications, including nanoelectronics[3,9], energy storage,[16] photovoltaics,[17,18] water-splitting,[19] hydrodesulfurization catalysts,[20] and biosensing.[21]

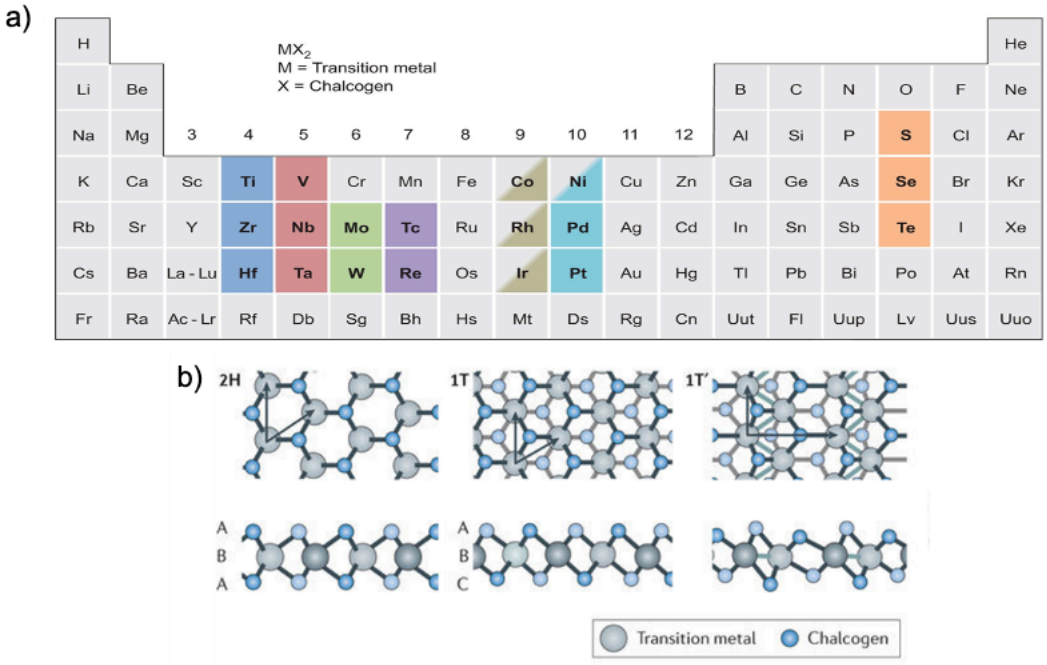

Figure 1 Different types and crystallographic structure of transition metal dichalcogenides a)The transition metals and the three chalcogen elements that predominantly crystallize in those layered structures are highlighted in the periodic table. Adapted with permission from Chhowalla et al.[1] b) c-axis and [11$\bar{2}$0] section view of single-layer TMD in 2H, 1T, and 1T' coordination. Atom color code: Grey, metal; Blue, chalcogen. Adapted with permission from reference[7]. Copyright 2017, Springer Nature.

TMDCs can exhibit different electronic properties including metallic, semiconducting, insulating, and even superconducting depending on the combination of M and X atoms.[7] For MoS_2, the focus of this thesis, the 2H phase, is semiconducting, while the 1T phase is metallic. 1T MoS_2 has been shown to form upon Li intercalation into the lattice and can be reversed to its 2H phase easily under irradiation. This is illustrated in Figure 2a below.[22] The difference in band structure of MoS_2 for the two phases is shown in Figure 2b, showing the transition from a semiconducting (2H) phase to a metallic (1T) phase.[23]

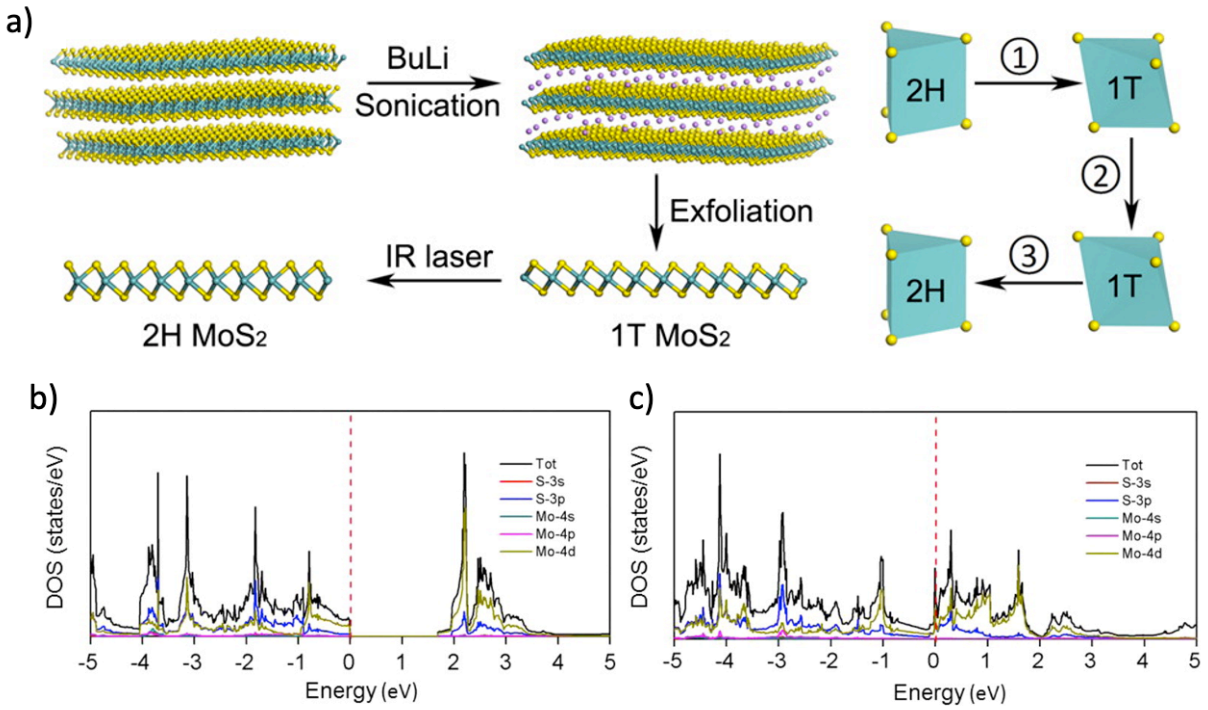

Figure 2 2H to 1T phase transition in MoS_2 a) Intercalation of n-butyl lithium into 2H MoS_2 layers leads to the formation of 1T MoS_2. This change can be reversed by irradiation. Adapted with permission from reference [22]. Copyright 2015, American Chemical Society. b) Total and orbital-projected density of states (DOS) of unfunctionalized 2H-MoS_2 (b) and 1T-MoS_2 (c). The Fermi level (dashed line) is set as zero. Adapted with permission from reference[23]. Copyright 2015 American Chemical Society.

An additional benefit of TMDCs is the ability to engineer the band gap based on the layer thickness of the crystal. Figure 3 shows the calculated indirect-to-direct band gap transition going from bulk to monolayer MoS_2 as shown in a study by Splendiani *et al.*[24] The same study shows experimental results that confirm DFT predictions and report a dramatic increase in photoluminescence (PL) intensity for monolayer MoS_2. This thickness-dependent behavior is starkly different from Si nanoparticles, which show PL enhancement but only for particles less than 2-3 nm in size.[25,26] This ability to engineer a sizable band gap by adjusting the layer thickness allows for the possibility of the creation of large-length-scale yet extremely thin and highly sensitive photosensors, detectors, and photovoltaics.

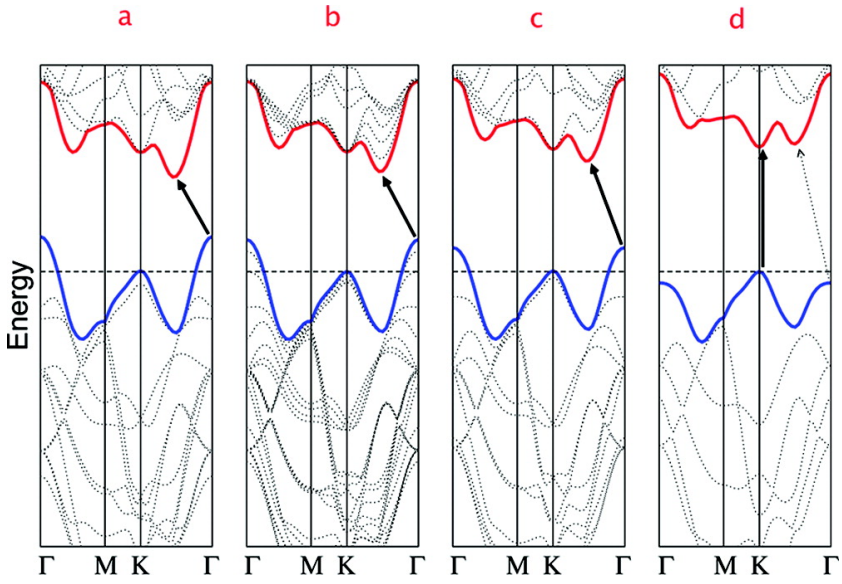

Figure 3 Calculated band structures of (a) bulk MoS_2, (b) quadrilayer MoS_2, (c) bilayer MoS_2, and (d) monolayer MoS_2 The solid arrows indicate the lowest energy transitions. Bulk MoS_2 is characterized by an indirect band gap. The direct excitonic transitions occur at high energies at K point. With reduced layer thickness, the indirect band gap becomes larger, while the direct excitonic transition barely changes. For monolayer MoS_2 in (d), it becomes a direct band gap semiconductor. This dramatic change of electronic structure in monolayer MoS_2 can explain the observed jump in monolayer photoluminescence efficiency. Adapted with permission from reference[24]. Copyright 2010 American Chemical Society.

A typical single crystal of TMDC has relatively inert basal planes (due to weak van der Waals interactions between layers) and highly reactive edge sites (due to the presence of dangling bonds). This is illustrated in Figure 4 for a MoS_2 crystal. The layers are so weakly bonded that simple mechanical exfoliation using Scotch tape can pull them apart, resulting in crystals with thicknesses down to a single monolayer (6.2 Å). The edge sites, however, are inevitably present in any bulk or synthesized MoS_2 crystal and feature dangling bonds or defective states, such as S vacancies, and are completely different from basal planes in terms of chemical reactivity. This chemical and structural anisotropy inherent to a single TMDC crystal also allows another knob for property tuning.

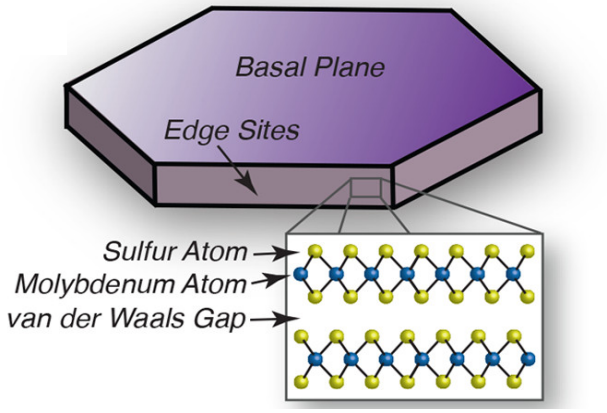

Figure 4 Schematic of a single MoS_2 crystal showing the position of basal planes and edge sites The magnified inset shows the layered S–Mo–S stacking for a crystal with the hexagonal 2H crystal structure.

Jaramillo *et al.*[28] showed that the catalytic efficiency for water splitting reactions for MoS_2 nanoparticle scales with the total length of edge planes on the crystals (Figure 5); thus the edge sites are catalytically active while the basal planes are not. While bulk MoS_2 is a poor catalyst; few-layered MoS_2 nanoparticles are cheap alternatives to Pt catalysts while also being photoactive. The water-splitting catalyst can be intentionally engineered to have a surface exposed with reactive edge sites to facilitate the hydrogen evolution reaction (HER).[29–32] On the other hand, a nanoelectronic FET device can be designed to feature a monolayer TMDC crystal with only the basal plane exposed in the channel, thereby featuring relatively few dangling bonds that contribute to interface states and electron traps, but chemical bonding across its edge sites allowing for good electron injection from metal contacts.[33] This will be discussed in greater detail in Section 1.2.2.

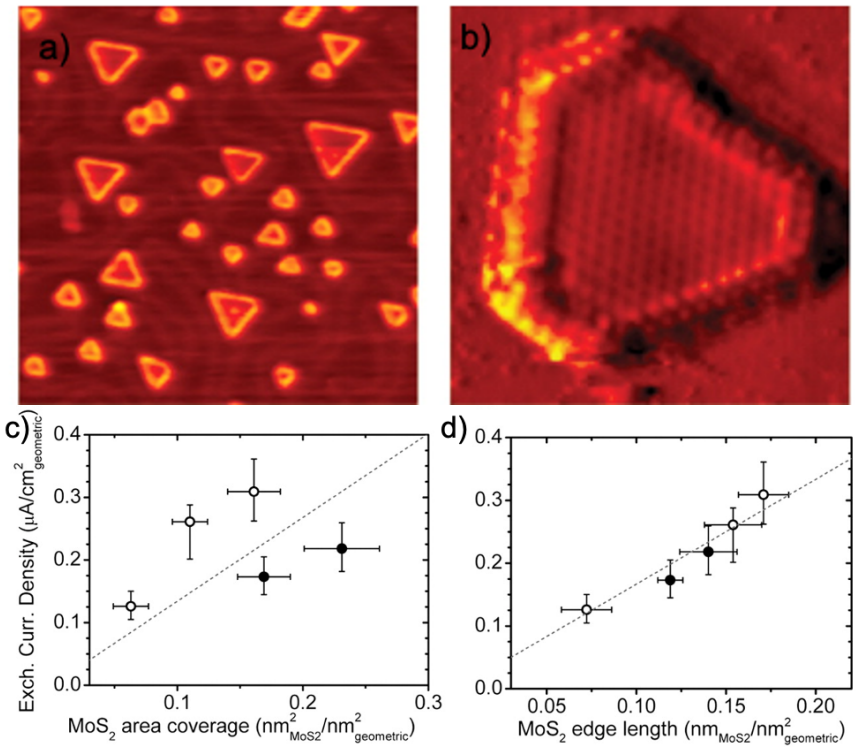

Figure 5 A series of STM images of MoS_2 nanoparticles on Au(111) The particles exhibit the typical polygon morphology with conducting edge states. a) MoS_2 nanoparticles annealed to 550°C (470 Å by 470 Å, 1.2 nA, 1.9 V). b) Atomically resolved MoS_2 particle. C) Exchange current density versus c) MoS_2 area coverage and d) MoS_2 edge length. The exchange current density does not correlate with the area coverage of MoS_2, whereas it shows a linear dependence on the MoS_2 edge length. Adapted with permission from reference[28]. Copyright 2007, American Association for the Advancement of Science.

Like other thin films, TMDCs naturally feature defects including vacancies, dislocations, and grain boundaries.[34,35] However, since the surface area to volume ratio is very high for thin TMDCs, the defects have a more substantial influence on its properties and hence special attention needs to be paid to engineering them appropriately. For instance, S-vacancies often exist as charged trap states which serve as scattering centers and degrade electronic properties in TMDCs.[36] McDonnell *et al.* showed that defects alone can cause MoS_2 thin films to exhibit both n-type and p-type doping on the same sample due to variation in S-vacancy concentration.[37] The same vacancies also induce new photoluminescence (PL) peaks and enhance PL intensities while

also enhancing catalytic activity for water-splitting reactions.[37] Ferromagnetic effects resulting from anion and cation vacancy clusters have also been reported in MoS_2.[38] These defects are also responsible for the initiation of MoS_2 oxidation by -O or -OH substitution of S vacancies resulting in gradual aging and degradation of the MoS_2 crystal.[39] CVD-grown MoS_2 crystals show a higher defect density and hence lower electron mobility than exfoliated crystals.[40]

To add to the variety of applications available using TMDCs, the possibility of growing van der Waals (vdW) heterostructures like MoS_2/WS_2, MoS_2/Graphene/hBN and several more has been explored as well, opening a whole new dimension of TMDC engineering.[41–44] Figure 6 shows the concept of van der Waals heterostructures to be analogous to the stacking of Legos.[45] Without the need for lattice matching, van der Waals epitaxy has enabled the growth of a variety of vdW heterostructures, which combine the benefits of each material. Furthermore, Liu *et al.* showed that MoS_2 crystals grown through van der Waals epitaxy on substrates like epitaxial graphene/SiC showed lower defect density than both CVD MoS_2 grown on SiO_2 as well as exfoliated MoS_2.[46] Several other papers have grown MoS_2-based heterostructures for improved vertical tunneling transistors and photodetectors.[41,44,47]

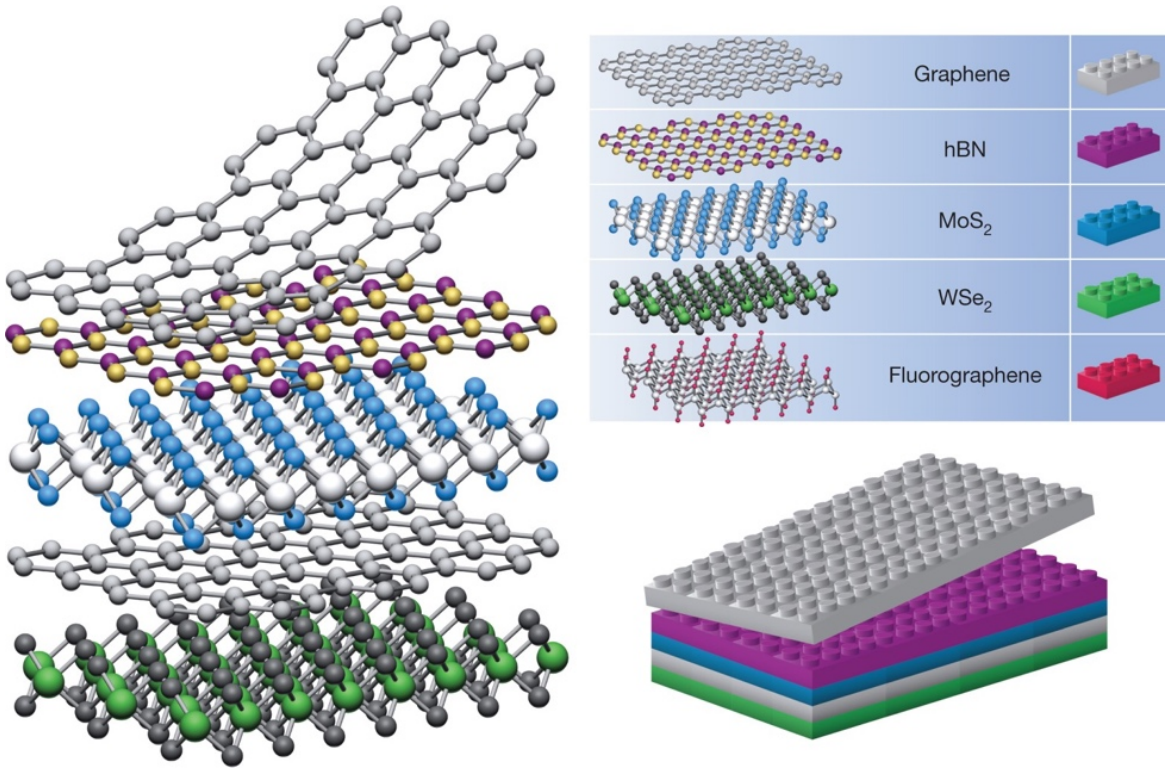

Figure 6 2D crystals can be considered to be analogous to Lego blocks (right panel) This allows for the construction of a variety of heterostructures with no lattice matching requirement – van der Waals epitaxy. Adapted with permission from reference [45]. Copyright 2013 Springer Nature.

The optical, electronic, and mechanical properties of TMDCs are strongly controlled by their physical and chemical structure. Figure 7 illustrates the complex but nuanced relationship between different variables required to achieve the optimal performance of TMDC devices. The chemical structure of TMDCs is controlled by the nature of MX_2 material, the synthesis method, and the growth substrate as well as its physical structure (crystallographic anisotropy, phase, and layer thickness). These two interrelated variables further control the resulting optoelectronic, catalytic and energy storage properties of the TMDC devices. Finally, the conditions in which a device is used (high temperature, or under corrosive conditions) also affect the operation of these TMDC devices and hence their optimal performance requires an understanding of all these different variables together. The research in this dissertation aims to investigate structural and

chemical transformations at TMDC interfaces using *in situ*, real-time characterization and aims to contribute to a greater understanding of the importance of controlling synthesis and operation of devices to achieve this optimal performance. Specific focus areas are growth and crystallization kinetics, transformations on interfacing with metals, and epitaxial growth of TMDC heterostructures.

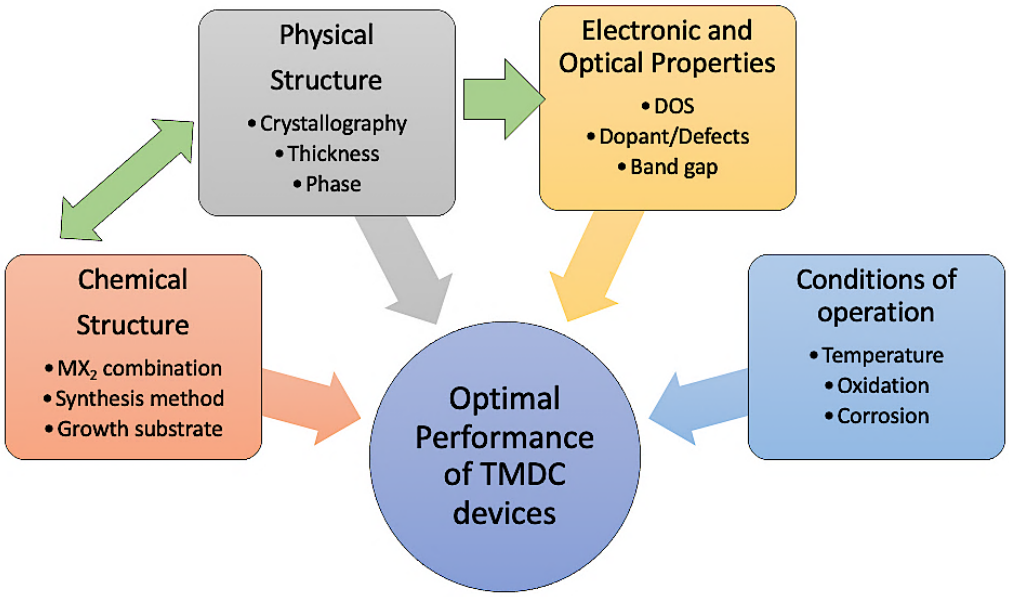

Figure 7 Structure-property correlation for TMDCs An illustration highlighting the relationship between the physical and chemical structure of TMDCs and the electronic, optical, and catalytic properties, as well as the stability conditions during operation of these devices, made with different TMDCs.

1.2 Layout of This Dissertation

This dissertation is arranged in the following manner. In Chapter 2, experimental methods utilized for the work are discussed, including both the *in situ* study of interface evolution as well as *ex-situ* analysis of MoS_2 thin films on metal and other 2D material substrates. In Chapter 3, the role of chemical bonding across contact metals and different MoS_2 surface sites (basal vs. edge) is investigated at room and elevated temperatures using *in situ* XPS and TEM techniques. In Chapter

4, the role of metal atoms (Ni, Co, Fe, Cr, and Cu) on the growth trajectory of MoS_2 nanocrystals is investigated using a combination of *in situ* and *ex situ* techniques. In Chapter 5, this knowledge is used to enable the selective growth of MoS_2 channels using patterned metal thin films, demonstrating the bottom-up synthesis of MoS_2 transistor structures without any photolithography steps between the MoS_2 channel growth and the metal contacts deposition. Finally, Chapter 6 will summarize conclusions and promising areas for future work.

CHAPTER 2. Experimental Methods

2.1 Introduction

This chapter describes experimental procedures utilized to gather data for this dissertation. Included are descriptions of TMDC synthesis and device fabrication, *in situ* X-ray photoelectron spectroscopy (XPS), *in situ* heated transmission electron microscopy (TEM) and photolithography, along with other procedures. Additional details about other experimental methods are found in the relevant chapters.

2.2 TMDC Synthesis and Device Fabrication

2.2.1 Preparation of Vertically and Horizontally Aligned MoS_2 Samples

Two types of MoS_2 samples with different crystallographic orientations were fabricated for the experiments discussed in Section 3. Horizontally aligned or basal plane exposed MoS_2 samples were produced by exfoliating few-layer films from bulk MoS_2 single crystals (SPI Supplies). These samples were mechanically exfoliated with Scotch tape and then transferred to a sample holder for XPS experiments and attached with carbon tape. This procedure was performed inside an Ar-filled glove box (MBraun) to minimize surface oxidation. For fabrication of vertically aligned or edge site exposed thin films of MoS_2, a heavily doped, p-type Si wafer (Addison) with orientation was first cleaned by sonicating in a 1:1:1 volumetric mixture of isopropanol, acetone, and methanol. A 50 nm thick film of Mo was evaporated onto the wafer using a Denton electron-beam evaporator at a pressure of 10^{-5} Torr. A relatively low deposition rate of 0.1 Å/s was used to ensure minimal surface roughness. This Mo thin film was then sulfided in an LPCVD setup under inert Ar gas with an elemental sulfur source as reported in a study by Kong *et al.*[29] In a single-zone tube furnace (Lindberg, Blue M), a ceramic boat containing 2.0 g of elemental sulfur powder

(Sigma Aldrich) was placed inside a 2.54 cm diameter quartz tube. The sulfur source material was located 16.5 cm upstream from the center of the tube. Si wafer samples coated with Mo were placed in the tube at the center of the heating zone. The system was sealed and evacuated to a pressure of 25 mTorr, and it was then flushed with Ar at a flow rate of 110 sccm for 15 min before heating. The chamber was then ramped to 700 °C over 15 min, during which Ar continuously flowed at a rate of 50 sccm. After this heating period, the furnace temperature was held at 700 °C for an additional 30 min under the same Ar flow. It was then naturally cooled to room temperature under 110 sccm Ar flow. During this process, the sulfur source material vaporized and reacted with the Mo to yield MoS_2 thin films with vertically aligned layers. The furnace was vented, and the samples were immediately transferred to the glove box to minimize surface oxidation. Characterization of the surface of these MoS_2 thin films revealed the presence of a SiO_x interfacial layer, which will be discussed subsequently. This layer was removed by etching the as-synthesized material in 2 vol % HF (aqueous solution) for 1 min. As discussed later, this etching step did not affect the surface chemistry of the MoS_2 material itself.

2.2.2 Atmospheric Pressure Chemical Vapor Deposition (APCVD)

While mechanical exfoliation allows for ease of production of high-quality TMDC single crystals, large-scale and controlled growth of TMDC single crystals requires a CVD process. The CVD process works through a vapor phase reaction between TMDC precursors like MoO_3 and S for MoS_2 at elevated temperature and atmospheric pressure. The reaction product or MoS_2 then condenses onto a substrate (SiO_2/Si, sapphire) and results in nucleation of MoS_2. Several studies have investigated the influence of parameters like the growth temperature, gas flow rate, and precursor concentration to allow for optimized and tailored TMDC growth. The most common

growth process for MoS_2 single crystals entails the use of MoO_3 and elemental S powder which are heated to 700 ºC and ~180 ºC, respectively, using a two-zone furnace configuration as shown in Figure 8. To allow for use of low precursor concentrations for selective growth of MoS_2 in Section 4, ~10 µg of MoO_3 powder was spread onto a SiO_2/Si substrate placed next to the patterned substrates.

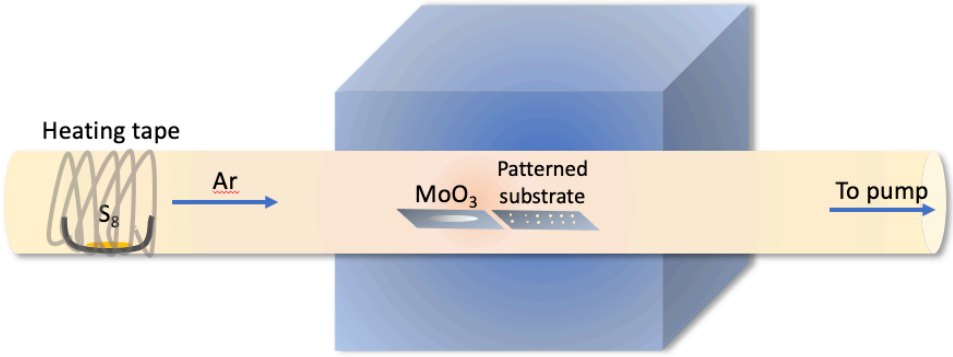

Figure 8 Atmospheric pressure CVD setup used to selectively grow MoS_2 on patterned substrates in Chapter 5.

Maintaining the pressure at 1 atm is required to allow for very slow and controlled vaporization of the precursors since the monolayer growth is sensitive to the precursor concentration above the substrate. However, it is important to use a vacuum pump to evacuate the hazardous H_2S and S vapor which are present in the tube. To maintain the pressure while still evacuating the tube downstream, a specialized setup had to be designed. A pressure manometer was placed upstream and connected to a Mass Flow Controller (MFC) which was operated as a pressure controller. These two were connected to an external computer which allowed for control of the flow rate and operating pressure of the gas. Downstream of the quartz tube, three valves were installed. Two modes of evacuating this tube were needed – one which allowed for the evacuation of the tube to a lower vacuum level (~10 mTorr) at the beginning of the CVD process and the other which could allow for atmospheric pressure operation while still evacuating the tube

of its gaseous by-products. Evacuating the tube to a lower vacuum level was important to remove the moisture and oxygen residues in the tube before beginning the CVD process.

2.2.3 Spin coating – Solution-processed MoS_2 growth

MoS_2 thin films for *ex situ* characterization were prepared on Si (111) wafers with 200 nm thermally grown SiO_2. The substrates were cleaned before the spin coating procedure by sonication in acetone, methanol, and 2-propanol for 20 min each. Additionally, the surface was rendered hydrophilic by performing an RCA clean (1:1:6 mixture of $NH_4OH/H_2O_2/H_2O$) for 10 min at 70 °C. A 5 wt % solution of ammonium tetrathiomolybdate ($(NH_4)_2MoS_4$, abbreviated ATM) in NMP solution was spin-coated onto the different samples with a spin speed of 3000 rpm. ATM is a solid precursor that decomposes to form crystalline MoS_2 on annealing to 300-800 ºC as discussed later in Section 4. For the experiments in this section (with Ni addition), Ni thin films were first deposited *via* e-beam evaporation of 5 or 30 nm Ni thin films onto the SiO_2/Si substrates. Samples were immediately dried in a vacuum oven at 60 °C to remove NMP residue. The samples were then placed in a 1 in. quartz tube and evacuated to a base pressure of 25 mTorr to remove all residual moisture and oxygen. Ar/H_2 gas then flowed over the sample at a flow rate of 100 sccm and the furnace was brought up to a pressure of 1800 mTorr. Under this gas flow, the samples were heated to varying temperatures between 600 - 900 °C with a heating ramp rate of 100 ºC/min.

2.3 *In situ* X-ray Photoelectron Spectroscopy (XPS)

As discussed in the introduction, thin films, especially few-layer TMDCs, have a high surface-to-volume ratio. A material's surface is the point of interaction with the external environment and other materials, and thus sees the onset of failures or degraded performance.

Hence, surface-sensitive chemical analysis to understand and maintain the efficacy of surface engineering strategies is necessary.

XPS, also known as electron spectroscopy for chemical analysis (ESCA), is a technique for analyzing the surface chemistry of a material. XPS can measure the elemental composition, atomic ratio, chemical state, and electronic state of the elements within a material. XP spectra are obtained by irradiating a solid material surface with a beam of X-rays. This results in the emission of core electrons as shown in Figure 9, which are then collected by a detector. The kinetic energy (KE) of the electron depends upon the photon energy (hν) and the binding energy (BE) of the electron (*i.e.,* the energy required to remove the electron from the surface). The detector measures the KE of the photoelectrons which is related to the BE of these electrons when present in the solid. Peaks appear in the spectrum from atoms emitting electrons of a particular characteristic energy. While the X-rays have a penetration depth up ~100 μm, photoelectrons that can escape the material with characteristic kinetic energies (without inelastic collisions altering the energies) are limited to the near-surface region (~1-10 nm).[48] XPS requires high vacuum (~10^{-8} millibar) or ultra-high vacuum (UHV; <10^{-9} millibar) conditions to allow for a larger mean free path for these photoelectrons, although a current area of development is ambient-pressure XPS, in which samples are analyzed at pressures of a few tens of millibar. The energies and intensities of the photoelectron peaks enable identification and quantification of all surface elements (except hydrogen).

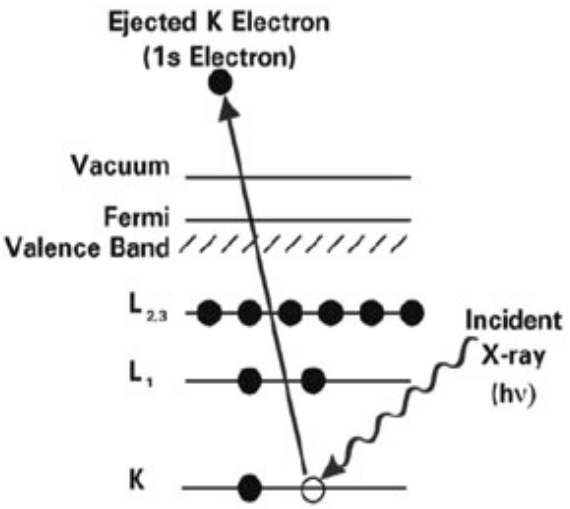

Figure 9 Mechanism of photoemission during XPS analysis. The photoemission process involved for XPS surface analysis. The discs represent electrons and the bars represent energy levels within the material being analyzed. The equation governing the process is: KE = hν – BE. Reproduced from reference[49].

In this dissertation, *in situ* or real-time XPS investigation of interfacial reactions between different metal thin films and the MoS_2 surface was carried out. This allows for surface-sensitive investigation of interfacial transformations or reactions taking place across the metal-MoS_2 interface. For this purpose, the methodology reported by Wenzel *et al.* was used.[50] An *L*-shaped sample holder was utilized to allow for the sputter deposition of the three different target materials (Li, Ag, and Ge) onto the MoS_2 samples within the XPS, as illustrated in Figure 10. The holder is designed so that the Ar sputter gun within the XPS chamber can be used to deposit the target material. The holder features an 85° angle between the upright portion of the holder and the horizontal surface. The target material was attached to the upright end of the holder using conductive carbon tape, and a MoS_2 sample was affixed to the horizontal surface of the sample holder 0.5 mm away from the target material. All of these steps were carried out inside an Ar glove box to prevent exposure to the atmosphere. The holder assembly was then placed within a vacuum transfer stage, which was evacuated inside the antechamber of the glove box. It was then transferred directly into the XPS analysis chamber. This procedure is useful for minimizing further

oxidation of the MoS_2, and it is necessary for preventing oxidation/nitridation of Li metal during experiments that utilize Li.

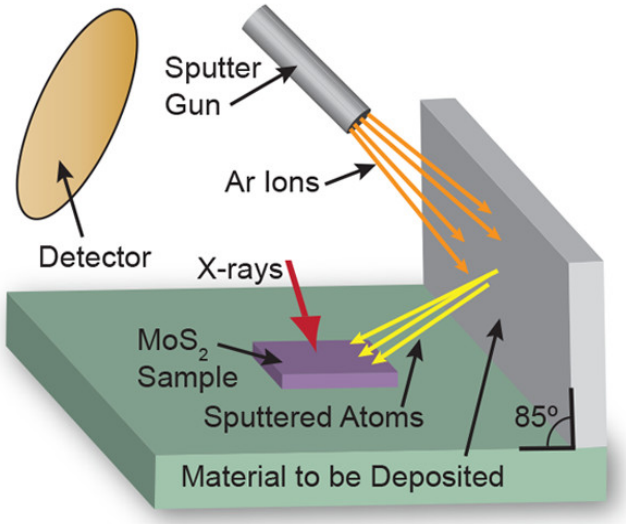

Figure 10 In situ XPS setup. The L-shaped holder to perform in situ XPS features the material to be deposited on the upright section while the MoS_2 sample is attached to the flat bottom. Ar^+ plasma is used to sputter deposit the material onto MoS_2 on the surface followed by detecting the chemical peaks using the XPS detector.

Each of the target materials to be deposited was prepared in different ways. For Li experiments, a piece of Li foil (Sigma-Aldrich, 99.9% purity) was mechanically cleaned with Teflon inside the glove box to remove surface oxides before being attached to the L-shaped sample holder. For Ag experiments, Ag film (~300 nm thick) was thermally evaporated (Denton Explorer) onto a piece of Si wafer substrate using Ag source material (99.99% purity). For Ge experiments, Czochralski-grown, undoped, Ge single crystals (MTI Corp.) were cleaned with deionized water to dissolve the surface oxide[51] and then transferred to the glove box and attached to the sample holder. Once the sample holder was inside the XPS instrument, the sputter deposition of the target material was carried out with Ar^+ ions using an acceleration voltage of 3.0 keV and an ion current of 9.0 μA. The ion beam was rastered over a rectangular area of 4 × 2 mm. The angle between the horizontal sample and the sputter gun was 32°, and the sputter gun was directed at a position ~2

mm above the surface of the MoS_2 sample. This resulted in sputtering of the target material in a cone-shaped plume, with the plume oriented to partially deposit onto the MoS_2 sample. Due to the nature of this sputtering process, the thickness of the sputtered thin films varied with position on the surface of the MoS_2 samples. For repeatable measurements, it was necessary to always collect XPS spectra from the same position on the sample. This position was chosen to be that at which the maximum amount of material was deposited (P_{max}). To find P_{max} for each target material, a set of XPS scans was performed over a wide area after sputtering. The point at which the integrated area of a given XPS peak from the deposited material was maximized was assumed to correspond to the thickest section of the deposited film. For these calibration experiments, sputtering was carried out onto a Si wafer instead of a MoS_2 sample to ensure minimal roughness. During the collection of *in situ* data, high-resolution photoelectron spectra were first obtained at the position P_{max} on the bare MoS_2 sample before any material was deposited. For Li deposition, a series of four sequential 3 min sputtering steps were performed, and a high-resolution photoelectron spectrum was collected after each sputtering step. For Ag, four sequential 1 min sputtering steps were performed, and for Ge, three 1 min sputtering steps and one 3 min sputtering step were used; high-resolution photoelectron spectra were similarly obtained. Deposition of ∼1−3 nm of the target material was found to allow for *in situ* determination of the interfacial reactions at the MoS_2 surface without fully attenuating the XPS signal from the MoS_2 buried under the deposited material. Since each deposited material attenuates MoS_2 photoelectrons to different degrees, the allowable deposition thickness is different for Li, Ge, and Ag. To determine the thickness of each material as a function of sputtering time, the three materials were sputtered *in situ* onto an MgO substrate, followed by the acquisition of Mg core-level spectra. MgO substrates were used because MgO is unreactive in contact with Li.[52,53] The MgO substrates (MTI Corp.) were single crystals with an

orientation, and they were plasma-cleaned (PE-25, Plasma Etch Inc.) for 10 min before deposition. The thickness of the deposited material was found by using the attenuation of the integrated intensity of the Mg 1s peak from the MgO substrate in conjunction with the electron-attenuation length (EAL) for the deposited material. The EAL values for each deposited material were obtained from the NIST standard database.[54] A Shirley background was used for fitting XPS peaks in these experiments, and the peak shapes used were 70% Gaussian/30% Lorentzian for all Mo 3d, S 2p, Li 1s, and Ge 3d peaks, while a Donjiac−Sunjic line shape was used for the asymmetric Ag 3d peak. For each high-resolution spectrum, the best fit for each data set was obtained as that with the minimum chi-square value.

2.4 *In situ* Transmission Electron Microscopy (TEM)

When Anton von Leeuwenhoek first used an optical microscope in 1676 to study microorganisms in his local pond, he was able to investigate real-time the blood flow in their capillaries and the movement of their muscle fibers.[55] That was a powerful tool to have and led him to be called as the 'father of microbiology'.[56] Today, the most powerful microscopes are TEMs which use electrons and feature a resolution 10,000 times higher than Leeuwenhoek's microscope (sub-Ångstrom) along with the ability to characterize materials with electron diffraction, energy dispersive spectroscopy (EDS), and electron energy loss spectroscopy (EELS), among other techniques. For atomically thin 2D TMDCs, a TEM is the ultimate tool to study their structural, chemical, and morphological properties.[56] A TEM operates by transmitting a high-voltage electron beam (200-300 kV) through a thin sample and using the transmitted electrons to form a real-space image or a diffraction pattern. Depending on the sample material, the specimen usually must be thinner than a few hundred nanometers to be electron transparent. Contrast is generated in TEM

in a few different ways. One mechanism is mass-thickness contrast: heavier atoms and thicker regions scatter electrons more effectively, which results in lower intensity in a bright-field image. Another contrast mechanism is diffraction contrast, which is generated when imaging crystalline samples; this contrast arises from scattering at high angles due to electron diffraction from a lattice. Finally, phase contrast can be used to obtain high-resolution lattice images. This contrast results from phase shifts and interference of the diffracted electron beam. Recent advances in the field allow for use of specialized holders to bias, heat, or cool TEM samples inside the microscope as well as perform the imaging under gaseous (N_2, O_2, H_2S) and liquid conditions.[57]

In this dissertation, *in situ* heating in a TEM was performed with a DENSsolutions Wildfire S3 heating holder featuring Si-based heating chips with ~30 nm thick SiN_x windows, illustrated in Figure 11. Imaging was performed using an FEI Tecnai G2 F30 TEM operated at 300 kV. Before TEM imaging, samples were prepared using 5 wt. % solution of Ammonium Tetrathiomolybdate (or ATM - $(NH_4)_2MoS_4$) in *n*-methylpyrrolidone (NMP), which was sonicated for 20 min. This solution was drop-cast onto the heating chip and dried under vacuum. To investigate the influence of Ni, 5 or 30 nm Ni films were e-beam evaporated onto the heating chips before drop-casting the precursor solution. For all TEM heating experiments, samples were first heated within the TEM from 25 to 100 °C with a ramp rate of 1 °C/s. The temperature was maintained at 100 °C within the TEM for 15 min to remove organic residues. Following this, the sample was heated from 100 to 900 °C in increments of 100 °C with a ramp rate of 100 °C/min. After each 100 °C heating increment, the sample temperature was held constant for 10 min during TEM imaging. Each *in situ* heating experiment was repeated at least twice. Circumferential integration of SAED patterns was carried out using the MATLAB script DiffractIndex. The electron beam dose rate for images at the highest magnification images was 478 mA/cm^2 (measured using the fluorescent screen).

Images were recorded using a Gatan OneView CCD camera with an exposure time of ~1 s, and the video was recorded at five frames per second. Experiments to investigate the influence of electron beam irradiation and growth conditions (vacuum *vs* Ar/H_2) were performed separately and are described in the relevant sections.

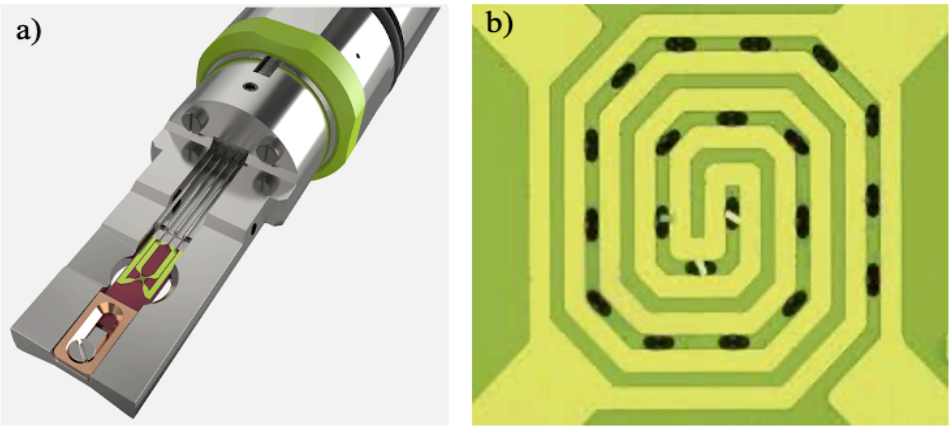

Figure 11 In situ TEM heating setup a) The single-tilt TEM holder (DENSsolutions) is used to load a specialized TEM grid with a MEMS chip featuring Pt electrodes on a SiNx membrane which allows for heating of the grid to temperatures up to 1300 ℃. b) A close-up view of the MEMS heating chip showing viewing holes in the SiN_X membrane. All the TEM imaging is carried over one or several of these viewing holes. Adapted from reference[58].

2.5 Sample Preparation and Imaging with Scanning Transmission Electron Microscopy (STEM)

For STEM imaging, MoS_2 films grown on SiO_2/Si substrates with 5 nm Ni were transferred onto holey SiN_x TEM grids (Ted Pella, Inc.) using a poly(methyl methacrylate) (PMMA)-assisted transfer method. The PMMA solution (MicroChem A9) was spun coat onto a prepared *ex situ* MoS_2 film on a 5 nm Ni/SiO_2/Si substrate at 4000 rpm for 45 s. Concentrated KOH solution (30 wt %) was used to etch the SiO_2 layer, resulting in a floating PMMA−MoS_2 stack which was then scooped onto the TEM grid. The TEM samples were rinsed with DI water multiple times and cleaned in acetone for 1 h at 80 °C, followed by annealing under Ar/H_2 atmosphere at 300 °C for 4 h. Annular dark-field (ADF) STEM imaging was conducted with a Hitachi HD-2700 STEM

equipped with a third-order spherical-aberration corrector. Imaging was performed at an acceleration voltage of 80 kV with a spatial resolution of 0.15 Å. The collection angle range was 40−210 mrad with a convergent angle of 22.5 mrad. EDS hypermaps were obtained using a Bruker system. A sum spectrum was captured for each pixel, which was then averaged to yield spectral intensity. The scan time was 20 min.

2.6 Photolithography for Selective Growth and Nanoelectronics Fabrication

Lithography, which means 'writing on a stone,' was originally used by Alois Senefelder in 1796 as a way to mass-produce textbooks using hydrophobic ink on a hydrophilic surface. Photolithography, now using photons, is based on the same principle of transferring patterns from a photomask to a photosensitive substrate. The pattern transfer is so powerful that features down to ~1 μm (lateral) can be transferred to the substrates. Figure 12 illustrates the basic principle of photolithography where a positive (negative) light-sensitive polymer or photoresist is removed (not removed). [59] This results in transferring different thin film patterns onto the substrate which is essential when fabricating nanoelectronics devices. In the complex CMOS circuits that modern electronics use, a single wafer may go through different photolithography cycles up to 50 times.

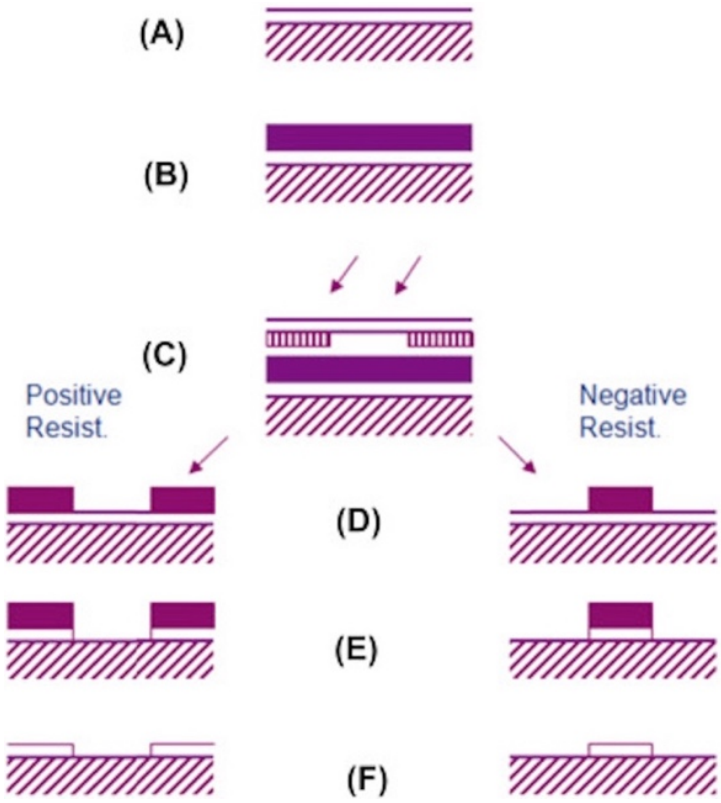

Figure 12 Schematic illustration of lithographic techniques to prepare nanomaterials in various feature sizes Adapted from reference[59].

This research uses the latest, state-of-the-art maskless aligner (MLA) where a CAD (Computer-Aided Design) design can be directly transferred onto the photoresist coated substrate without needing a photomask. Figure 13a shows the setup of the Heidelberg MLA setup consisting of a 385nm laser light (high resolution), a spatial light modulator to control light projection in the form of strips of the CAD pattern exposed at a time, a micromirror and lens setup along with a high-speed stage for X-Y translation.[59] By bypassing expensive and made-to-order photomasks, this MLA setup allows quick production of several different patterns ideal for early-stage and exploratory research like that done in this work. Several examples of patterns used during this research for deposition of several metal-TMDC thin films are shown in Figure 13b.

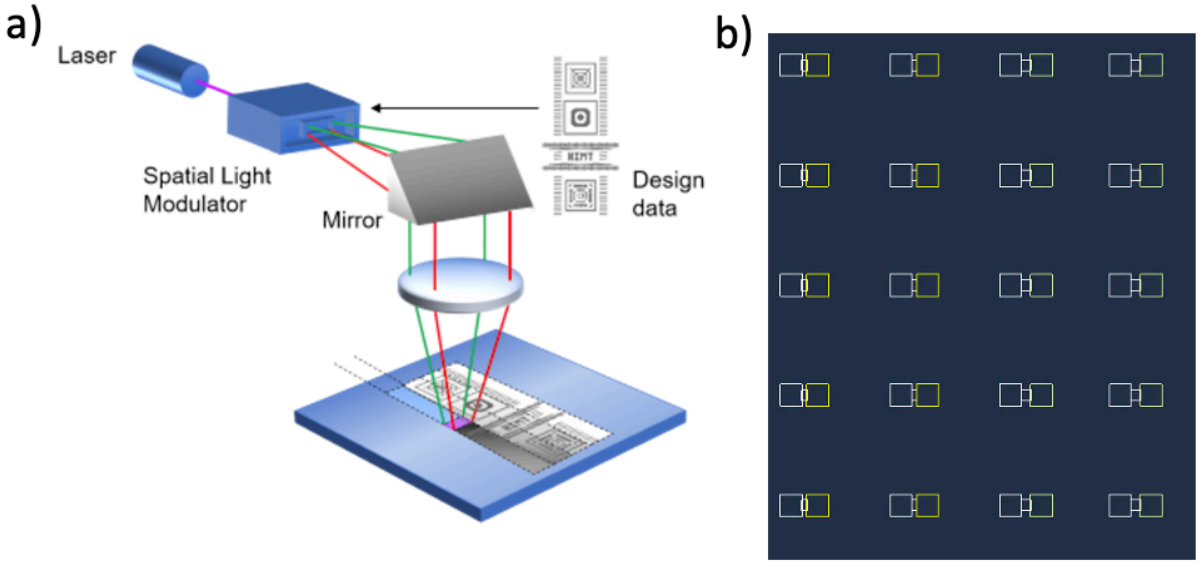

Figure 13 Maskless Aligner Photolithography Setup a) A combination of laser, Spatial Light Modulator (SLM), and a mirror assembly to transfer a CAD pattern directly onto a substrate with photoresist. Adapted from reference[59]. b) Several CAD designs used in this thesis to produce different metallic thin film patterns on which TMDC thin films were subsequently grown.

2.6.1 Other Ex Situ Characterization Techniques

Several other characterization methods including Raman spectroscopy, grazing incidence X-ray diffraction (GIXRD), and atomic force microscopy (AFM) were also used and the details of their use are discussed in the relevant sections of the subsequent chapters.

CHAPTER 3. Interfacial Phase Transformations across Crystallographically Controlled MoS_2 Surface Sites

3.1 Introduction

MoS_2 has shown promise as a low power, ultra-fast, and atomically thin channel. However, contact resistance can manifest due to the presence of a large Schottky barrier height between contact metals like Au or Pt and MoS_2 as shown in Figure 14.[33]

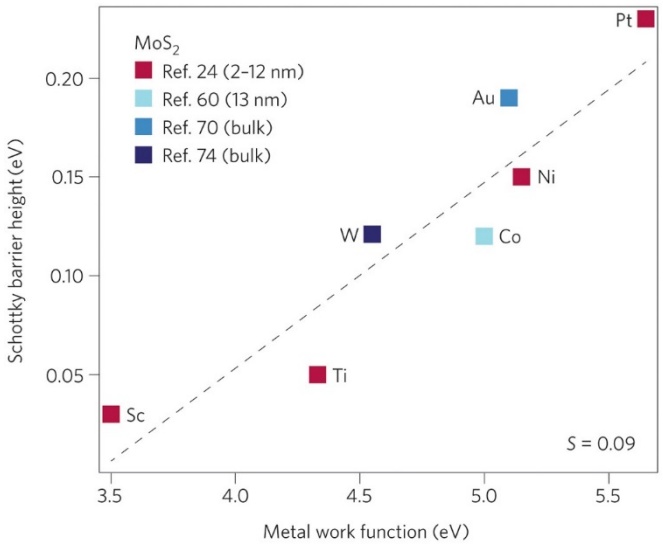

Figure 14 Schottky barrier heights for different metals with MoS_2 as reported in literature Adapted with permission from reference[33]. Copyright 2015 Springer Nature.

The Schottky barrier limits electron injection into the channel and hence the performance of the device. Careful engineering of the metal-MoS_2 interface is needed to minimize contact resistance. Allain *et al.*[33] showed using DFT calculations that ordinarily, the contact between metal and bulk semiconductors like Si results in the formation of covalent bonds between the metal and Si (as shown in Figure 15a-b). This results in an inherent Schottky barrier which can be overcome through three charge injection mechanisms as shown – thermionic emission, thermionic field emission, and tunneling. However, a lack of dangling bonds on the basal plane of MoS_2 results in

the formation of an additional tunneling barrier (Figure 15c-d) due to the presence of the vdW gap and the absence of bonding between Au and MoS_2. This results in thermionic emission as the only source of charge injection, which is the cause for the resulting high contact resistance. Metals like Ti, on the other hand, react with MoS_2 to form covalent bonds at the interface and show significantly improved charge injection because of the elimination of the vdW gap.

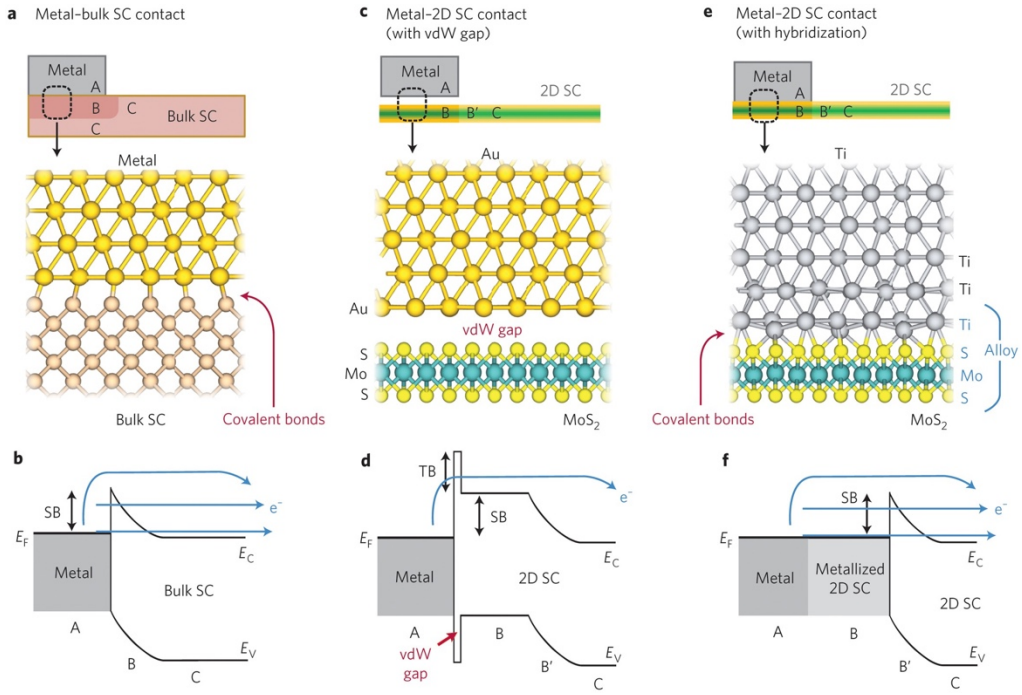

Figure 15 Predicted nature of bonding across MoS_2 metal interface. Schematic (a) and corresponding band diagram (b) of a typical metal/bulk SC interface. c,d, Metal/2D SC interface with vdW gap (for example, Au–MoS_2 contact). e,f, Metal/2D SC interface with hybridization (for example, Ti–MoS_2 contact, where MoS_2 under the contact is metalized by Ti). E_F, E_C and E_V represent the Fermi level of the metal, and the conduction and valence bands of the 2D SC, respectively. TB and SB indicate the tunnel and Schottky barrier heights, respectively. A, B, B′ and C represent different regions in the current path from the metal to the SC. The blue arrows in b, d , and f represent the different injection mechanisms. From top to bottom: thermionic emission, thermionic field emission and field emission (tunneling). In d, only thermionic emission is available. Adapted with permission from reference[33]. Copyright 2015 Springer Nature.

Previous studies have demonstrated that contacting the edges of graphene[60] and TMDC[39] crystals results in shorter bonding distance and a stronger orbital overlap and hence reduced contact resistance. For multilayer TMDC SCs, only the top layer can be hybridized by metal top contacts

while a vdW gap between the different layers of TMDC persists. Hence, the optimal performance in this case would be achieved when the metal makes edge contacts to all the layers. Furthermore, these guiding principles are based on the assumption of perfect interfaces, which in practice is rarely the case. Contact interfaces may have resist residues, may be oxidized, or even require annealing for a chemical bond to form. For example, in graphene, during annealing, the carbon atoms can dissolve into the contact metal (Ni or Co) and thus form strong covalent bonds, which contribute towards a much smaller contact resistance.[51]

Figure 16a-e illustrates the interfacial transformations of an exfoliated MoS_2 crystal with various contact metals under different vacuum conditions.[61,62] For Ti (Figure 16a)[61] deposited under a high vacuum (HV) condition, no reaction across the Ti-MoS_2 interface is observed, in contrast to DFT predictions. This is likely due to the passivation of the surface with residual oxygen or moisture in the evaporator chamber. However, when Ti is deposited with minimal oxygen content under an ultra-high vacuum (UHV) environment of an XPS, the formation of Ti-S covalent bonds can be observed. Similarly, it can be seen in Figure 16b-e that Au-MoS_2 do not react under both HV and UHV conditions while Ir, Cr and Sc react with the MoS_2 to form a combination of metal sulfides, oxysulfides and oxides under HV conditions which are usual to cleanroom metal evaporation systems.[62] The presence of UHV reduces the surface oxide for Ir, Sc, and Cr as well as the interfacial oxide for Sc which can result in crucial differences in charge injection capacities. While DFT models predict the nature of bonding between pure interfaces well, they fail to estimate the chemical composition across the interface. However, these interfaces play a role in controlling the resulting device properties; therefore, such an investigation is critical in informing the nature of the metal to be chosen and the conditions under which it should be

deposited. This thesis will further investigate the role of surface sites in altering the extent of interfacial chemical reactions with various other materials.

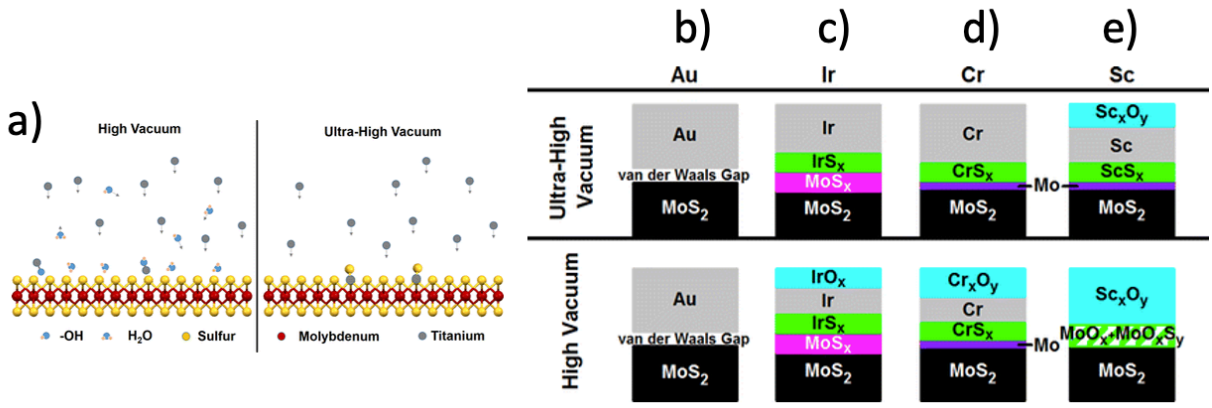

Figure 16 Phase transformations across MoS_2 surfaces on deposition of a) Ti b) Au c) Ir d) Cr e) Sc under ultra-high vacuum and high vacuum conditions. a) is Adapted with permission from reference[61]. Copyright 2016 American Chemical Society and b-e) are Adapted with permission from reference[62]. Copyright 2016 American Chemical Society.

3.2 Crystallographically Controlled MoS_2 Samples – Horizontally and Vertically Aligned

To understand the impact of crystallographic orientation on the nature of interfacial transformations, MoS_2 films with either exposed edge sites (vertically aligned) or exposed basal planes (horizontally aligned) were fabricated (see Experimental methods Section 2.2.1 for details) as shown in Figure 17. A plan-view high-resolution TEM (HRTEM) image and a selected-area electron-diffraction (SAED) pattern of a horizontally aligned sample is shown in Figure 17a. The electron beam is oriented through the basal planes, as shown in the schematic below. The SAED pattern shows that this is a single crystal with the hexagonal 2H MoS_2 crystal structure. In contrast, Figure 17b shows a plan-view HRTEM image and SAED pattern of a vertically aligned MoS_2 specimen. The image shows that the material is polycrystalline and features an abundance of widely spaced lattice fringes; these fringes correspond to the {002} planes with a spacing of 6.2 Å. The vertical alignment of the {002} lattice planes is further confirmed by the cross-sectional

scanning TEM image of a similar sulfided MoS_2 sample in Figure 17c. This image shows that the {002} planes are aligned perpendicular to the surface of the film; also, the surface of the MoS_2 film is rough (<10 nm roughness).

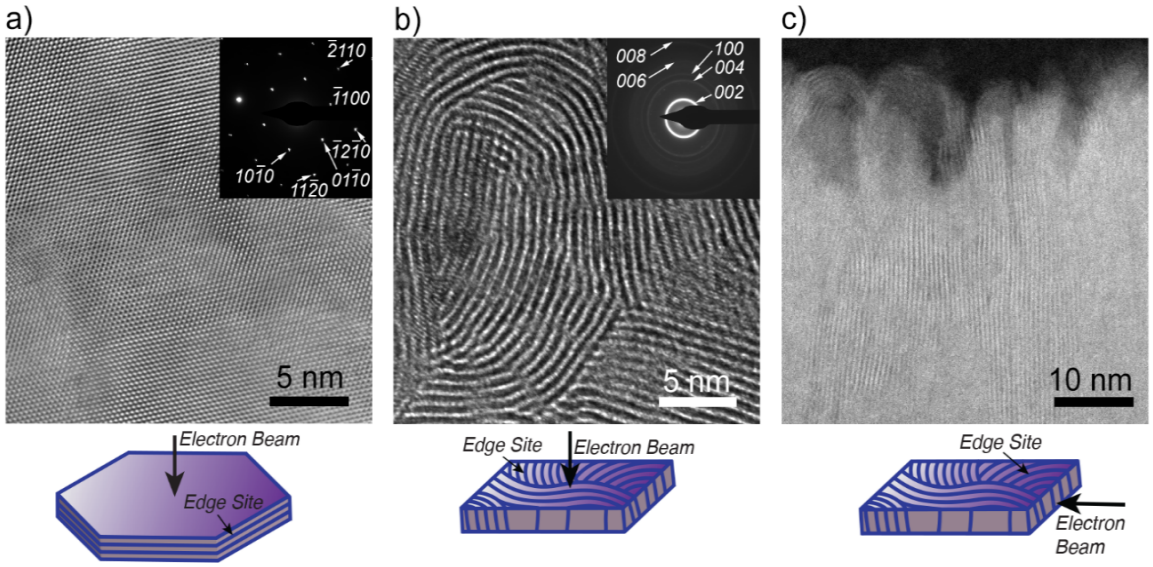

Figure 17 Crystallographically oriented MoS_2 TEM a) Plan-view (through-film) TEM image and SAED pattern of a horizontally aligned MoS_2 specimen exfoliated from a single crystal. b) Plan-view TEM image and SAED pattern of a ~15 nm thick vertically aligned MoS_2 specimen fabricated via sulfidation of a Mo film; the layers are aligned along the electron beam as shown in the schematic below the image. c) Cross-sectional STEM image of a similar sulfided ~50 nm film of MoS_2. The image clearly shows the vertically aligned layers in the MoS_2 structure.

3.3 *In situ* XPS of Phase Transformations across the Material-TMDC Interface

3.3.1. In situ XPS observation of Li – MoS_2 phase transformations

High-resolution XPS was performed to characterize the pristine MoS_2 materials. Figure 18a and c show Mo 3d and S 2p spectra obtained from a horizontally aligned MoS_2 sample before any deposition. The binding energy (BE) values for the most intense Mo 3d and S 2p doublets were found to be 229.1 ± 0.1 eV (Mo $3d_{5/2}$) and 161.9 ± 0.1 eV (S $2p_{3/2}$). These values correspond to MoS_2 (Mo^{4+} oxidation state) peaks reported in previous work (Mo $3d_{5/2}$BE = 229.3 eV, S $2p_{3/2}$ BE = 162.1 eV).[64] A small amount of nonstoichiometric Mo_xS_y with intermediate oxidation states may

also be present, as evidenced by the smaller doublets at lower BE in the Mo 3d and S 2p spectra at 228.2 ± 0.2 eV (Mo $3d_{5/2}$) and 162.1 ± 0.1 eV (S $2p_{3/2}$).[64] This could be due to the presence of surface defects introduced during mechanical exfoliation. These defect sites are a combination of S vacancies and metallic clusters of Mo;[65] since there are fewer S atoms around the Mo atoms at such sites, the electronic environment is different than stoichiometric MoS_2.[64]

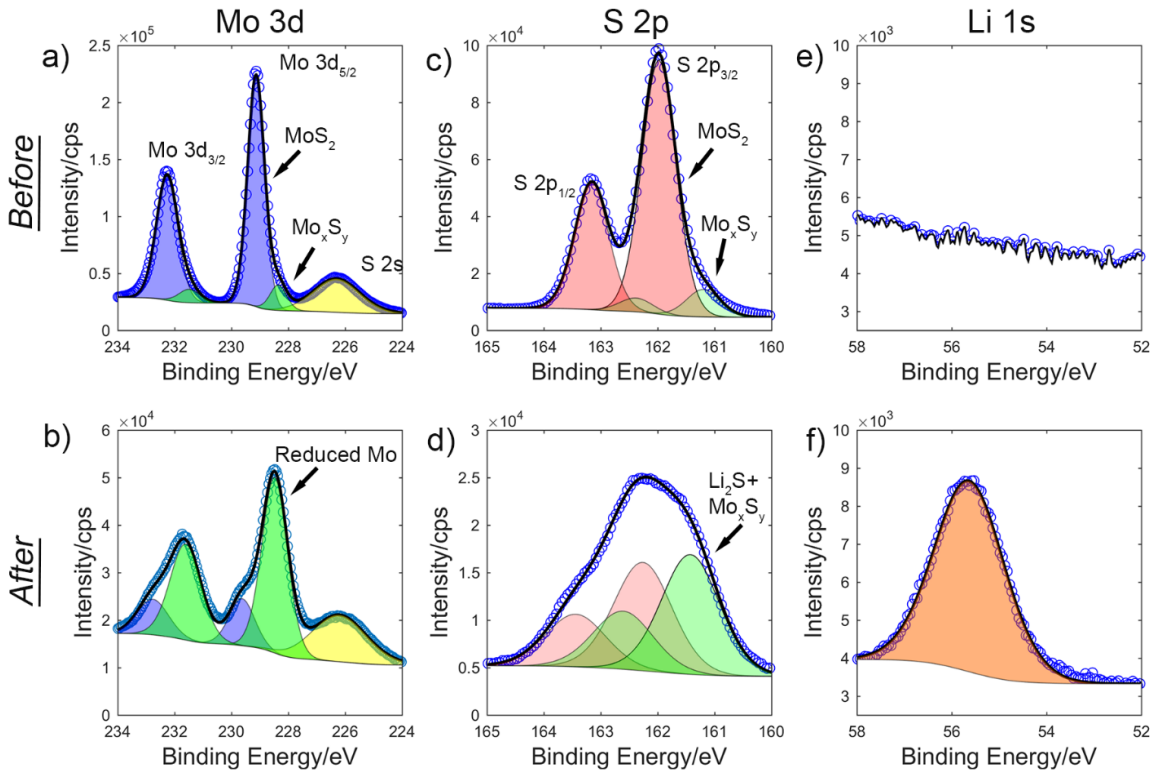

Figure 18 Interfacial phase transformations after Li deposition on horizontally aligned MoS_2. XPS spectra from a horizontally aligned MoS_2 sample before (top row) and after (bottom row) 1.3 nm of Li deposition showing different peaks: (a, b) Mo 3d, (c, d) S 2p, and (e, f) Li 1s.

Similar to the horizontally aligned sample, peaks arising from stoichiometric MoS_2 are the primary contributor to these spectra for the vertically aligned samples in Figure 18a and c, with small peaks from nonstoichiometric Mo_xS_y. A difference of ~0.1 eV in the BE of the core-level spectra is evident when comparing the two types of MoS_2; such differences were commonly observed and are attributed to sample-to-sample variation. The main difference in the

photoelectron spectra of the pristine vertically and horizontally aligned samples is the presence of a more significant O 1s peak on the vertically aligned samples, even after etching (Figure 30). This is likely due to both the unavoidable exposure of the vertically aligned thin films to the atmosphere as well as to the greater sensitivity of the exposed edge sites to oxidation than basal planes.[66] The horizontally aligned samples were exfoliated under Ar atmosphere and transferred into the XPS under vacuum. Hence, there is minimal oxidation of the horizontally aligned MoS_2 samples before material deposition. As detailed later in this section, this chemical difference could play a role in controlling reactions at interfaces formed with other materials. distinct from the original nonstoichiometric Mo_xS_y doublet in a, since S 2p peaks with lower BE also grew after Li deposition (Figure 18d). These changes in the Mo 3d and S 2p spectra are consistent with the reaction of Li with MoS_2 at the interface to form a mixture of Mo^0 and Li_2S.[67] Also, a strong Li 1s peak is detected after sputtering (Figure 18f), which verifies that Li is deposited on MoS_2. This peak likely arises from the presence of a combination of Li_2S and Li oxide/hydroxide.[68] For the vertically aligned MoS_2, similar changes of the Mo 3d, S 2p, and Li 1s spectra were observed upon depositing Li (Figure 19).

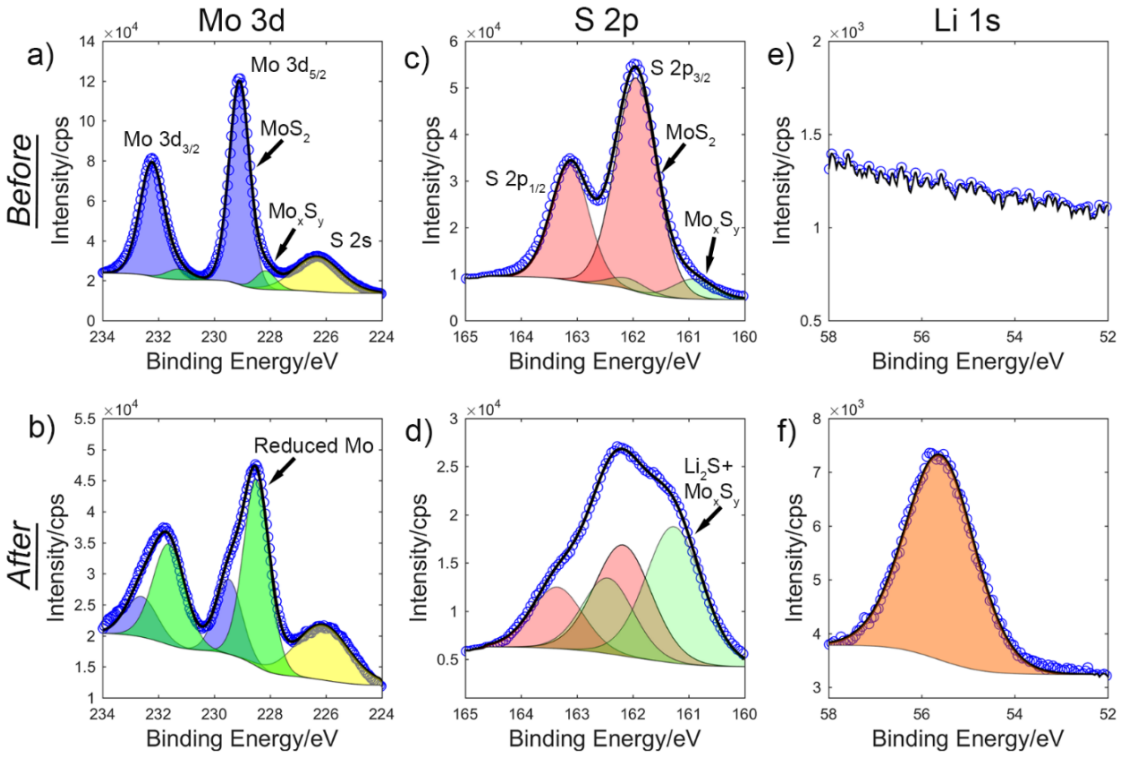

Figure 19 Interfacial phase transformations after Li deposition on vertically aligned MoS_2. XPS spectra from a vertically aligned MoS_2 sample before (top row) and after (bottom row) 1.3 nm of Li was deposited on the sample. The interfacial SiO_x was removed via HF etching before performing this XPS. (a-b) Mo 3d; (c-d) S 2p; and (e-f) Li 1s peaks.

3.3.2. In situ XPS observation of Ag – MoS_2 phase transformations

The Mo 3d, S 2p, and Ag 3d spectra for horizontally and vertically aligned MoS_2 (HF-etched) before and after 0.95 nm Ag deposition are shown in Figure 20 and Figure 21, respectively. In the pristine state, both samples again show the presence of Mo^{4+} arising from MoS_2, along with a minor amount of non-stoichiometric Mo_xS_y, as seen in the Mo 3d and S 2p peaks in Figure 20-20 a, c. Both the vertically and horizontally aligned MoS_2 samples show almost identical behavior upon Ag deposition, with insignificant changes in the relative intensity or shapes of the Mo 3d and S 2p spectra after deposition. Both samples show a systematic shift of all peaks to lower binding energies upon initial Ag deposition, which is due to electronic effects. The asymmetric Ag 3d peaks along with plasmon loss features in Figure 20-20f are representative of metallic Ag as the

predominant species on the surface after deposition. An asymmetric Doniach-Sunjic lineshape was used to fit the metallic Ag peaks. These data show that neither type of MoS_2 sample interacts with the deposited Ag to a significant degree, which is consistent with thermodynamic arguments (Section 3.5).

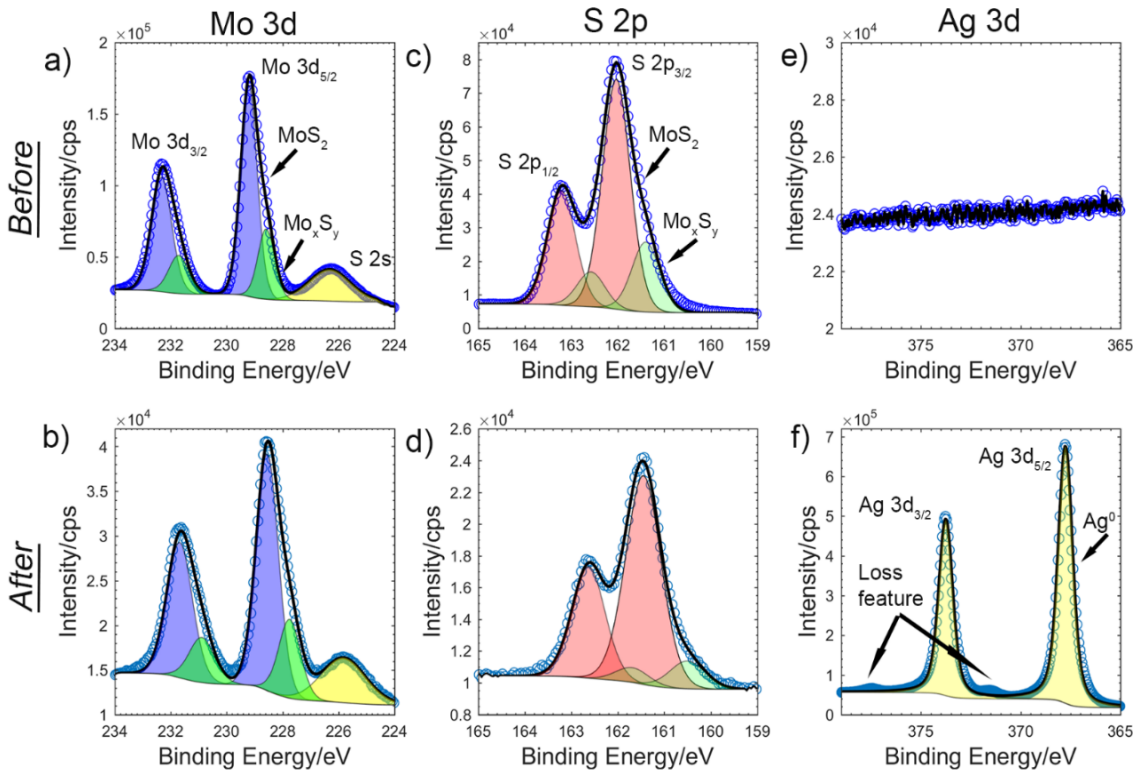

Figure 20 Interfacial phase transformations after Ag deposition on horizontally aligned MoS_2. Deconvoluted high-resolution XPS spectra before (top row) and after (bottom row) 0.95 nm of Ag was deposited on a horizontally aligned MoS_2 sample. (a-b) Mo 3d; (c-d) S 2p; (e-f) Ag 3d peaks.

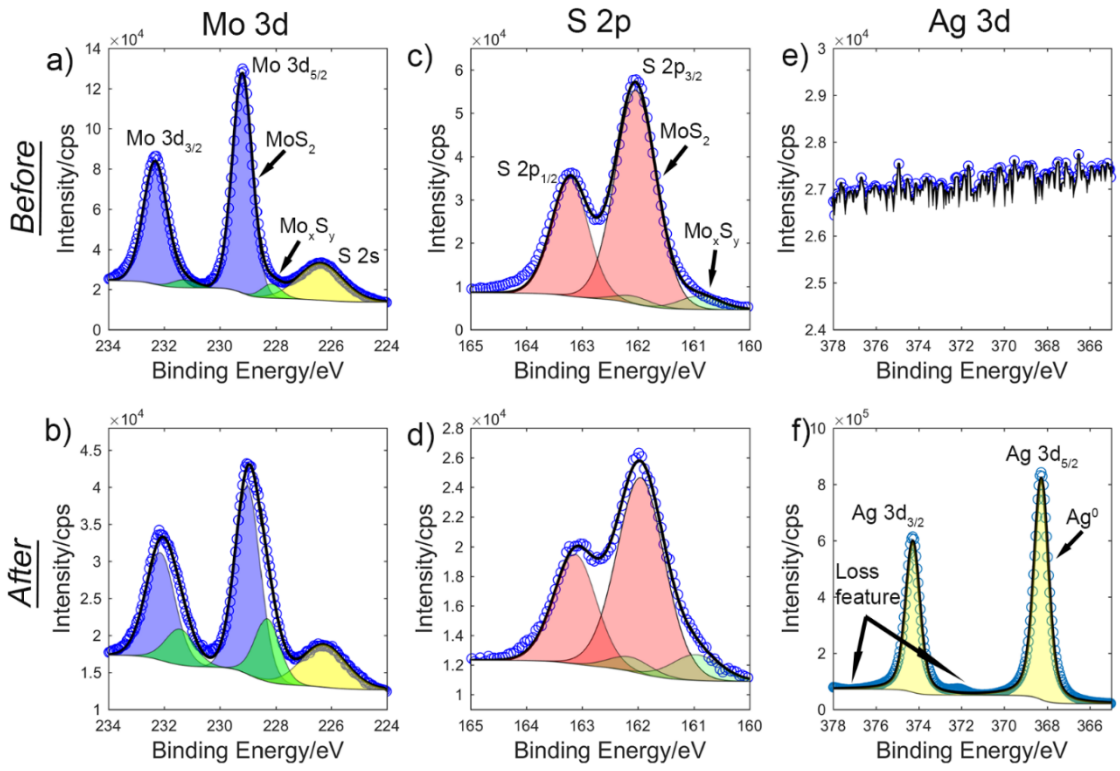

Figure 21 Interfacial phase transformations after Ag deposition on vertically aligned MoS_2. Deconvoluted high-resolution XPS spectra before (top row) and after (bottom row) 0.95 nm of Ag was deposited on a vertically aligned MoS_2 sample from which the interfacial SiO_x was removed via HF etching. (a-b) Mo 3d; (c-d) S 2p; (e-f) Ag 3d peaks.

3.3.3. In situ XPS observation of Ge – MoS_2 phase transformations

The Mo 3d, S 2p, and Ge 3d spectra for horizontally and vertically aligned (HF-etched) MoS_2 before and after 3.6 nm Ge deposition are shown in Figure 22 and Figure 23 respectively. The pristine samples again show similar features in the Mo 3d and S 2p spectra before deposition. However, upon Ge deposition, the behavior of the two types of MoS_2 samples differs. The horizontally aligned MoS_2 shows the growth of a distinctly reduced Mo doublet at lower BE after Ge deposition (Figure 22b); this doublet grows continuously with each Ge deposition step, as shown later in Figure 25. Like the Li case, this doublet corresponds to predominantly metallic Mo. The negligible change in the S 2p peak after Ge deposition (Figure 22c, d) suggests a minimal

change in the oxidation state and chemical environment of sulfur. The Ge 3d peak after deposition (Figure 22f) corresponds to elemental Ge.

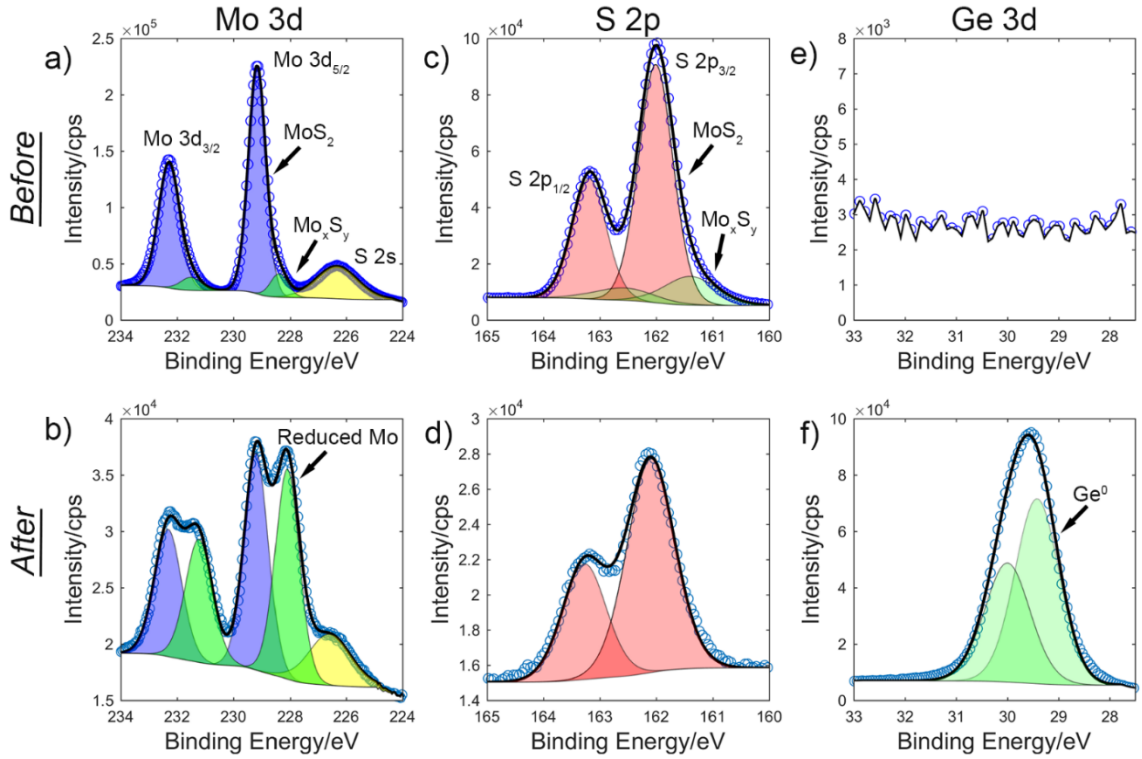

Figure 22 Interfacial phase transformations after Ge deposition on horizontally aligned MoS_2. Deconvoluted high-resolution XPS spectra before (top row) and after (bottom row) 3.6 nm Ge deposition on a horizontally aligned MoS_2 sample. (a-b) Mo 3d; (c-d) S 2p; (e-f) Ge 3d peaks.

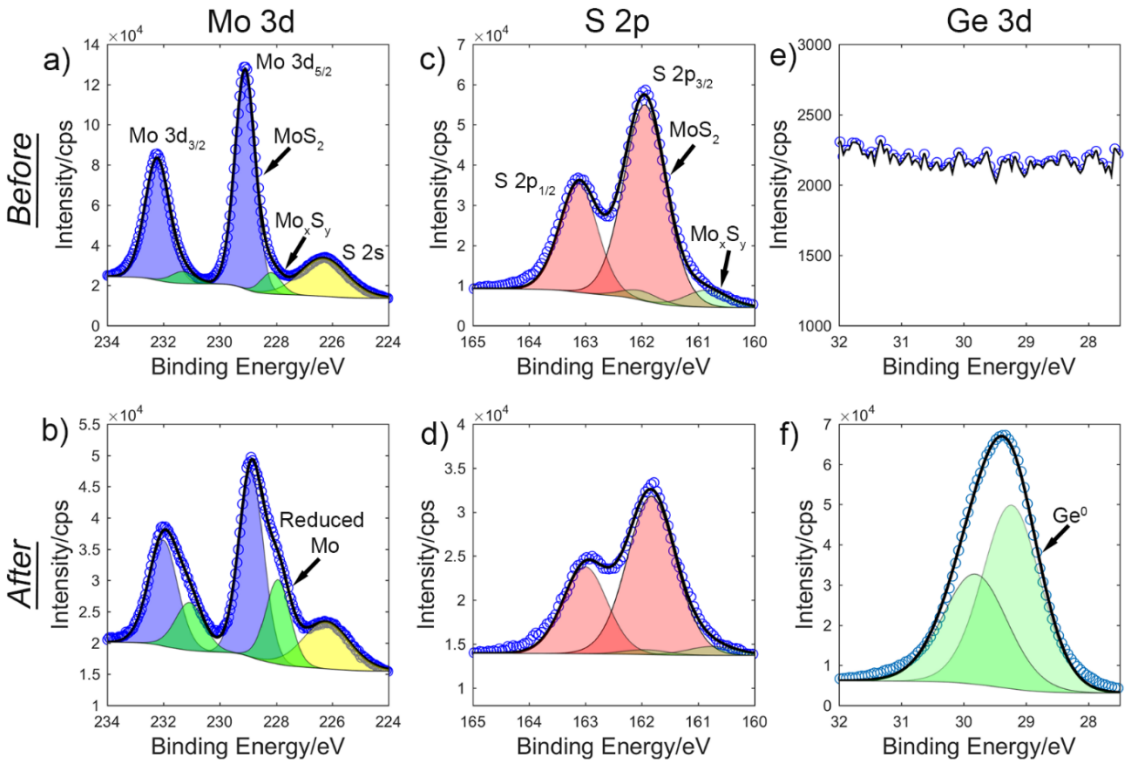

Figure 23 Interfacial phase transformations on Ge deposition on vertically aligned MoS_2. Deconvoluted high-resolution XPS spectra before (top row) and after (bottom row) 3.6 nm Ge deposition on a vertically aligned MoS_2 sample from which the interfacial SiO_x was removed via HF etching. (a-b) Mo 3d; (c-d) S 2p; (e-f) Ge 3d peaks.

3.4 Sequential Deposition of Material on the TMDC Surface

To monitor the evolution of the MoS_2/Li interface as a function of the amount of Li deposited, a series of four consecutive depositions of Li onto the horizontally and vertically aligned MoS_2 was performed. Figure 24a, b shows the evolution of Mo 3d core levels for the two types of MoS_2 samples. The entire XPS spectrum underwent a shift of ~0.3− 0.4 eV to higher BE after initial deposition. As reported previously, this shift is due to band bending in the MoS_2 due to the electronic interaction with the deposited metal,[69] and it is distinct from chemical changes (i.e., the presence of elements with different oxidation states). For both types of MoS_2 samples, a Mo 3d doublet at ~1.1 eV lower BE belonging to Mo^0 was observed to monotonically increase in relative magnitude with every deposition step, while the original Mo 3d doublet corresponding to Mo^{4+}

species decreased in relative magnitude. The full width at half-maximum (fwhm) of the reduced doublet also slightly increased with Li deposition, which could arise from the presence of convoluted peaks from multiple oxidation states. Another contributing factor is that the Mo^0 species are known to form extremely small (~1 nm) nanoparticles after reaction with Li;[22,70] the small size of these nanoparticles may also influence the peak shape.[71]

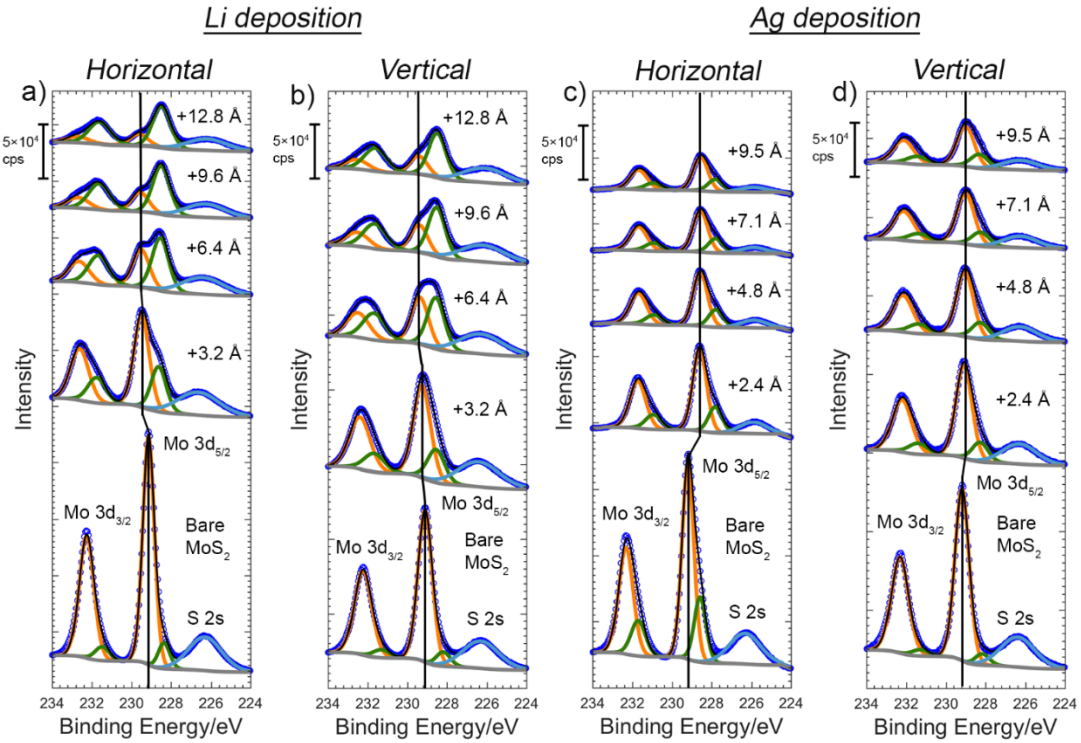

Figure 24 Evolution of Mo 3d peaks with progressive deposition of Li and Ag a) Deposition of Li onto horizontally aligned MoS_2. b) Deposition of Li onto vertically aligned MoS_2. c) Deposition of Ag onto horizontally aligned MoS_2. d) Deposition of Ag onto vertically aligned MoS_2.

Identical *in situ* depositions and XPS monitoring were carried out with Ag as the target material for comparison to Li. Figure 24c, d present the evolution of Mo 3d peaks during sequential deposition of Ag onto horizontally and vertically aligned MoS_2. Both orientations showed very little change of the Mo 3d core levels during Ag deposition. The Mo 3d spectrum was continuously attenuated due to the growth of the Ag overlayer, however. This result indicates that there are no

significant chemical interactions at the MoS_2/Ag interface for both orientations. Negligible changes were observed in the S 2p peaks before and after Ag deposition and the Ag 3d peaks showed asymmetry and plasmon losses indicating metallic Ag deposition. Finally, a shift of the entire spectrum due to band bending to a lower BE was again observed upon initial deposition of Ag onto MoS_2 and is opposite to that of Li due to expected electronegativity differences between Li and Ag (Figure 24c,d).

Finally, sequential Ge deposition was also carried out on horizontally and vertically aligned MoS_2. Figure 25a, b presents the evolution of Mo 3d peaks before and after sequential Ge deposition steps. In contrast to the cases of Li and Ag, the samples with different orientations of MoS_2 showed different behavior upon Ge deposition. For horizontally aligned MoS_2, a monotonic growth of a Mo 3d doublet corresponding to Mo^0 was observed after Ge deposition (Figure 25a). For the vertically aligned sample (Figure 25b), however, this Mo 3d doublet at lower BE grew to a lesser degree in relative area compared to the horizontally aligned MoS_2. The S 2p spectra do not show significant changes after Ge deposition, and the detection of Ge 3d peaks in both cases show that elemental Ge was deposited (Ge $3d_{5/2}$ BE = ~ 29.2 eV).[72] These results indicate that there is a more substantial chemical interaction at the MoS_2/Ge interface for horizontally aligned MoS_2 than for vertically aligned MoS_2.

Figure 25c summarizes the results for the deposition of Li, Ag, and Ge onto both types of MoS_2 samples. This plot shows the ratio of the area of the Mo $3d_{5/2}$ peak at lower BE (Mo^0) to that of the original peak (Mo^{4+}) with higher BE as a function of deposited thickness. The data show that MoS_2 samples with both orientations underwent a similar extent of reaction when in contact with Li, while the MoS_2/Ag interface did not show significant chemical interactions. The chemical interactions at the MoS_2/Ge interface were dependent on the type of MoS_2 sample, with the reduced

Mo $3d_{5/2}$ peak growing in relative area for horizontally aligned samples but showing less-substantial changes for the vertically aligned samples.

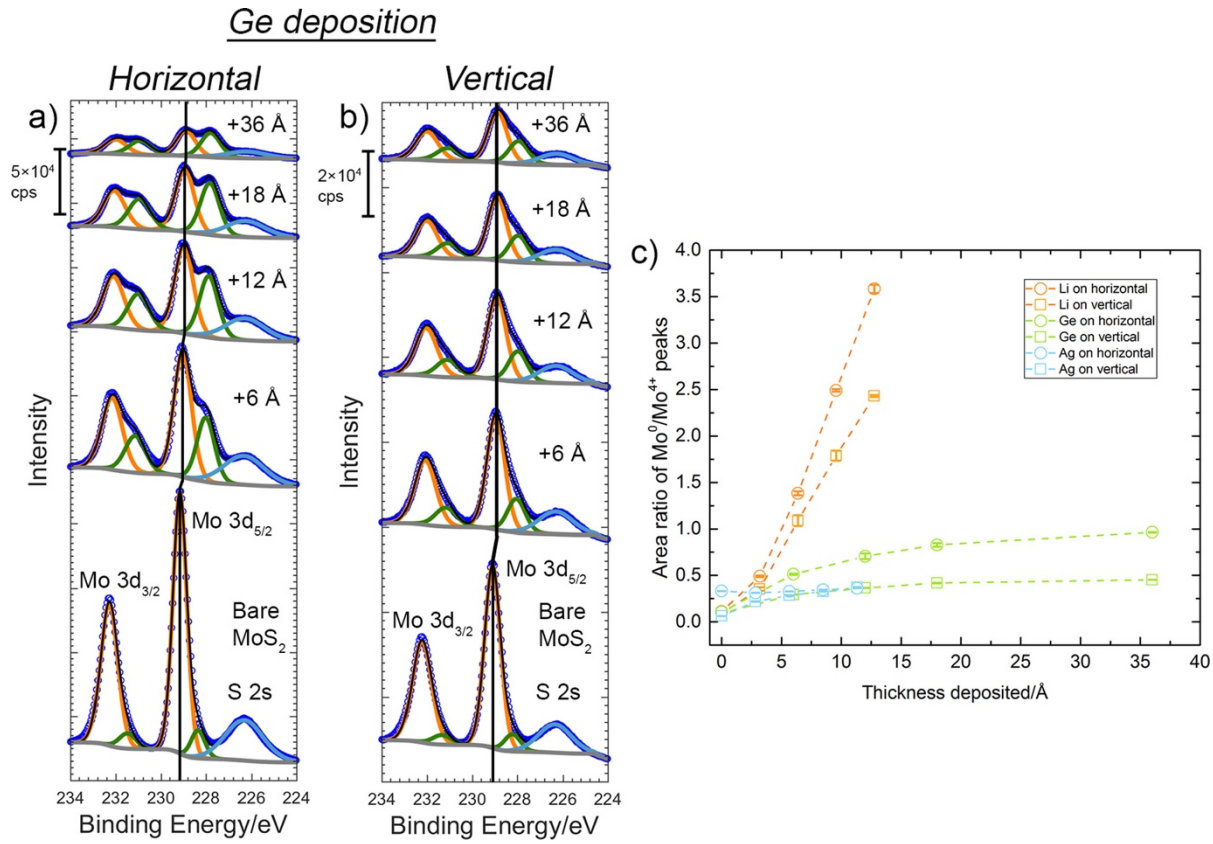

Figure 25 Evolution of Mo 3d peaks during the sequential deposition of Ge onto a) horizontally aligned MoS_2 and b) vertically aligned MoS_2. c) The ratio of the area of the Mo 3d5/2 peak with lower binding energy (Mo0 peak) to the Mo 3d5/2 peak with higher binding energy (Mo4+ peak) for each of the three deposited materials. This area ratio is presented as a function of deposited thickness. Error bars represent the possible deviation in the fitted areas for the deconvolution of the Mo 3d5/2 peaks.

The Mo 3d and S 2p core level binding energy values were observed to differ slightly from sample to sample, as seen in Table 1. The minor variations in binding energy across samples have been reported to be due to inherent surface defects introduced during mechanical exfoliation for horizontally aligned MoS_2.[37] Further variations could arise from differing amounts of surface oxide on the vertically aligned material, which could influence the chemical/electronic nature of the sample.[37]

Table 1 Binding energy values of the Mo $3d_{5/2}$ (listed first) and S $2p_{3/2}$ (listed second) core levels before material deposition for the different samples used in this study.

	Horizontally aligned MoS_2	Vertically aligned MoS_2, HF etch	Vertically aligned MoS_2, as-synthesized
Pre-Li	**229.13 eV, 161.98 eV**	**229.10 eV, 161.94 eV**	**228.97 eV, 161.81 eV**
Pre-Ge	**229.16 eV, 162.00 eV**	**229.12 eV, 161.95 eV**	**228.90 eV, 161.74 eV**
Pre-Ag	**229.20 eV, 162.03 eV**	**229.06 eV, 161.90 eV**	**229.10 eV, 161.95 eV**

Additionally, multiple experiments were performed for each combination of MoS_2 samples (vertically or horizontally aligned) and deposition material (Li, Ge, or Ag). In general, the experiments for each combination of MoS_2 type and deposited material showed consistent results. Figure 26 shows the ratio of the area of the Mo^0 $3d_{5/2}$ peak to that of the Mo^{4+} $3d_{5/2}$ peak for different experiments using horizontally and vertically aligned MoS_2. Li deposition (Figure 26a) caused a significant growth of the reduced (Mo^0) Mo $3d_{5/2}$ peak for both types of MoS_2 samples in all cases, although the extent of growth varied slightly among the different experiments. For Ag deposition (Figure 26b), the ratio of the Mo $3d_{5/2}$ peak area arising from Mo^0 to that of Mo^{4+} stayed below ~0.45 for all cases. For Ge deposition (Figure 26c), all three horizontally aligned samples showed substantial growth of the Mo^0 (Mo $3d_{5/2}$) peak after deposition, while the vertically aligned samples showed fewer substantial changes. For Ag and Ge deposition onto the vertically aligned samples with the SiO_x interfacial layer, the extent of interaction was always lower than SiO_x-free samples. This indicates a passivating effect of the SiO_x interlayer for these two deposited materials. These data show that these results are repeatable and consistent, which indicates that our experimental methods are sufficient for monitoring interfacial changes.

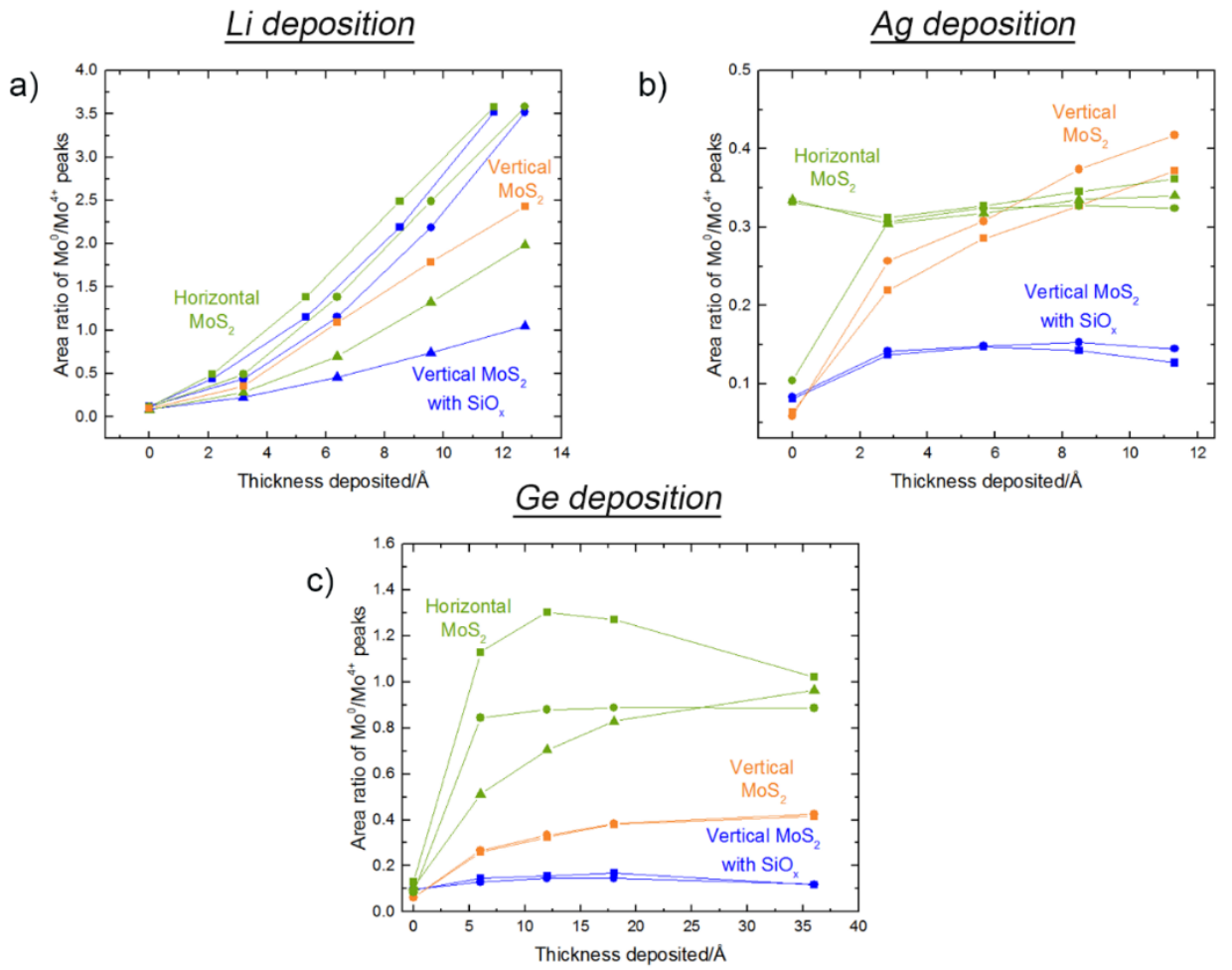

Figure 26 The ratio of the area of the Mo $3d_{5/2}$ peak for the Mo^0 state to that of the Mo^{4+} state for two sample sets. a) Li deposition, b) Ag deposition, and c) Ge deposition. Green data are from horizontally aligned MoS_2, orange data are from vertically aligned MoS_2, and blue data are from vertically aligned MoS_2 with an interfacial SiO_x layer. Different symbols represent different experimental runs.

3.5 Possible Reaction Mechanisms Driving the Phase Transformations

To rationalize the observations presented herein, it is helpful to examine the thermodynamics of possible interfacial reactions. The reaction of MoS_2 with a deposited material *M* can proceed according to the following equation ***(1)***:

$$\boldsymbol{MoS_2 + 2xM \rightarrow 2M_xS + Mo} \qquad \textbf{(1)}$$

When the material *M* is Li, this reaction is thermodynamically favorable since the Gibbs free energy of formation (ΔG_f°) of Li_2S is significantly more negative than that of MoS_2, yielding

a large driving force of ΔG^{o}_{rxn} = -323 kJ/mol of S for the reaction.[73] The formation of Mo and Li_2S upon deposition of Li is supported by our results for both horizontally and vertically aligned MoS_2 samples. This involves the growth of the Mo 3d and S 2p doublets at lower binding energies after Li deposition. Even though the S^{2-} species do not change the formal oxidation state during this reaction, the S 2p spectrum is expected to be different for Li_2S compared to MoS_2 because of the significantly different electronegativity of Li and Mo (χ_{Mo} = 2.16, χ_{Li} = 0.98, χ_S = 2.58).[74] Due to a total deposition of only ~1.2 nm of Li on much thicker MoS_2 films (~50 nm), the interfacial reaction is limited by the amount of Li available and only progresses with more Li deposition. This conclusion was supported by additional experiments in which the MoS_2 surface was monitored with XPS for 60 min beyond the time required for the deposition of Li (see Figure 27). The data showed that the shape and area of the Mo 3d peaks remained the same over this 60-minute period, which indicates that the interfacial reaction proceeded faster than the temporal resolution of these experiments (~35 sec).

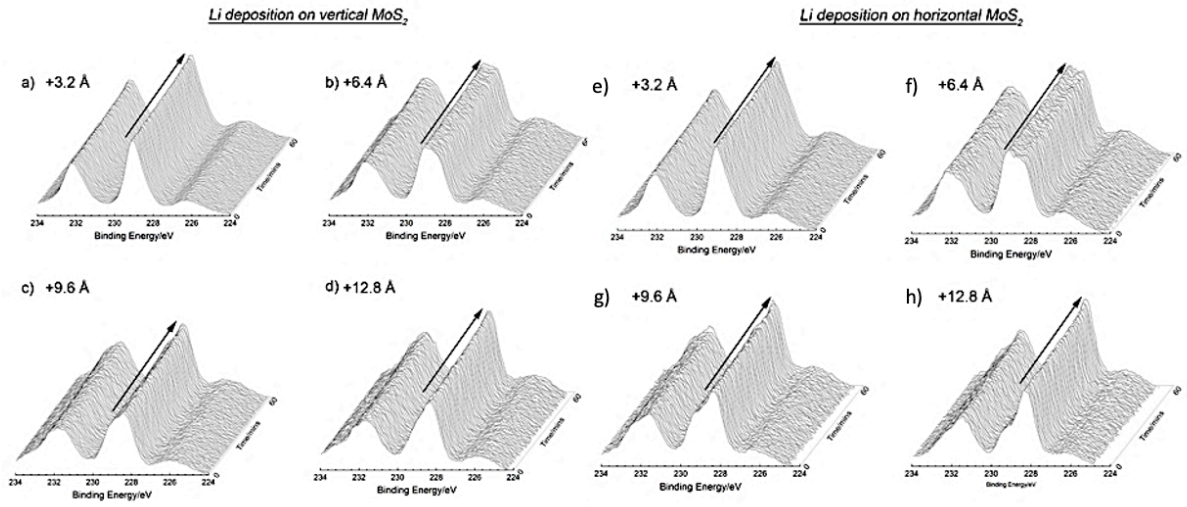

Figure 27 Evolution of Mo 3d peaks over 60 minutes after initial Li deposition on vertically aligned (left) and horizontally aligned MoS_2 (right). Scans of the Mo 3d spectrum were collected over 1 hour after a,e) 3.2 Å b,f) 6.4 Å c,g) 9.6 Å and d,h) 12.8 Å of Li deposition.

An important finding herein is that Li reacts with MoS_2 to a similar extent for both crystallographic orientations. This finding is in contrast to previous work that has found that Li does not exhibit an appreciable interfacial reaction at the edge sites of large single crystals of MoS_2, as Li intercalation within the crystals was presumed to occur faster than the interfacial reaction process.[69] However, there was a key difference in methodologies between this previous work and our study, as they obtained stepped edge sites by cleaving large single crystals under vacuum, implying high crystal quality and a lack of surface oxidation. In our case, surface oxide or oxysulfide is present on the vertically aligned samples, and the samples are also polycrystalline and rather disordered. While the presence of surface oxide does not prevent the reaction of the underlying MoS_2 (as proven by the changes in the S 2p spectrum of the vertically aligned samples), it may change the kinetics of Li transport as well as cause an interfacial reaction with both the oxygen and sulfur species. Furthermore, the disordered nature of the vertically aligned sample may also induce interfacial reactions due to the presence of defective sites that cause different reaction kinetics than conventional surfaces.

In contrast to Li, the reduction of MoS_2 by Ag is not thermodynamically favorable (ΔG^{o}_{rxn} = +95 kJ/mol of S).[75] The observation of a lack of significant changes of the Mo 3d and S 2p spectra for both MoS_2 orientations upon Ag deposition is in line with this thermodynamic prediction. Minor variations in the extent of interaction with the MoS_2 samples were observed across multiple Ag depositions. These slight variations could be due to the presence of a variety of intrinsic surface defects on the MoS_2, which enhances the charge transfer between Ag and MoS_2, as reported by Addou *et al.*[76]

Unlike the Li and Ag cases, the MoS_2/Ge interfacial interaction showed a strong dependence on the type of MoS_2 sample investigated, with the horizontally aligned MoS_2 showing an apparent reaction with Ge while the vertically aligned MoS_2 showed a less substantial interaction. Interestingly, the reaction of Ge with MoS_2 to form GeS based on equation ***(1)*** is not thermodynamically favorable, since ΔG°_{rxn} = +57 kJ/mol of S.[75] Thus, this thermodynamic calculation fails to predict a spontaneous reaction between Ge and MoS_2. However, the changes in the Mo 3d peaks upon Ge deposition onto horizontally aligned MoS_2 strongly suggest that the Ge reacts with near-surface sulfur to form reduced Mo. Alternative explanations for this observed behavior include the possibility that a reaction other than that shown in equation ***(1)*** occurs at the interface, and/or that the interface does not behave according to bulk thermodynamics because of surface dangling bonds or other defects that are not present in the bulk phases. Regarding the first option, the thermodynamics of the reaction would be modified if the deposited Ge formed an alloy with the newly produced Mo in addition to reacting with the S species, as shown in equation ***(2)***:

$$\boldsymbol{xMoS_2 + (2x + y)Ge \rightarrow (2x)GeS + Mo_xGe_y} \qquad \textbf{(2)}$$

Several Mo-Ge alloy phases are known to form at high temperature,[77], and assuming a sufficiently negative ΔG_f° for such alloys, alloy formation could serve to negate the positive ΔG°_{rxn} previously calculated for the overall reaction. Such a mechanism has previously been postulated for TMDC interfacial reactions.[78] This Ge-Mo alloying mechanism could further be promoted by the fact that other studies have also found that TMDC/metal interfaces that show positive bulk enthalpies of reaction (up to ~50 kJ/mol) can still show interfacial reactivity.[78] Such a phenomenon likely occurs because the interface is not a bulk phase and has additional energetic features (*e.g.*, dangling bonds, strain energy) that must be taken into account besides bulk free energies of formation. Finally, we note that in contrast to Ge/Mo, Ag and Mo do not form any intermediate

phases or solid solutions,[79] which supports this alloying theory since Ag did not chemically interact at the interface of MoS_2.

In contrast to the behavior of Ge on horizontally aligned MoS_2, Ge deposited on vertically aligned MoS_2 showed less substantial chemical interactions (the reduced Mo 3d doublet at lower BE increased less substantially). We postulate that this less significant interfacial interaction is due to the differing chemistry and structure of the vertically aligned MoS_2 compared to horizontally aligned material; in particular, the presence of a thicker oxide (MoO_x) or oxysulfide layer may play a role. Oxides or oxysulfides that are substoichiometric (*i.e.*, MoO_x, where $x \leq 2$) could be present due to the disordered and non-uniform nature of the surface of the vertically aligned MoS_2. These materials are likely to exhibit small or positive reaction free energies (for instance, ΔG^{o}_{rxn} = +6 kJ/mol of O for the reaction of MoO_2 with Ge to form GeO_2 and Mo[73]). Furthermore, such interfacial films likely increase the kinetic barrier for the transport of Ge through the interfacial layer to interact with the underlying MoS_2, which also would decrease the chemical interactions at the interface. Beyond surface oxide effects, it is also possible that the disordered and non-uniform surface of the vertically aligned samples plays a role. These findings have important ramifications for interfacial engineering in TMDC-based electronic devices, since the formation of a reacted interphase vs. hindered reaction due to the presence of interfacial layers will likely impact important electronic properties, including contact resistance, band structure and electron transport.

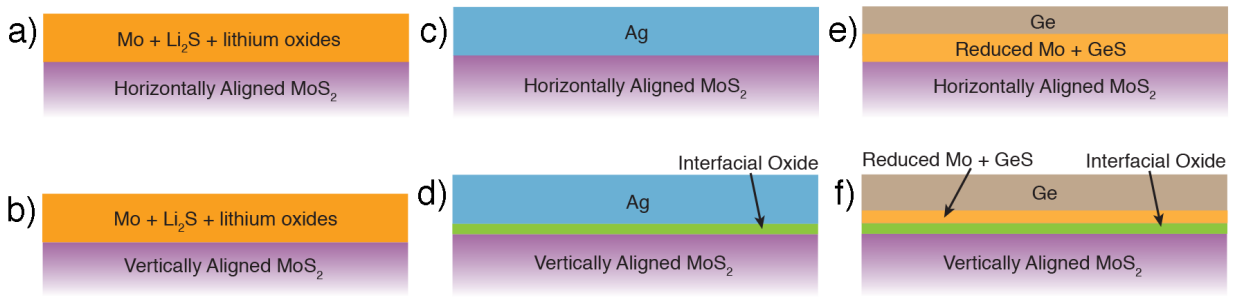

Figure 28 Schematic illustrating the chemical nature of interfaces formed upon a, b) Li, c, d) Ag, and e, f) Ge deposition onto horizontally and vertically aligned MoS_2 samples.

Figure 28 summarizes the findings on interfacial transformations in MoS_2 studied in this section. These results have important ramifications for interfacial engineering in TMDC-based electronic devices and other applications, since the formation of a reacted interphase vs. hindered reaction due to the presence of interfacial oxide layers will likely impact important electronic properties in different ways, including by altering contact resistance, band structure and electron transport.

3.6 Role of Surface Oxide in Altering the Phase Transformations across the Material-TMDC Interface

The as-synthesized, vertically aligned MoS_2 samples feature a layer of SiO_x on the surface. HF etching was performed to remove this layer; Figure 29 shows the influence of this HF etching step on the Si 2p and O 1s peaks on a typical vertically aligned MoS_2 sample. The Si 2p signal was significantly reduced after the HF etch, confirming the removal of the SiO_x layer. The O 1s signal was also reduced after etching, although some oxygen signal remains.

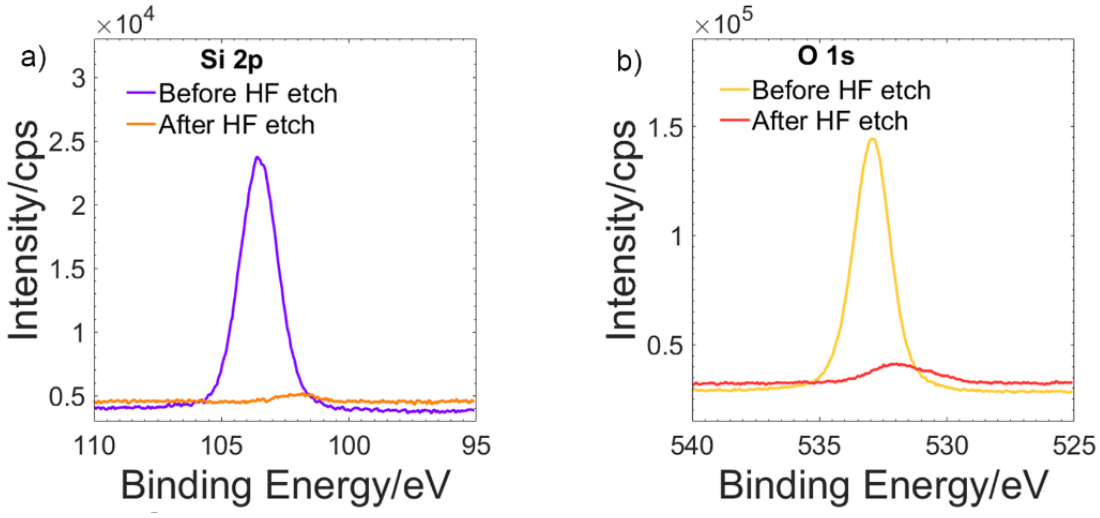

Figure 29 Influence of HF etching on surface oxide (a) Si 2p and (b) O 1s peaks on the surface of vertically aligned MoS_2 samples before and after HF etching to remove the interfacial SiO_x layer.

The effects of oxygen species and surface oxides were also investigated, since oxygen species have been shown to alter the chemical nature of the interface formed between TMDCs and other metals.[61] As seen in Figure 30, the exfoliated horizontally aligned samples have only minimal surface oxide because of the relatively inert nature of the basal planes. An adsorbed layer of oxygen and adventitious carbon (giving rise to C-O bonds) was observed for horizontally aligned samples. The vertically aligned samples feature more substantial O 1s peaks. This likely corresponds to a mixture of Mo oxides and/or oxysulfides. The presence of a mixture of MoO_2 and MoS_2 has been reported previously on the surface of sulfided samples by Spevack *et al.*[80]

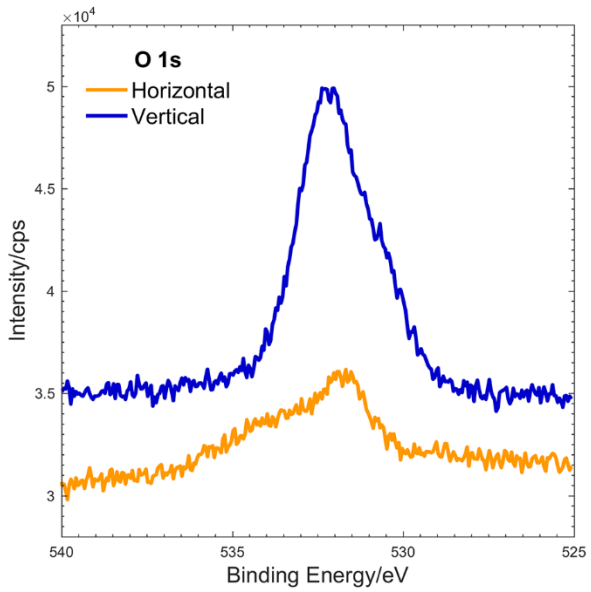

Figure 30 High-resolution O 1s XPS spectra on pristine horizontally aligned MoS_2 and vertically aligned MoS_2 that was HF-etched to remove the SiO_x interfacial layer.

Figure 31 shows the evolution of O 1s XPS core levels during the deposition of the various materials on both types of MoS_2 samples. Negligible or small amounts of surface oxide are detected before any material deposition for the horizontally aligned MoS_2 samples, as displayed in Figure 31a, c, and e (bottom traces). Trace amounts of impurities present in the natural crystal can be responsible for the relative differences. As discussed previously, the vertically aligned MoS_2 samples exhibit more substantial oxygen signals (Figure 31b, d, f).

Upon Li deposition (Figure 31a and b), the integrated area of the O 1s peak is observed to increase for both horizontally and vertically aligned MoS_2 samples. As discussed previously, this is due to the partial oxidation of the lithium during the deposition process. The O 1s spectrum also changes shape in both cases, with additional signal intensity at lower binding energies. This is likely due to the formation of different lithium-oxygen compounds. Upon Ge deposition, the horizontally aligned MoS_2 (Figure 31c) shows only minor O 1s peaks that remain approximately constant in magnitude. This is similar to the behavior of the horizontally aligned MoS_2 during Ag

deposition (Figure 31e). In both cases, this behavior arises due to the burying of the initial adsorbed oxygen species by the deposited material; the XPS signal during deposition then arises due to small amounts of surface oxide on the Ge or Ag film. For the deposition of both Ge and Ag on vertically aligned MoS_2 (Figure 31d-f, respectively), the O 1s peak intensity decreases upon initial deposition due to the deposited material covering the Mo-oxide layer.

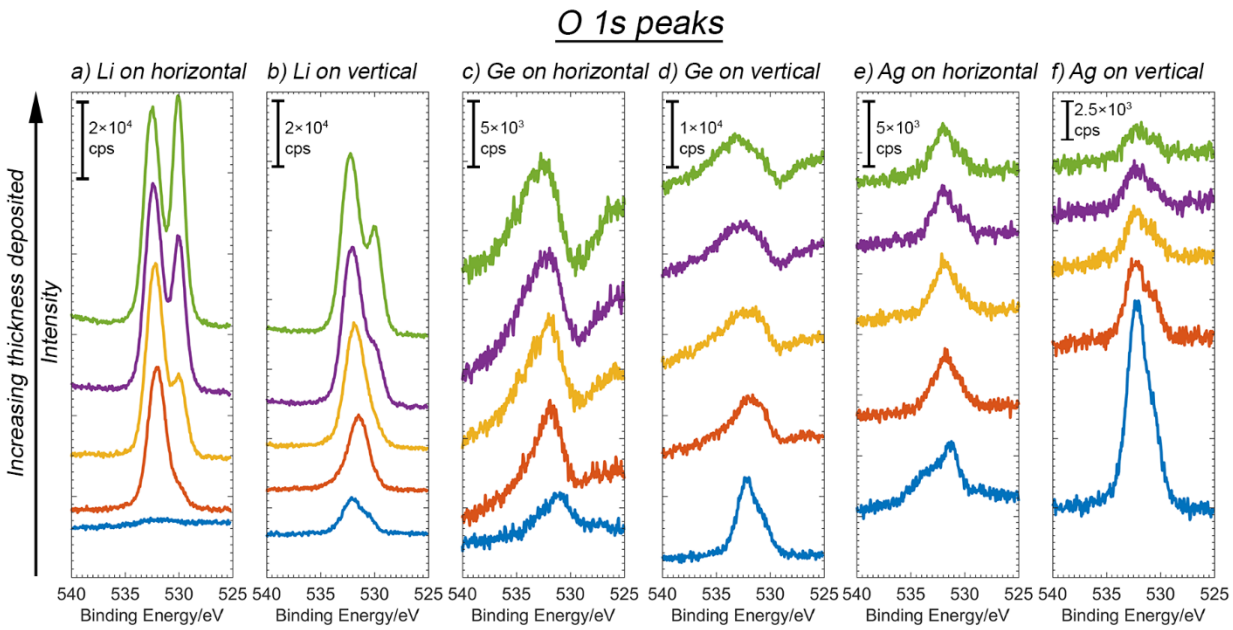

Figure 31 Evolution of O 1s spectra with depositiona) Li on horizontally aligned MoS_2, b) Li on vertically aligned MoS_2, c) Ge on horizontally aligned MoS_2, d) Ge on vertically aligned MoS_2, e) Ag on horizontally aligned MoS_2, and f) Ag on vertically aligned MoS_2. All vertically aligned samples were etched with HF to remove the interfacial SiO_x layer. The pristine sample is the bottom trace for each plot. Each Li deposition step deposits 3.2 Å, each Ge deposition step deposits 6.0 Å (except the last one being 18.0 Å), and each Ag deposition step deposits 2.8 Å.

To further investigate the behavior of surface oxide, the peak areas (integrated intensity under the respective peaks) of Li 1s, Ge 3d, and Ag 3d were compared for the two orientations of MoS_2 as a function of deposition of the respective materials (Figure 32). The area values were normalized using their pre-deposition values and hence all curves start at 1.0 but have not been scaled using their relative sensitivity factors, hence the widely different values of area growth. As seen in Figure 32, this area consistently increased at a greater rate for the vertically aligned MoS_2

samples, across all depositions. This trend suggests that despite sputtering Li, Ge and Ag under identical conditions, more of these elements are detected on the surface of the vertically aligned MoS_2. This is possibly due to the hindrance to diffusion of these elements into the MoS_2 lattice introduced by the presence of surface oxide on the vertically aligned MoS_2. The diffusion barrier for the horizontally aligned MoS_2 is much lower due to negligible surface oxidation.

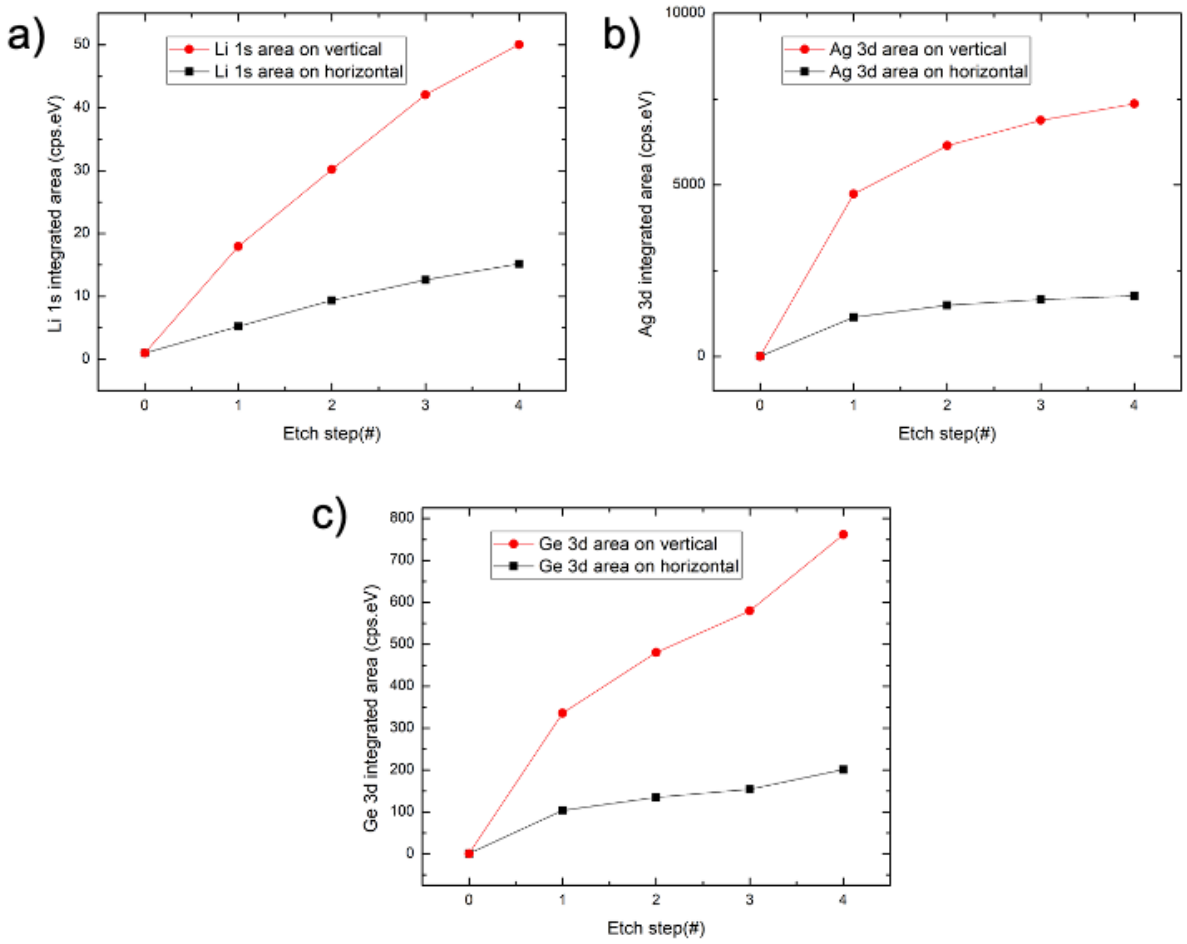

Figure 32 Evolution of area (integrated intensity) values for a) Li 1s, (b) Ge 3d, and (c) Ag 3d with each deposition step. The area values have all been normalized to their respective pre-deposition area value and hence they all start at 1.0. No relative sensitivity factor has been accounted for to calculate these areas of high-resolution XPS scans.

The following conclusions can be drawn from these results:

- The vertically aligned MoS_2 is more susceptible to surface oxidation possibly due to the presence of a large number of edge sites.

- Sample-to-sample variation of this surface oxide exist, as seen in Figure 31b, d, and f, despite using identical fabrication conditions.
- The surface oxide on the vertically aligned MoS_2 may pose a kinetic barrier to diffusion of material across the MoS_2-material interface.

Thus, contrary to the common understanding of vertically aligned MoS_2 being more chemically active, the passivation of its surface due to oxidation can not only affect its chemical reactivity to a large extent but also hinder the diffusion of interfaced materials through it. This alters the kinetics of the reaction across the material-MoS_2 interface, in turn altering the composition and possibly its properties.

3.7 Role of Annealing in Assisting Phase Transformations across the Metal-MoS_2 Interface

Annealing of metal-TMDC interfaces is routinely performed to remove photoresist residues and improve the bonding across the interface. Several studies have shown that annealing lowered contact resistance and improved the electronic switching properties of such devices.[81–86] Leong et al. showed that annealing Ni-graphene interfaces resulted in the dissolution of carbon atoms into the Ni contacts which was the cause of the lower contact resistance.[51] Furthermore, annealing can also alter the physical structure across the interface even when no chemical reactions occur. Chen *et al.* demonstrated the formation of a single-crystalline Au film on deposition followed by annealing on a bilayer MoS_2 grown on sapphire substrates.[87] While depositing and annealing Au only on sapphire or mica substrates resulted in the formation of discontinuous islands of Au, the Au/MoS_2/sapphire stack resulted in the formation of single-crystalline Au contacts with ~10 times lower contact resistance values.

With this in mind, it was important to investigate the role of annealing on the interface character of our horizontally and vertically aligned MoS_2 samples. It also enabled the investigation of elevated temperatures on the diffusion kinetics of metal atoms through the surface oxide layer discussed in Section 3.6. Ni was the metal of choice because it is thermodynamically favorable for it to react with MoS_2 both during its synthesis and with grown MoS_2 crystals.[88–94] The reaction mechanisms are discussed in greater detail in the upcoming sections. *Ex-situ* grazing incidence X-ray diffraction (GIXRD) was utilized to understand the change in crystallite size and structure on annealing Ni-MoS_2 samples. First, several pristine MoS_2 samples were fabricated starting with sulfidation of 2 nm Mo (horizontally aligned) and 10 nm Mo (vertically aligned) films via the methods discussed in Section 2.2.1. Then, 2 nm of Ni was deposited on both types of MoS_2 samples. These Ni-MoS_2 samples were then annealed under Ar/S atmosphere in a procedure identical to the sulfidation of pure MoS_2 samples. Finally, 2 nm Ni was deposited onto 2 nm Mo and 10 nm Mo samples before sulfidation, and then they were sulfided together under the Ar/S atmosphere. These resulted in the Ni-Mo sulfided samples.

Figure 33 shows the GIXRD curves for all of these samples. It is important to note that the intensity of these peaks depends on both the material thickness as well as the physical size of the samples. The intensity is not normalized by the sample size even though the size of the samples was very similar (~ 1 cm^2). Hence, the FWHM of these peaks rather than intensity is used for comparison and understanding of the physicochemical changes post-annealing. The horizontally aligned pristine MoS_2 sample shows a very weak and broad peak at ~14˚ (0002) due to its ultra-thin nature with only 2 nm Mo being sulfided. The broad peak suggests that the film is highly polycrystalline and disordered even after sulfidation at 700 ˚C. It is interesting to note, however, that on the deposition of just 2 nm Ni on this pre-sulfided MoS_2, the sharpness of (0002) MoS_2

peak increases substantially. When 2 nm Ni is deposited on 2 nm Mo and then sulfided, this peak is even sharper. The (0002) peak corresponds to horizontally aligned (*i.e.,* basal-plane exposed) MoS_2 since the plane normal is along the c-axis. This implies that Ni undergoes a reaction with these horizontally aligned MoS_2 layers to result in increased crystallite size. Note that basal planes in a single crystal of MoS_2 are thought to be relatively inert due to weak bonding via van der Waals forces. However, in the case of polycrystalline MoS_2, grain boundaries, steps and terraces could be among the surface defects contributing to the presence of active edge sites. Previous studies have suggested a likely reaction between Ni atoms and edge sites of MoS_2 crystals which in turn allow for faster lateral growth of these crystals. The mechanism of this process is investigated with *in situ* TEM in Section 4.

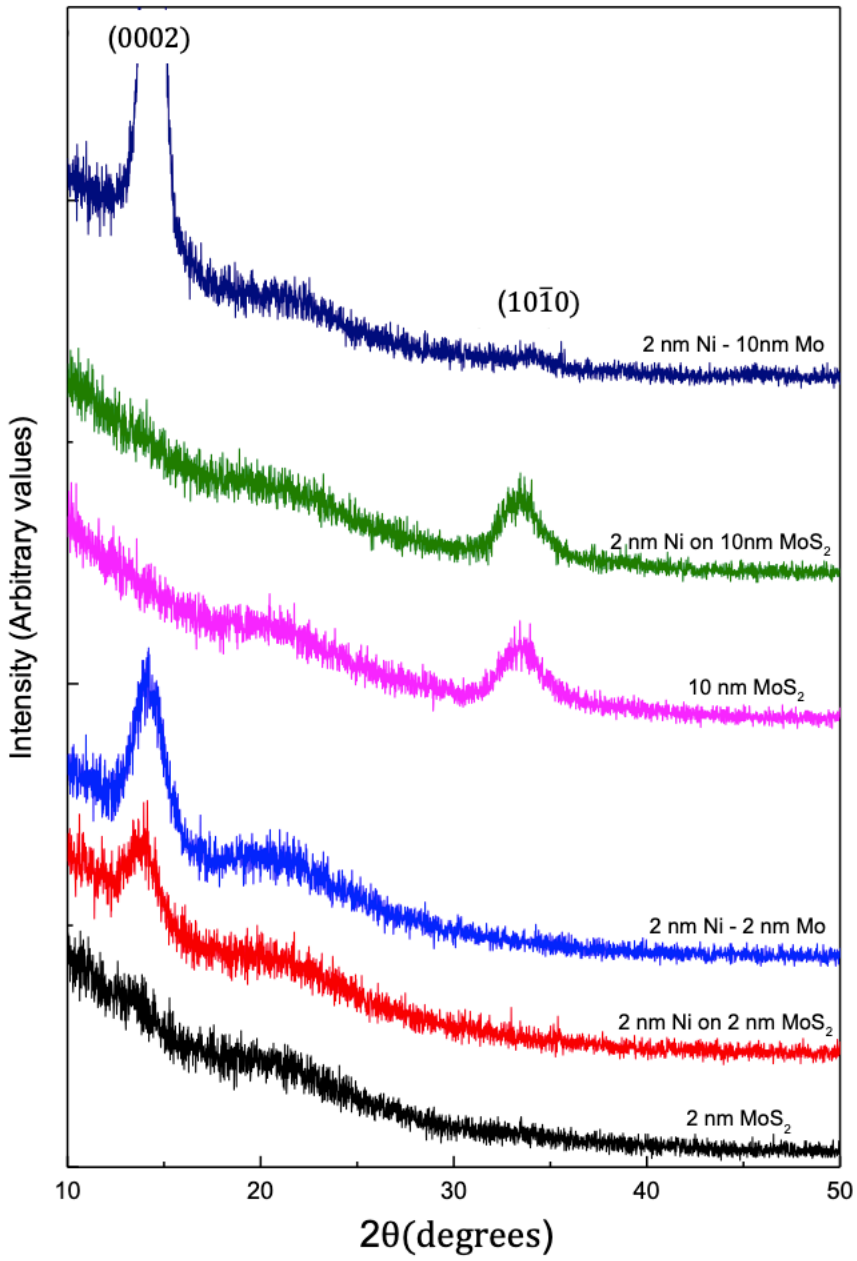

Figure 33 GIXRD curves for horizontally and vertically aligned MoS_2 sulfided under different conditions. For the Ni on MoS_2 samples, Ni was deposited on pre-sulfided MoS_2 and annealed under Ar/S conditions again. For the Ni-Mo samples, the samples were exposed to sulfur only once and together. The peak marked (0002) corresponds to horizontally aligned MoS_2 while (10$\bar{1}$0) corresponds to vertically aligned MoS_2.

However, the case with vertically aligned MoS_2 is significantly different. The pure 10 nm MoS_2 features only one peak at ~32˚ (10$\bar{1}$0), corresponding to vertically oriented crystals (*i.e.,* the plane normal is along the $\vec{x}$ axis). On annealing Ni deposited onto pre-sulfided MoS_2, no significant

difference in the FWHM of this peak is seen. However, when the Ni-Mo sample is sulfided together, a very intense (0002) peak (also due to the presence of more material) is observed. It is sharper than the peak observed for the 2 nm Ni- 2 nm Mo sulfide sample. This large difference suggests that the vertically aligned MoS_2 is oxidized, preventing a reaction across the Ni and MoS_2 interface.

Further detailed experiments with cross-section TEM visualization of this interface are needed to understand behavior in greater detail. However, this study shows how important it is to keep the surface oxide or passivated edge sites in mind when designing any applications utilizing these metal – MoS_2 interfaces.

3.8 Conclusions

This study has presented a detailed investigation of the interactions of three different materials (Li, Ag, and Ge) on horizontally and vertically aligned MoS_2 surfaces. Li was found to reduce MoS_2 with both orientations, despite the presence of surface oxide or oxysulfide on the vertically aligned sample. Ag did not substantially react with either, while Ge showed unique behavior exhibiting a reaction with horizontally aligned MoS_2, but not with vertically aligned MoS_2. A key finding herein is that the different reaction products are likely affected both by the presence of surface defects and the propensity of the edge sites of MoS_2 to form thin oxide layers. As seen on annealing the Ni-MoS_2 systems, these surface interactions, in addition to bulk thermodynamics, likely have an impact on the extent and pathway of the interfacial transformation with different deposited materials. The transport of electrons through interfaces in electronic devices and energy storage systems will depend critically on the chemical and electronic properties of the interface, and the results of this work are useful in understanding the evolution of a variety

of important interfaces. It will be of interest in future work to relate the chemical and structural properties of these various interfaces to their electronic transport characteristics so they can be reliably engineered for next-generation devices.

CHAPTER 4. Tailoring Crystallinity of MoS_2 through Addition of Other Metals

4.1 Introduction

Alumina-supported MoS_2 is among the best materials for hydrodesulfurization (HDS) catalysis, which involves the removal of naturally-occurring sulfur from petroleum feedstock to reduce sulfur dioxide emissions.[95,96] Additionally, MoS_2 has shown promise for the electrocatalytic hydrogen evolution reaction (HER),[28,66,97,98] which is a key reaction involved in water splitting. In all of these cases, the highly anisotropic, layered crystal structure of TMDCs plays a key role in governing the properties critical for these applications. Beyond these considerations, the addition of dopants or additives to TMDCs has been shown to impact structure and properties in a variety of important ways. Industrial HDS catalysts contain promoter atoms, such as Ni or Co, which are added to the MoS_2 to enhance catalytic activity.[94,99] Previous research has shown via both STM (scanning tunneling microscopy) and DFT (density functional theory) studies that these promoter atoms are located at the edge sites of thin MoS_2 crystals, which are thought to be the active sites for catalysis as shown in Figure 34.[94,100,101] The Ni or Co species can also alter selectivity between different reaction pathways.[93] Recent work using aberration-corrected transmission electron microscopy (TEM) has also revealed important nanoscale structural details of model catalyst materials.[102,103]

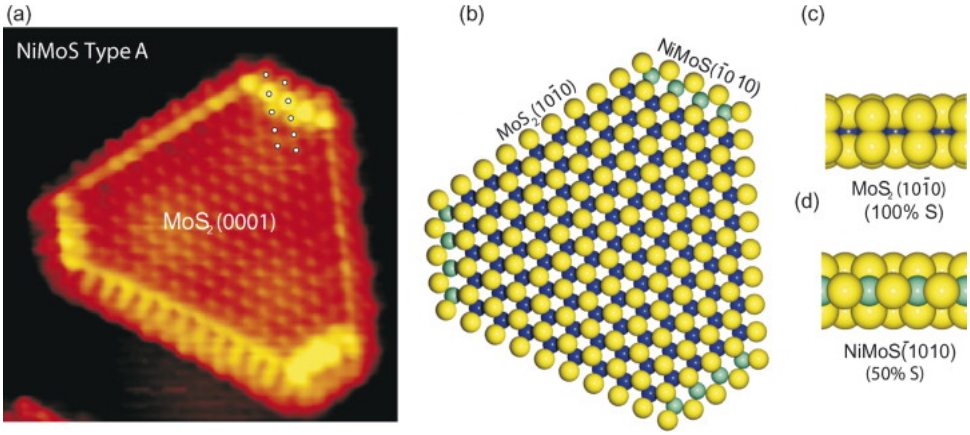

Figure 34 Atomic structure of Ni-Mo-S (a) Atom-resolved STM image of type A Ni–Mo–S (61×61 Å^2, V_t=−600 mV, I_t=−0.51 nA). (b) Ball model of type A Ni–Mo–S. (c) Side view of the MoS_2 (10$\bar{1}$0) edge. (d) Side view of the Ni–Mo–S($\bar{1}$010) edge. S: yellow, Mo: blue, Ni: cyan. Adapted with permission from reference [94]. Copyright 2007 Elsevier Inc.

A variety of transition metal atoms have been used to enhance catalytic activity in HER catalysts as well. Figure 35 shows the change in the electrochemical properties of doped MoS_2 catalysts with different transition metals affecting the current density and overpotential to different extents.[104] Substitutional or surface-adsorbing dopants are also known to affect the electronic and optical properties of thin MoS_2 materials within devices,[105–108] and the presence of other elements such as carrier agents or chemical modifiers during chemical-vapor-deposition-based synthesis of TMDCs can affect their growth.[109,110] Finally, additions of certain transition metals may be beneficial for the growth of high-quality semiconducting films, as prior work has shown that the presence of Ni or Cr can alter TMDC crystal morphology when synthesized from solid-state precursors, resulting in films with improved optoelectronic properties.[111,112]

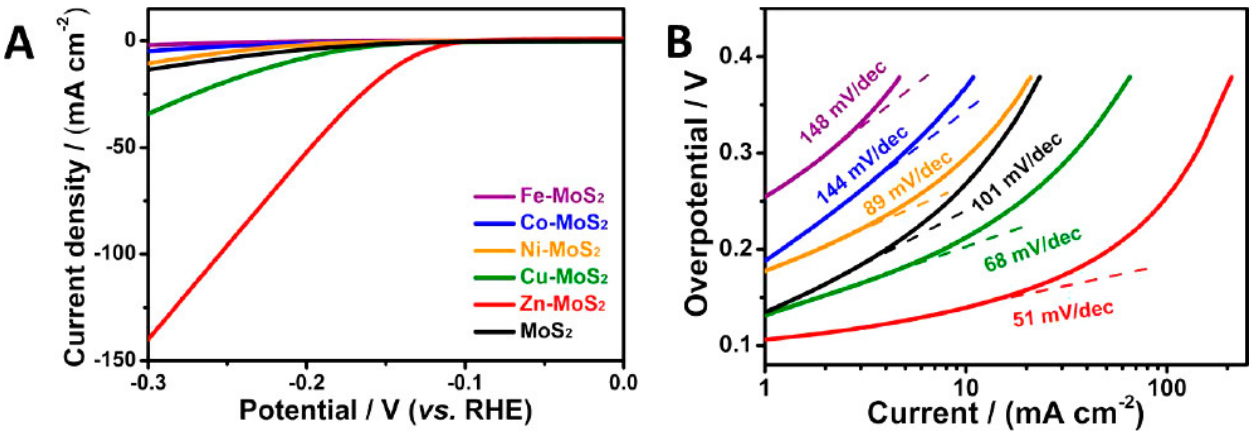

Figure 35 Electrochemical activities of various catalysts toward HER (A) HER polarization curves of various catalysts as indicated. (B) Tafel plots of the corresponding electrocatalysts derived from the early stages of HER polarization curves. Adapted with permission from reference [104]. Copyright 2017 American Chemical Society.

The most efficient catalyst would require the maximized density of these metal decorated edge sites during the synthesis of these MoS_2 crystals. These catalysts are almost always fabricated by sulfiding a mixture of Mo, Ni and/or Co oxide/metal precursors either under controlled sulfo-reducing conditions or *in situ* as in the case of HDS catalysts.[113] The sulfidation step occurs before HDS catalysis, and it is designed to transform the inactive Mo-Ni/Co precursor material into catalytically active MoS_2-Ni/Co material. Although this sulfidation step is critical for producing active nanostructures, key information regarding the relationship between the structure/morphology of the initial precursors and the final material after the transformation is often overlooked. Figure 36 clearly shows the influence of the promoter atoms, substrates and sulfiding conditions on the catalyst morphology (a) and the grain-size distribution (b). In many cases, the structure of as-synthesized TMDC materials that contain dopants or additives is known, but the processes that govern crystal evolution during synthesis are not understood. Elucidating such processes is important, since understanding the growth mechanisms of TMDC materials is key for design and fabrication of materials with optimized structure, morphology, and properties for a given application. There are relatively few attempts to actively control the final structure of

these materials while understanding the structural evolution during growth of such metal added TMDC structures.[91,114,115] Improved understanding of the dynamic materials transformations during the sulfidation process using well-defined nanostructured systems, along with new techniques to control structure and composition of complex MoS_2/transition metal materials, are necessary for the development of HDS catalysts with improved activity and selectivity.

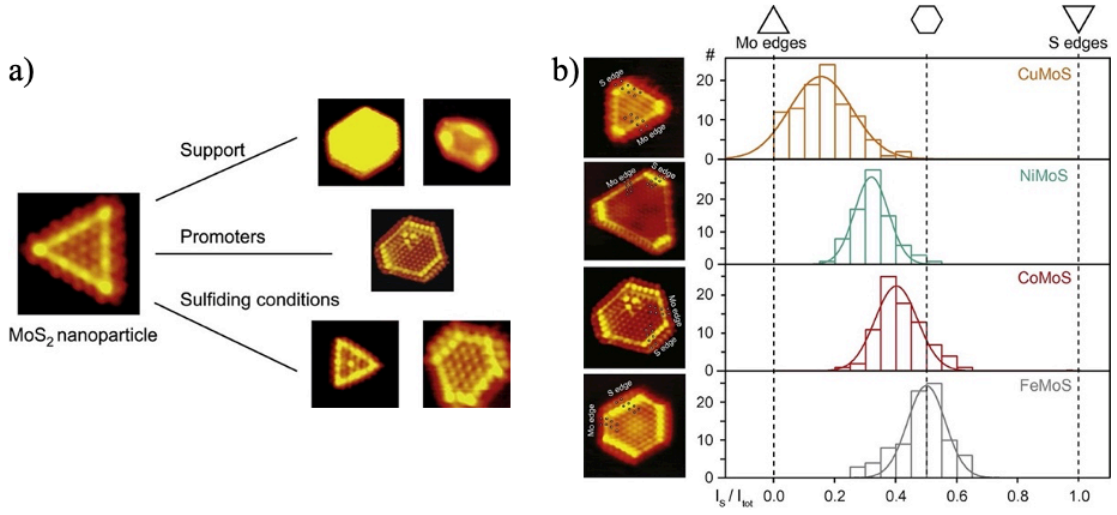

Figure 36 Crystal morphology is influenced by growth conditions a) Influence of various variables on the resulting morphology of the MoS_2 nanoparticles during synthesis - growth support, promoter atoms and sulfiding conditions. Adapted with permission from reference [100]. Copyright 2013 Elsevier Inc. b) Distribution of sulfur edge length versus total edge length with representative STM images for each promoting metal. A ratio of 0 indicates the unpromoted (triangular) MoS_2 case, whereas a ratio of 0.5 indicates a perfectly hexagonal cluster with even amounts of Mo and S edges. Adapted with permission from reference [101]. Copyright 2010 Elsevier Inc.

In situ experimental methods, such as TEM, have been used in recent years to investigate transformations in TMDC materials.[116–118] However, only a few recent studies have directly revealed TMDC growth processes from the precursor stage.[119–122] Here, we use *in situ* TEM and other *ex situ* characterization methods to investigate the effects of Ni on the dynamic crystallization and growth process of MoS_2 crystals from an amorphous precursor during heating. The addition of low concentrations of Ni causes larger crystals with different crystallographic orientations to

grow compared to the Ni-free case. In contrast, the presence of higher concentrations of Ni suppresses MoS_2 formation, instead resulting in the formation of Ni and Ni-sulfides. X-ray diffraction (XRD), scanning electron microscopy (SEM), and Raman spectroscopy confirm these results under similar *ex situ* conditions. The direct *in situ* observation of increased edge plane mobility in the presence of low concentrations of Ni indicates that the mobility of species at edge planes controls growth in this system. These results show that addition of transition metals like Ni can significantly influence the growth process of MoS_2, and this work has important implications for tailored design of MoS_2 materials for electronic and catalytic applications.

4.2 Crystallization of MoS_2 at Elevated Temperatures Investigated via *in situ* TEM

To investigate the dynamic growth process of MoS_2, *in situ* TEM experiments were carried out in which ATM ($(NH_4)_2MoS_4$), was heated inside a TEM using a single-tilt chip-based heating holder. Previous research has shown that heating of ATM under N_2 or vacuum atmosphere causes it to decompose to form MoS_2 through a two-step process (equations ***3*** and ***4***):[123,124]

$$(NH_4)_2MoS_4 \rightarrow 2NH_3\,(g) + H_2S\,(g) + MoS_3\,(s) \quad (155\,°C - 300\,°C) \qquad (3)$$

$$MoS_3 \rightarrow MoS_2\,(s) + S\,(g) \quad (300\,°C - 820\,°C) \qquad (4)$$

This precursor has been used previously to synthesize wafer-scale MoS_2 thin films using spin- and dip-coating methods, with electronic and optical properties comparable to crystalline MoS_2 grown using conventional chemical vapor deposition through sulfidation of Mo, MoO_3 or $MoCl_5$.[125–127] The advantages of precursor decomposition for MoS_2 growth include the ease of application via spin-coating, and that it does not require a sulfiding atmosphere for growth. However, it is more difficult to grow large crystals compared to CVD, and it is likely more difficult

to control thickness. Regardless, the use of the ATM precursor is beneficial herein for controlled growth of MoS_2 thin films inside the high-vacuum environment of a TEM without the introduction of additional sulfur.

We first investigated the growth of MoS_2 from ATM without any added Ni. Similar *in situ* TEM experiments detailing the growth of pure MoS_2 have recently been reported by Fei *et al*[119] ATM in n-methyl pyrrolidone (NMP) solution was drop-cast onto a ~30 nm thick SiN_x membrane on a silicon TEM heating chip and dried under vacuum, leading to formation of ATM islands with non-uniform thickness. Inside the TEM, the chip was heated from room temperature to 100 °C to remove any solvent residue, and then the chip was further heated to 900 °C in steps, with a 10 min hold every 100 °C. Additional sample preparation and experimental details are listed in section 2.4 (Experimental Methods).

Images of the growth of crystalline MoS_2 during heating of pure ATM precursor are shown in Figure 37. ATM was amorphous at 100 °C, as seen by the lack of visible lattice fringes and the diffuse intensity in the fast Fourier transform (FFT) inset (Figure 37a). Heating of ATM to 400 °C led to crystallization of MoS_2 into a polycrystalline film with (0002), $\{10\bar{1}0\}$, and $\{11\bar{2}0\}$ lattice fringes visible (Figure 37b). These few-layer MoS_2 crystals were ~2-5 nm in size, and the FFT inset shows continuous rings produced by these fringes. The material consists of crystals with random orientation; the (0002) lattice fringes that are predominantly visible correspond to crystals with vertically-oriented basal planes. Horizontally-oriented basal planes would give rise to $\{1010\}$ and $\{11\bar{2}0\}$ lattice fringes. Upon further heating to 600 °C (Figure 37c), the material largely retained this polycrystalline structure. Heating to 800 °C led to reorientation of many of the MoS_2 crystals so that their basal planes were horizontally-oriented (Figure 37d) leading to a reduction of visible (0002) lattice fringes. The reoriented MoS_2 crystals at this temperature feature small

domain sizes (~1-2 nm) with a high degree of disorder. Regions of vertically-oriented MoS_2 are also visible. The MoS_2 crystals increased in size upon heating to 900 °C, possibly due to coalescence of smaller crystals (Figure 37e). Furthermore, Mo metal particles were observed to grow from the MoS_2 at this high temperature due to the decomposition of MoS_2 ($MoS_2 \rightarrow Mo + 2S$) under vacuum. These results are largely consistent with the previous study by Fei *et al.*[119] which investigated growth of MoS_2 crystals with *in situ* TEM under similar conditions. The illustration in Figure 37f summarizes the growth of MoS_2; these results provide a baseline for comparison to precursor that contains Ni.

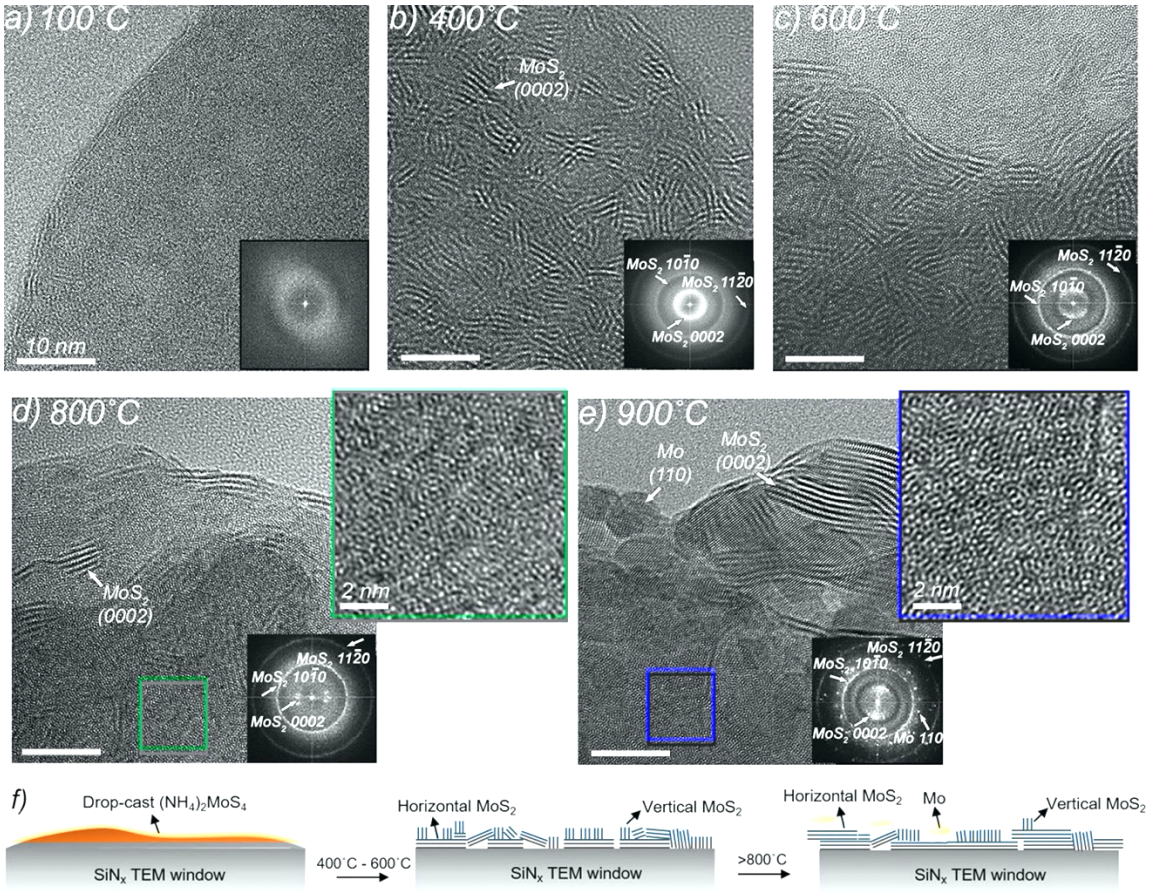

Figure 37 In situ TEM images showing the evolution of ATM precursor during heating to (a) 100 °C, (b) 400 °C, (c) 600 °C, (d) 800 °C, and (e) 900 °C. Note that each of these images is taken from slightly different locations within a region of the sample. The ATM precursor is amorphous at 100 °C, and it converts to polycrystalline MoS_2 by 400 °C. At higher temperatures, a slight increase in crystallite size is observed (d), followed by decomposition of MoS_2 to form Mo metal particles at 900 °C (e). The insets in (a–e) show fast Fourier transforms (FFTs) of these images. The bright rings in the FFTs correspond to different lattice fringes of MoS_2, which become sharper and more intense in the

images upon increasing temperature. The square insets outlined in green and blue in (d) and (e) show magnified views of the MoS_2 crystals from the marked locations at 800 and 900 °C, respectively. In both cases, the materials show small crystallite domain size and significant disorder. (f) Illustration summarizing the formation of MoS_2 crystals from the pure ATM precursor; thermolysis of the precursor results in the formation of polycrystalline MoS_2, with crystallite domains that grow in size with heating.

4.3 Crystallization of MoS_2 in the Presence of Ni Investigated via *in situ* TEM

To understand the influence of Ni on MoS_2 crystallization and growth, similar *in situ* heating experiments were carried out with Ni present (Figure 38). To fabricate these samples, a 5 nm Ni film was evaporated onto the SiN_x window, and ATM solution was then drop-cast onto it. Similar to the Ni-free case, the ATM precursor was amorphous at room temperature and at 100 °C (Figure 38a).

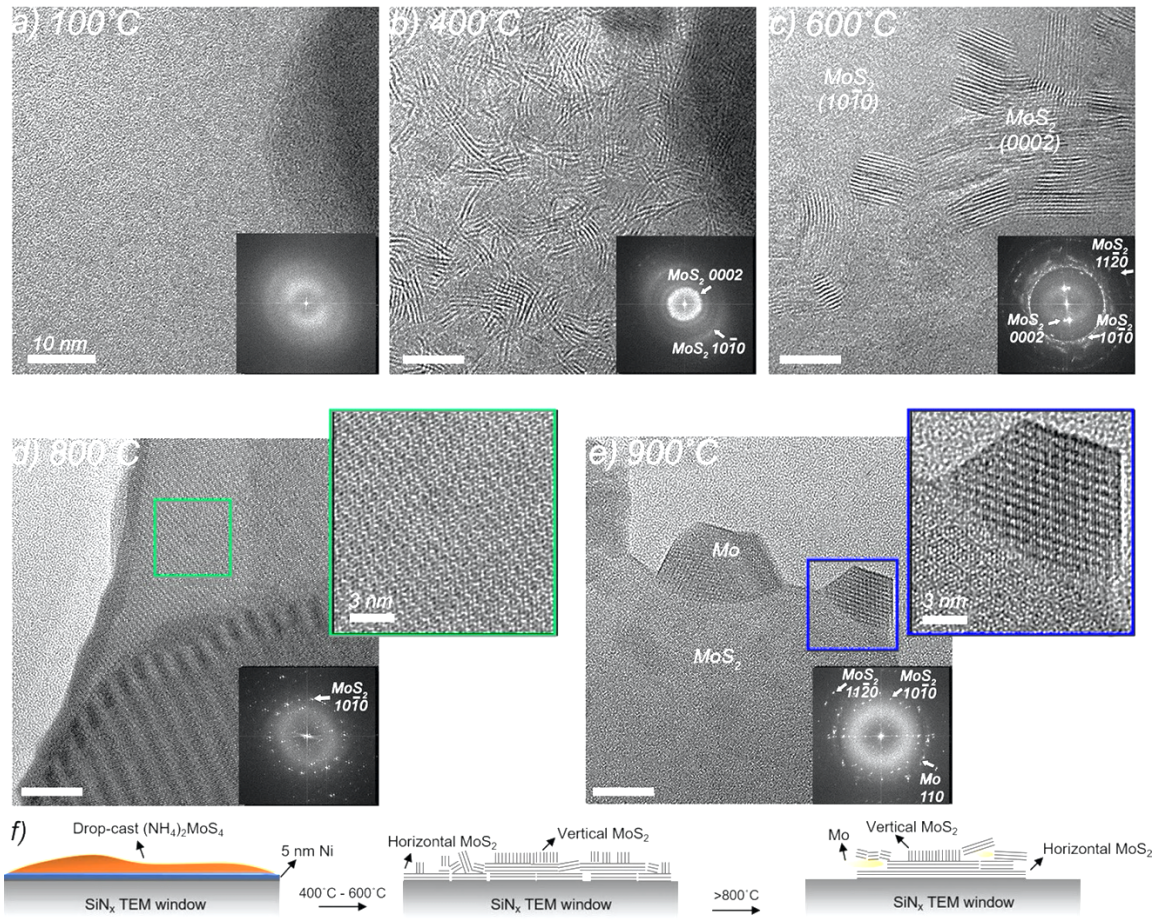

Figure 38 In situ TEM images showing the evolution of ATM precursor in the presence of a 5 nm Ni film during heating to (a) 100 °C, (b) 400 °C, (c) 600 °C, (d) 800 °C, and (e) 900 °C. Each of these images is taken from a slightly

different location from within a region of the sample. FFTs of these images are shown as insets. The ATM precursor is amorphous at 100 °C, and it converts to polycrystalline MoS_2 at 400 °C, resulting in broad and diffuse rings in the FFT. Significant crystal growth/shrinkage occurs by 600 °C (c), with the ($10\bar{1}0$) ring in the FFT indicating that much of the MoS_2 materials have basal planes parallel to the substrate. By 800 °C (d), large horizontally oriented single crystals have grown. In (d), Moiré fringes characterized by the alternating bright and dark stripes arise due to multiple MoS_2 crystals that are stacked and slightly rotated. The green rectangular inset in (d) shows a higher-magnification view of the few-layer MoS_2 crystal formed at 800 °C, while the blue inset in (e) shows a Mo crystal formed due to the decomposition of MoS_2 at 900 °C, similar to the pure ATM sample. (f) Illustration summarizing the formation of MoS_2 crystals in the presence of Ni; the initial polycrystalline MoS_2 converts to much larger, horizontally oriented crystals than in the Ni-free case.

Although not easily visible here, the thin Ni film was verified to be present in this type of sample using energy dispersive spectroscopy (Figure 39a,d). By 200 °C, the polycrystalline Ni film disappeared (Figure 39b,e), but Ni was still present according to EDS (Figure 39e) . By 400 °C, crystallization of MoS_2 occurred (Figure 38b), which is similar to the case in Figure 37 without Ni. However, differences began to emerge upon heating to 600 °C (Figure 38c). Specifically, larger MoS_2 crystals (~10–40 nm in width) formed, and both vertically oriented and horizontally oriented crystals were visible. Upon further heating to 800 °C, much larger crystals (>80 nm wide) of horizontally oriented MoS_2 formed in certain regions of the sample (Figure 38d). The FFT inset shows clusters of distinct points corresponding to $\{10\bar{1}0\}$ lattice fringes, indicating that the particle visible in this image is made up of a few horizontally oriented crystals that are stacked on their basal planes and rotated with respect to each other. Moiré fringes visible in the bottom portion of the material support this conclusion. While other large crystals such as that in Figure 38d were observed, we note that the crystal size at this stage varied, with some of the material in other regions retaining the polycrystalline form similar to that shown in Figure 38c. Upon further heating to 900 °C, the growth of Mo metal from the surface of these larger MoS_2 crystals was observed (Figure 38e), similar to the case of pure MoS_2 (Figure 38e). Thus, the *in situ* TEM measurements presented here suggest that the addition of Ni affects the size and morphology of MoS_2 crystals

during growth from the ATM precursor. Additional *ex situ* experiments that probe larger areas are discussed in Section 4.6 to corroborate these localized findings.

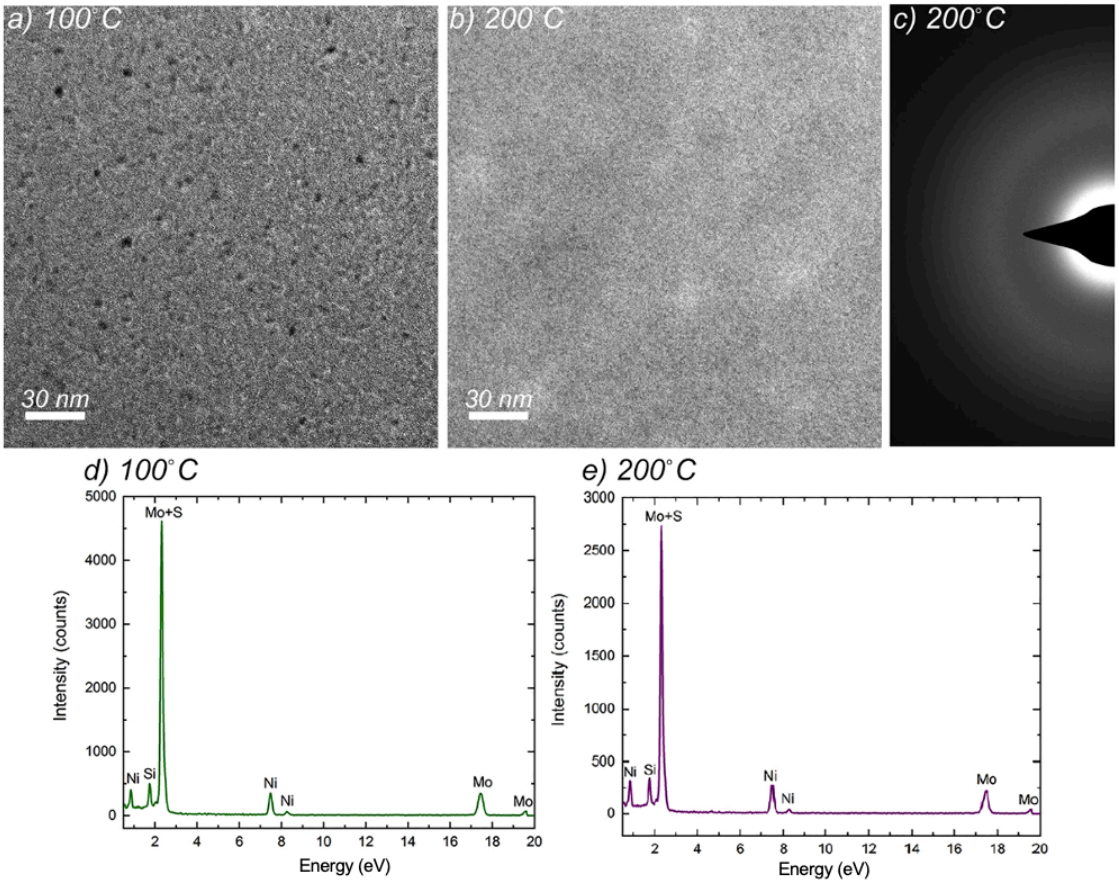

Figure 39 Low-magnification in situ TEM images for a sample with the ATM precursor in 5 nm Ni at a) 100 °C and b) 200 °C. The diffraction contrast due to polycrystalline Ni visible in (a) has disappeared at 200 °C in (b). c) The SAED pattern at 200 °C does not show any crystalline phases. EDS spectra obtained at d) 100 °C and e) 200 °C show the presence of Ni at both temperatures.

4.4 Ni Assisted MoS_2 Crystallization Dynamics

In the sample with 5 nm Ni discussed in Figure 38, interesting dynamics were observed during the heating process. Figure 40 shows the evolution of the sample while holding the temperature at 600 °C over the course of 43 seconds. At this temperature, a transition was observed in the sample: the polycrystalline MoS_2 formed at lower temperatures was undergoing grain

growth to form larger crystals. Two primary overlapping MoS_2 crystals with visible (0002) lattice fringes were initially observed (Figure 40a). With time, one crystal (outlined in red) shrank in size and eventually disappeared. This occurred *via* a process in which the edge planes at the left side of the crystal receded, while another crystal (outlined in blue) appeared to grow. This suggests that the Mo and S atoms at the edge sites of the shrinking crystal were leaving the material; these species were possibly diffusing from the crystal edge sites to join the underlying MoS_2 material that coats the substrate and/or other growing crystals. Multiple vertically oriented crystals were seen to shrink or grow in this manner, across the sample. This mechanism was only observed in samples that contained Ni, suggesting that this process was promoted by Ni species. This process is different than physical reorientation and coalescence of pure MoS_2 crystals as reported by Fei *et al.*[119] These observations thus suggest that the mobility of MoS_2 edge planes *via* the diffusion of Mo and S elemental species at ~600 °C is key for the formation of larger MoS_2 crystals. Notably, the growth of some crystals at the expense of other crystals is similar to conventional grain-growth processes in polycrystalline metals, which are governed by the energetic driving force to reduce grain boundary area.[129]

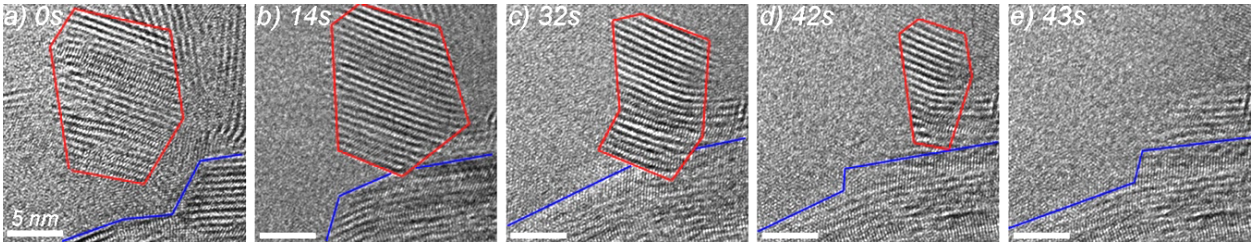

Figure 40 In situ TEM snapshots of the evolution of an individual MoS_2 crystal in a sample that initially had a 5 nm Ni film. These images were recorded during a temperature hold at 600 °C, and the elapsed time is shown at the top of each image. The red outline marks a vertically oriented MoS_2 crystal with visible (0002) lattice fringes as it shrinks, while the blue outline marks another MoS_2 crystal growing simultaneously. All scale bars are 5 nm in length.

To further analyze the differences in MoS_2 crystallization and growth with and without Ni, selected-area electron diffraction (SAED) patterns were collected during additional *in situ* heating

experiments. Figure 41 shows the evolution of the SAED patterns for pure ATM precursor. At 100 °C, only diffuse background intensity was observed from the amorphous ATM precursor and the SiNx substrate (Figure 41a). By 400 °C, the background began to sharpen (Figure 41b), corresponding to the beginning of MoS_2 crystallization. Figure 41c, d show that the rings corresponding to MoS_2 $\{10\bar{1}0\}$ and $\{11\bar{2}0\}$ increased in intensity as the temperature was increased to 600 and 800 °C. In addition, a more diffuse ring corresponding to MoS_2 $\{10\bar{1}3\}$ was also observed. All these observations are consistent with the TEM images in Figure 37.

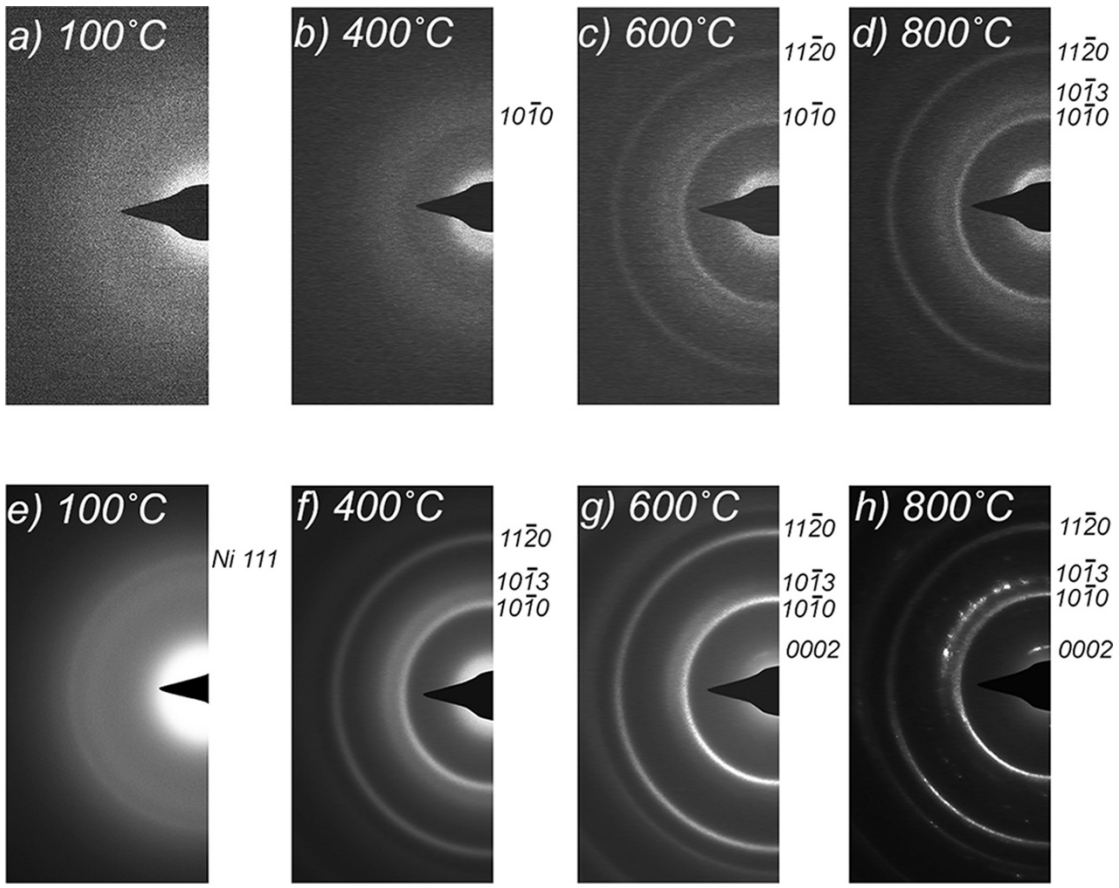

Figure 41 Evolution of SAED patterns from in situ TEM experiments of the heating of ATM precursor with and without Ni (a–d) Diffraction data from an experiment with pure ATM precursor at (a) 100 °C, (b) 400 °C, (c) 600 °C, and (d) 800 °C. (e–h) Diffraction data from an experiment with ATM precursor on 5 nm of Ni at (e) 100 °C, (f) 400 °C, (g) 600 °C, and (h) 800 °C.

Figure 41e–h shows similar SAED patterns for a sample with 5 nm of Ni. At 100 °C, a diffuse ring corresponding to Ni (111) is evident (Figure 41e), confirming the presence of polycrystalline Ni. Heating to 400 °C resulted in the formation of MoS_2 $\{10\bar{1}3\}$, $\{10\bar{1}0\}$, and $\{11\bar{2}0\}$ diffraction rings, as well as an (0002) ring that is difficult to distinguish from background intensity (Figure 41f). These rings were sharper and more intense than the pure MoS_2 sample at the same temperature, which indicates that Ni induces a greater extent of crystallinity. Importantly, the Ni {111} diffraction ring was no longer visible at 400 °C; this feature was observed to disappear after heating to 200 °C (Figure 39). This indicates that the underlying Ni was no longer present as a crystalline film, and the Ni species likely diffused into the precursor layer and/or directly reacted to form Ni sulfides. Further heating to 600 °C resulted in a resolvable but faint MoS_2 (0002) ring and increased intensity of the $\{10\bar{1}0\}$ and $\{11\bar{2}0\}$ rings due to growth of horizontally oriented MoS_2 and formation of distinct islands of vertical MoS_2 (Figure 41g). By 800 °C, the rings appear to be more directional likely due to an increase in crystallite size (Figure 41h). These observations are consistent with the TEM images in Figure 38. Circumferential integration of the SAED patterns in Figure 42 was carried out to facilitate comparison of the patterns at different temperatures. It is clear that peaks belonging to crystalline MoS_2 appear at lower temperatures for the sample containing Ni (Figure 42b).The peaks are also sharper and more intense for the Ni-MoS_2 sample implying larger crystallites confirming the previous results.

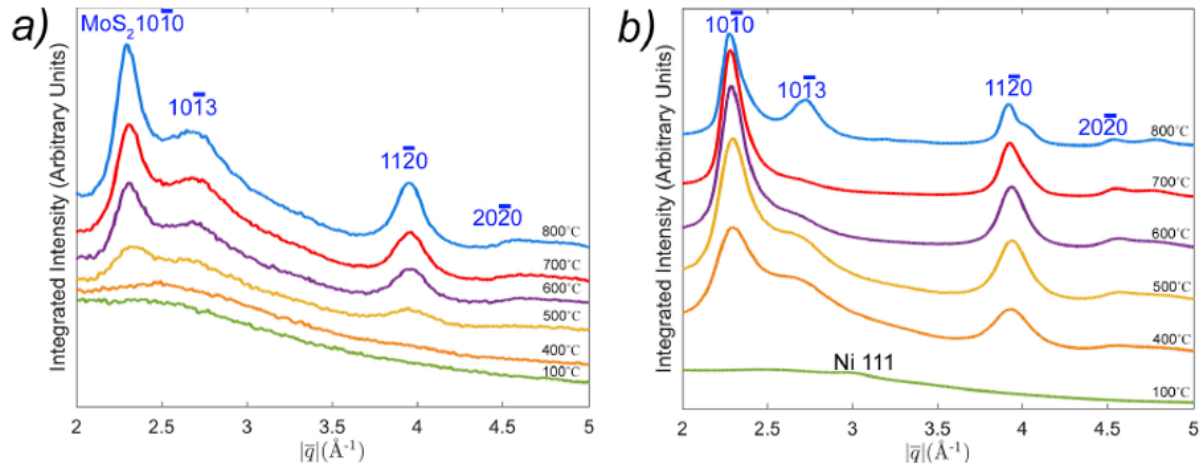

Figure 42 Circumferentially-integrated intensity as a function of scattering vector $|\bar{q}|$ from the SAED patterns obtained during heating of the a) pure ATM precursor in Figure 41a-d. Temperatures are marked on the right side of each trace. b) Circumferentially-integrated intensity from SAED patterns obtained during heating of the ATM precursor on 5 nm Ni in Figure 41e-h. Comparing the integrated plots in (a) and (b), more significant MoS_2 crystallization occurs at a lower temperature in the presence of Ni, and the crystallites are larger in size, as is evident by the sharper and more intense peaks.

4.5 Higher Concentration of Ni Disrupts MoS_2 Crystallization

With the knowledge obtained thus far, additional TEM experiments were undertaken to determine the effects of higher quantities of Ni on the evolution of MoS_2. Figure 43 shows *in situ* images from a TEM heating experiment that was carried out with the ATM precursor drop-cast onto a 30 nm Ni film instead of a 5 nm Ni film. Upon heating, this sample evolved in a significantly different way compared to the other samples shown in Figure 37-Figure 38. Instead of forming a polycrystalline MoS_2 film, this sample was dominated by growth of Ni crystals and Ni–S phases above 400 °C (Figure 43c, d). No MoS_2 was detected, although at 800 °C, a small number of Ni islands were seen to be surrounded by a layered structure that resembled onion-like MoS_2 (Figure 43e). However, the layer spacing differed from MoS_2 (5.22 Å *vs.* 6.15 Å in MoS_2). These layers are likely based on the 2H-MoS_2 structure, but their highly defective nature suggests that Ni incorporation induces disorder in these MoS_2 phases. Overall, these additional *in situ* TEM results show that the presence of greater quantities of Ni disrupts and prevents the crystallization

of MoS_2 during the decomposition of the ATM precursor, since crystalline MoS_2 was not detected in these experiments. Clearly, the amount of Ni included with the MoS_2 precursor is critical for determining growth pathways.

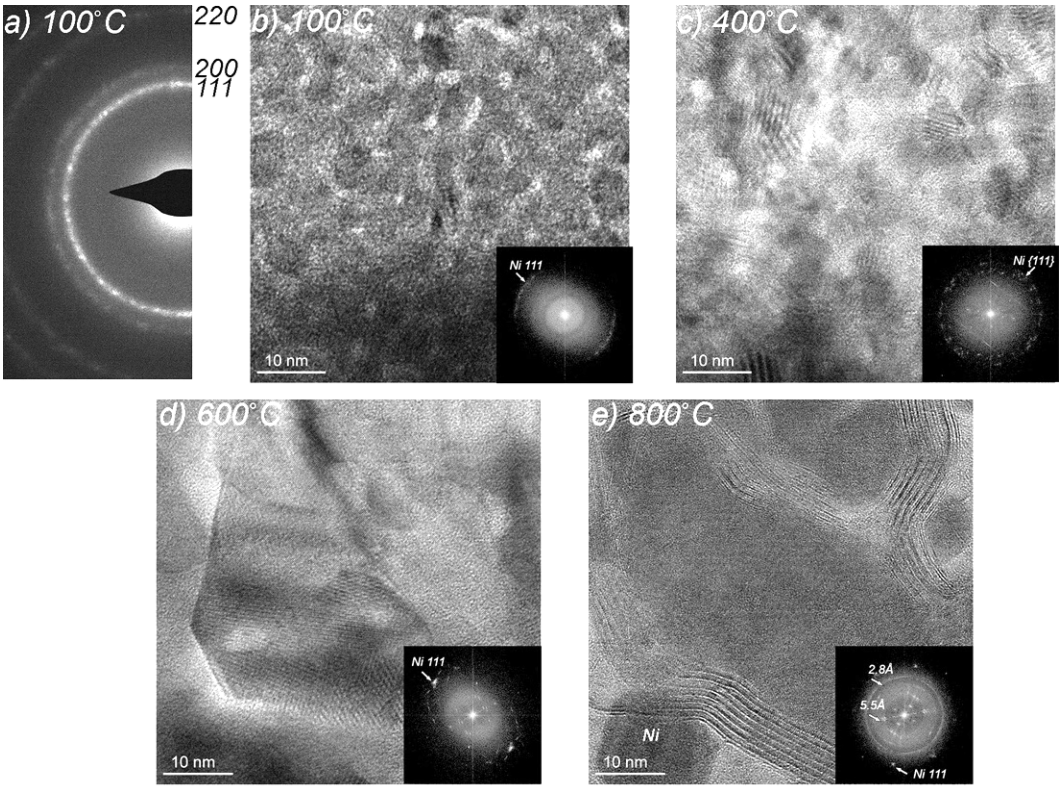

Figure 43 In situ TEM investigation of the evolution of the ATM precursor on a 30 nm Ni film during heating. An SAED pattern of the sample at 100 °C shows the presence of polycrystalline Ni. b) A TEM image at the same temperature. Upon heating, larger Ni islands form at c) 400 °C and d) 600 °C. FFT insets confirm that the islands are Ni. e) Upon heating to 800 °C, metallic Ni and Ni-S phases were observed. A MoS_2-like layered phase with different interlayer spacing than pure MoS_2 is visible in this image surrounding the darker Ni grain, but this phase was sparsely observed.

4.6 Large Scale Changes in Ni-MoS_2 Crystallization Dynamics via *Ex Situ* Characterization

The *in situ* TEM results presented herein have captured the evolution of MoS_2 during crystallization from a solid-state precursor, and they have shown that the addition of Ni plays a role in determining the size and morphology of MoS_2 crystals. The information has been obtained

from a local area of each TEM chip, and it is therefore unclear whether the observations are representative of larger sample areas. To draw conclusions about the global effect of Ni, and to corroborate our *in situ* results with independent measurements, *ex situ* characterization experiments were carried out on a larger scale. Thin films of the ATM precursor were spin coated onto ~200 nm SiO_2/Si substrates and heated to 600 °C inside an evacuated tube furnace under Ar/H_2 flow at a pressure of 1.8 Torr. This was followed by cooling to room temperature. Figure 44 shows SEM images of three *ex situ* samples that initially contained different amounts of Ni (0, 5, or 30 nm Ni films). The SEM images show that there are significant differences in the morphology of the films. Without Ni, the MoS_2 film is uniform across the wafer and the grains are too small to resolve (Figure 44a), as has been shown for other pure polycrystalline MoS_2 films.[27,29] For the sample with the 5 nm Ni film (Figure 44b), islands of MoS_2 are present which appear to feature horizontally oriented basal planes with faceted edge planes and a distribution of grain sizes (~0.5–2 μm). These islands are likely the few-layered, horizontal MoS_2 crystals observed during the *in situ* TEM heating in Figure 38d. These results are similar to a prior report showing that small amounts of Ni can lead to larger MoS_2 grain size and photoactive samples when annealing layered Mo–S thin films.[129] Finally, for the sample with 30 nm Ni (Figure 44c), a rough film with distinct large particles was observed. EDS mapping showed Ni, Mo, and S species to be present across all three samples. *Ex situ* grazing-incidence X-ray diffraction (XRD) in Figure 44d showed primarily (0002) peaks for the samples with 5 nm Ni and without Ni, indicating a preferred horizontal orientation, and the narrower (0002) peak in the 5 nm sample again suggested larger grain size. The sample with 30 nm Ni did not show crystalline MoS_2 peaks.

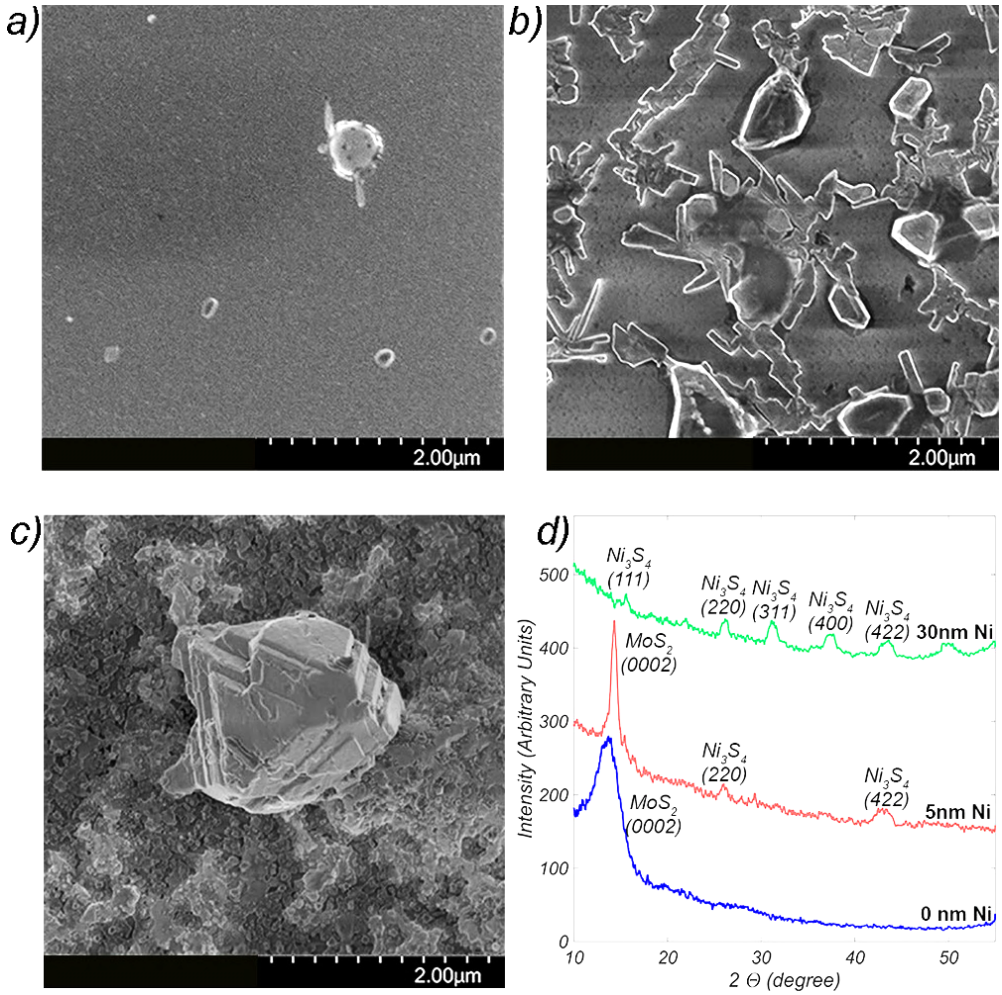

Figure 44 Ex situ samples prepared by heating precursors at 600 °C under Ar/H_2 flow. SEM images of (a) pure ATM precursor after heating, (b) a sample with ATM spin-coated onto 5 nm of Ni and then heated, and (c) a sample with ATM spin-coated onto 30 nm of Ni and then heated. (d) Grazing incidence XRD for the three samples.

Raman spectroscopy and X-ray photoelectron spectroscopy (XPS) measurements were also performed on the same samples (Figure 45), and the presence of stoichiometric MoS_2 for samples without Ni and with 5 nm Ni was further confirmed. XPS spectra for Mo 3d and S 2p (Figure 45a-b) appear to be shifted to a lower binding energy for the 5 nm Ni sample compared to the pure MoS_2 sample despite careful referencing to the C 1s peak, suggesting a possible charge transfer between the Ni and MoS_2 material. The black arrows between the S 2p peaks show that the sulfur is more reduced within the 5 nm Ni sample in comparison to pure MoS_2, and sulfur is in a higher

oxidation state for the 30 nm Ni sample (Figure 45b). The Ni 2p spectra show a mixture of oxidation states, with Ni^0 and Ni^{2+} species present in both the 5 nm and 30 nm Ni/ATM samples. As expected, no Ni signal is detected from the pure MoS_2 (Figure 45c). Raman spectra for the three samples. The A1g Raman mode shifts to a higher wavenumber (by 3 cm^{-1}) for the 5 nm Ni sample compared to the pure MoS_2 sample (Figure 45d). This corresponds to a stiffening of the Mo-S bond and could be due to the electronic doping of MoS_2 through interactions with Ni. The peaks also appear to be sharper (smaller FWHM) for the 5 nm Ni sample, which could arise from increased crystallite size or a greater number of MoS_2 layers. The lack of Raman modes arising from MoS_2 in the 30 nm Ni indicates that this phase does not form, agreeing with the *in situ* TEM data shown in Figure 43. All spectra are presented in terms of normalized intensity to aid comparison of peak shapes and positions.

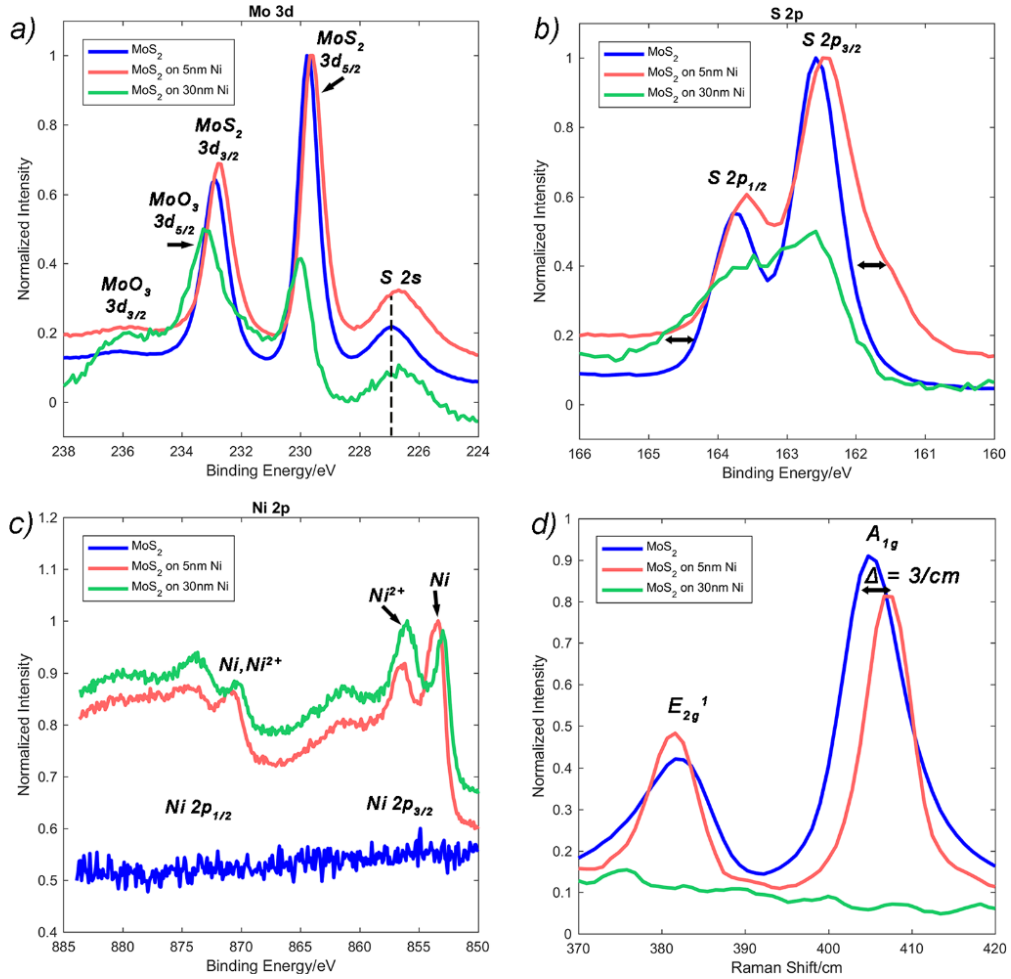

Figure 45 High resolution XPS spectra and Raman spectra from the ex situ samples fabricated from pure ATM, 5 nm Ni/ATM, and 30 nm Ni/ATM after heating to 900 °C and cooling. a) Mo 3d XPS spectra for all three types of samples. These spectra show that MoS_2 is the dominant Mo-containing phase for the pure ATM and 5 nm Ni/ATM samples, while the 30 nm Ni/ATM sample shows a mixture of Mo^{4+} and Mo^{6+}. b) S 2p XPS spectra for all three samples.

Finally, *ex situ* TEM experiments were also carried out in which the precursor was spin-coated onto SiN_x TEM grids with 5 nm Ni and heated *ex situ* under Ar/H_2 gas flow in a tube furnace. As shown in Figure 46, the presence of Ni resulted in formation of a uniform thin film of MoS_2, while the crystals grown directly on the SiN_x TEM grid were thicker islands. These similarities to the *in situ* TEM experiments indicate that although the different vacuum conditions could play a role in growth (high vacuum of TEM vs. 1.8 Torr in the tube furnace), these differences did not significantly affect the final morphology.

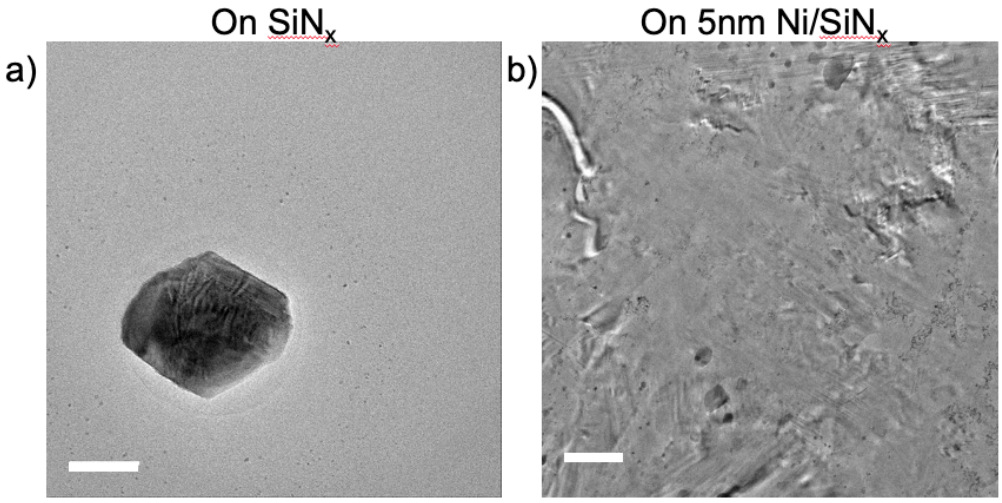

Figure 46 Ex situ TEM image of a MoS_2 film formed after heating the ATM precursor on a) SiN_x TEM grid with no Ni, b) 5 nm Ni film on the SiN_x TEM grid. Both samples were heated to 800 °C in Ar/H_2 atmosphere at 1.8 Torr in two separated runs. In b, the subtly varying diffraction contrast throughout indicates a thin film which has very fine wrinkles on the surface. A variety of other particles also present (MoS_2 and nickel sulfides).

Together, these TEM data show that the addition of a thin film of Ni alters the growth and evolution of MoS_2 during heating. However, the TEM results do not allow detection of where the Ni species reside. To investigate the atomic-scale structure of the materials synthesized in our experiments, scanning TEM (STEM) imaging was carried out with an aberration-corrected instrument operating at an accelerating voltage of 80 kV. Samples for these experiments were prepared *ex situ* and transferred to TEM grids (see section 2.5 for details). Figure 47 shows an atomic-resolution annular-darkfield (ADF) STEM image from a region of this sample, which was grown on 5 nm of Ni. This image shows single- and few-layered regions of the MoS_2 material. X-ray energy-dispersive spectroscopy (EDS) showed that Ni was distributed across the MoS_2, with greater quantities of Ni detected in clusters of material on the MoS_2 surface. However, the instrumentation and conditions used were not sufficient to resolve the presence of individual Ni atoms. In addition to being present in these clusters and on the surface, the atomic Ni is also likely

substituted at edge sites, as previously observed with STM experiments,[27,88,89], and may even be intercalated between MoS_2 layers in small quantities.

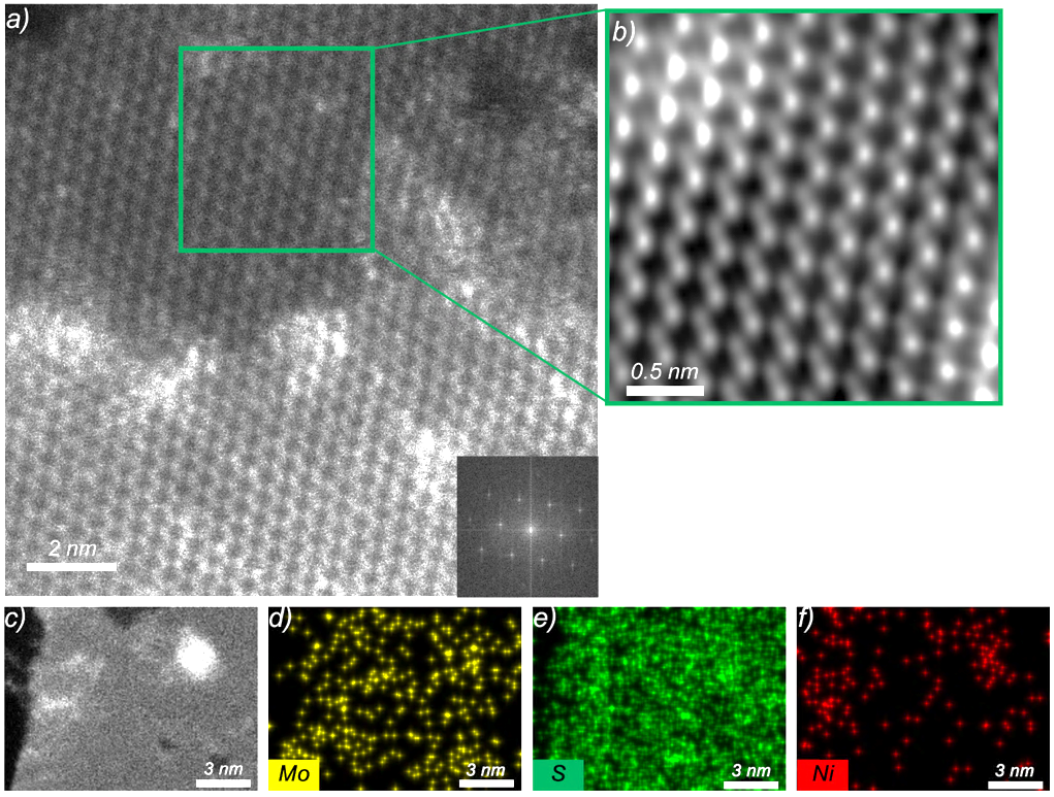

Figure 47 ADF-STEM image of a MoS_2 crystal prepared ex situ by heating the precursor cast on 5 nm Ni to 900 °C. The MoS_2 crystal shows regions of different thickness, as shown by brightness. This image was produced by processing the raw image with a Gaussian blur filter. b) A processed image showing a magnified view of single-layered MoS_2, corresponding to the region outlined in green in (a). This image was obtained by applying a low-pass FFT filter to the image in (a). c-f) STEM-EDS elemental mapping of a different region of the same sample. c) Image of the region of the sample for which EDS mapping was carried out; the dark regions are holes in the sample. Elemental maps of d) Mo, e) S, and f) Ni. While Mo and S are present across the mapped region, Ni is present in lower quantities, but with elevated quantities at the bright clusters in the image in (c).

4.7 TGA and DSC Analysis of the Gaseous Byproducts of the Reaction

Thermogravimetric analysis (TGA) and differential scanning calorimetry (DSC) were carried out to further investigate the effect of Ni on the crystallization and growth process during decomposition of the ATM precursor. In these experiments, different amounts of Ni nanopowder were added to the ATM precursor and heated at a constant rate of 20 °C/min to 900 °C under N_2 gas flow. Figure 48a shows the heat flow (in W/g) during heating of three different samples:

pure ATM, 13 wt % Ni/ATM, and 50 wt % Ni/ATM. Positive heat flow corresponds to an exothermic reaction in this plot. For all three samples, an endothermic peak at ∼230 °C is present due to the thermolysis of the ATM precursor to yield amorphous MoS_3 along with the release of H_2S and NH_3 (eq. 3). This reaction results in weight loss for all three samples in Figure 48b at a similar temperature. At ∼370 °C, an exothermic peak corresponding to the crystallization of MoS_2 from MoS_3 (eq. 4) can be observed in all three samples (Figure 48a). Parts c–e of Figure 48 show magnified views of these crystallization peaks, along with curves showing the derivative of heat flow with respect to temperature. These derivative curves highlight differences in the peak shape. The peak for pure ATM (Figure 48c) shows the presence of multiple inflection points, and the addition of increasing amounts of Ni reduces the number of distinct inflection points (Figure 48d,e). This suggests that Ni subtly alters the crystallization behavior of MoS_2 at these temperatures. Also, weight loss (corresponding to release of sulfur gas, eq. 2) occurs at this temperature for the pure ATM, but this weight loss decreases for the 13 wt % Ni/ATM sample and is negligible for the 50 wt % Ni/ATM sample (Figure 48b). This indicates that Ni reacts with excess sulfur released from MoS_3, thereby preventing weight loss. The endothermic peaks at higher temperatures for the Ni-containing samples likely correspond to phase transformations found in the Ni–S binary phase diagram.[90]

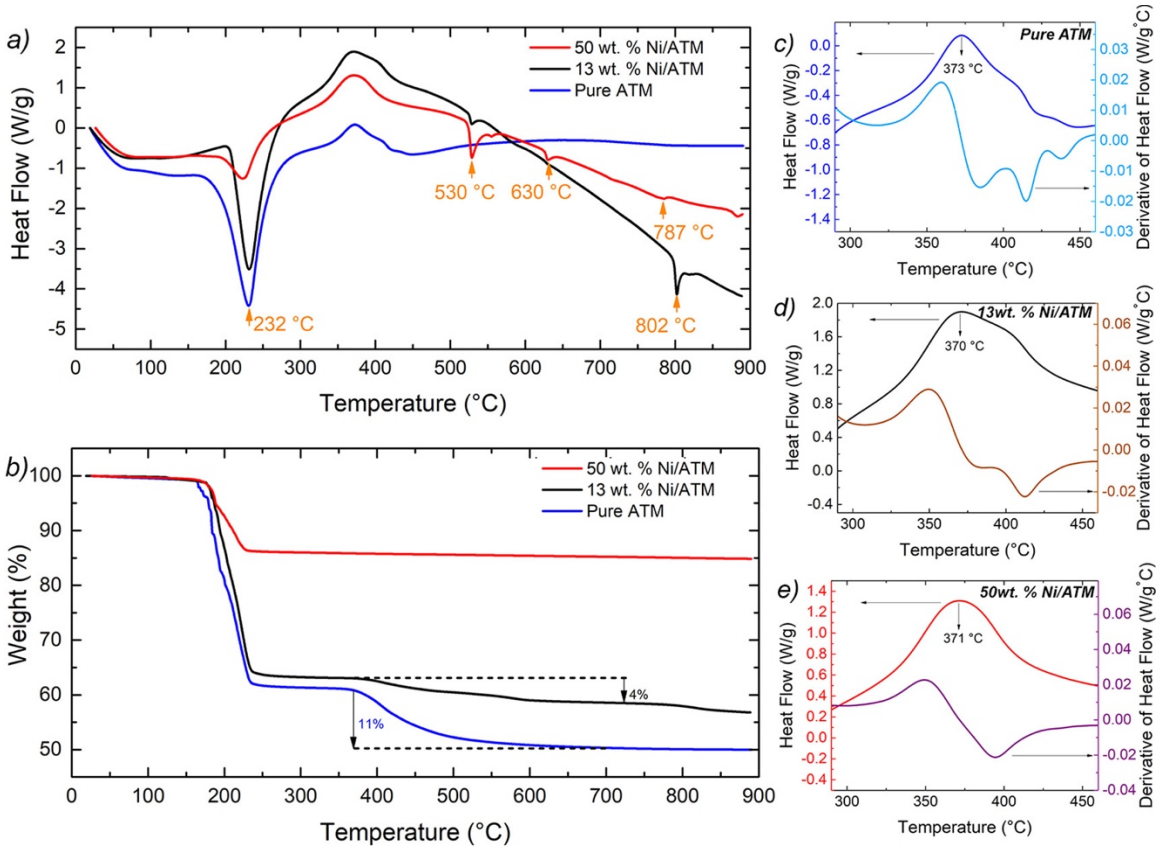

Figure 48 TGA/DSC analysis of pure ATM precursor and ATM mixed with different quantities of Ni powder (13 and 50 wt % Ni). (a) DSC heat flow across the three samples. Positive heat flow is exothermic. (b) TGA analysis shows percent weight change for the three samples as a function of temperature. (c–e) Magnified views of the exothermic peaks from (a), along with the derivative of the heat flow, for (c) pure ATM precursor, (d) 13 wt % Ni/ATM mixture, and (e) 50 wt % Ni/ATM mixture.

4.8 Postulated Mechanism of Ni-Assisted MoS_2 Crystallization

The comprehensive *in situ* and *ex situ* results presented herein provide abundant evidence that Ni acts to affect the evolution of crystal size and morphology during growth of MoS_2. In particular, the addition of small amounts of Ni to the solid-state ATM precursor results in the formation of larger MoS_2 crystals with a preferred horizontal orientation. Here, we postulate a mechanism based on our results and prior literature. During heating, Ni was observed to diffuse into the amorphous ATM precursor at about 200 °C, as indicated by the disappearance of the Ni diffraction ring from the SAED pattern (Figure 42). Ni exposed to the H_2S and S released from the

precursor during heating could become sulfided to form nanoscale Ni–sulfide clusters present at the surface of crystals or at grain boundaries between MoS_2 crystals. Although such clusters were not detectable in the *in situ* TEM experiments, the TGA/DSC provided evidence for the reaction of Ni with excess sulfur, and the STEM results suggested Ni was present in clusters. In addition to forming sulfide clusters, Ni atoms are known to be incorporated into MoS_2 crystals by substituting at edge sites,[88,94,100,130]indicating that Ni atoms would tend to substitute at edge sites throughout the polycrystalline mixture. Previous work by Lauritsen *et al*[94] and others[88,89,100,130–132] has investigated the structure of Ni-substituted MoS_2 materials in detail because of their importance for HDS catalysis. Scanning tunneling microscopy (STM) and DFT calculations have shown that Ni substitutes for Mo atoms at S-terminated edge sites, altering their structure and resulting in Ni–MoS_2 crystals with truncated triangular and dodecagonal morphologies on Au substrates.[100] Krebs *et al.* showed that certain Ni-substituted edge planes have surface energies that are significantly lower than the unsubstituted, pure Mo-terminated edge site.[132] The edge structure and Ni concentration are also expected to vary with temperature and chemical conditions (*e.g.*, the chemical potential of sulfur in the system).[100,132] Several papers[91,111,114,133–137] have also suggested the possibility of liquid NiS_x phase forming which allows for the overlayer of MoS_2, WS_2, or WSe_2 crystallites to be more mobile, resulting in larger domain sizes. This is referred to as van der Waals Rheotaxy (vdWR) and is based on the observation that when sulfur reacts with Ni, a Ni–S eutectic forms with 33 at% of S which has a relatively low melting point (635 °C) and hence must be a liquid phase above this temperature at 1 atm pressure.[138] Regula *et al.* also performed an *in situ* TEM study, starting with sputtered, amorphous Ni-WS_x and observed the formation of > 1 μm WS_2 crystallites in the presence of Ni.[91] They proposed that NiS_x phase forms on reaction with S, as the WS_x loses its excess sulfur atoms to form small, disordered crystallites. These NiS_x crystals,

which are liquid above 600 °C, then allow for the dissolution of the WS_2 crystals and grow laterally from the saturated solution.

However, we observe Ni-assisted MoS_2 crystallization at temperatures of 400 °C, which is below the eutectic melting point for the bulk NiS_x phase. By 200 °C, Ni is homogenously distributed throughout the MoS_2 film (Figure 39). It can be assumed that Ni is located at the edges of the MoS_2 crystallites, as has been shown previously.[88,94,100,130] Here we postulate the modification of MoS_2 edge planes by Ni atoms not only changes their surface energy but also can alter their mobility during the crystallization and growth process of polycrystalline MoS_2. This has been seen in Al-Si systems where aluminum atoms assist crystallization of amorphous silicon.[139] This has been calculated to be due to diffusion of aluminum via interstitial resulting in broken covalent bonds and hence higher atomic mobilities, which favor the crystallite growth.[140] As in any system with interfaces or grain boundaries that naturally have higher energy than the bulk crystal, there is a thermodynamic driving force for the growth of the MoS_2 crystallites to reduce interface volume in the polycrystalline films. Ni-substituted MoS_2 edge plane structures could enable easier movement of the edge planes during MoS_2 crystal growth due to increased disorder, greater free volume, or different bonding characteristics at these interfaces. This would allow for Mo and S atoms to be transported across these interfaces more readily to be added to a growing crystal or removed from a shrinking one, and the moving interfaces themselves could then be transported to and annihilated at free surfaces. In our experiments without Ni, the MoS_2 crystals grew only a small amount during heating. In the samples with small amounts of Ni, the crystals grew to be much larger, and we directly observed the movement of edge planes during the simultaneous shrinkage and growth of individual MoS_2 crystals (Figure 40), which was not observed in any experiments on pure MoS_2. This observation suggests that the mobility of edge

planes plays a key role in the growth process. It is expected that the edge structure and chemistry change as Ni and S are dynamically incorporated and removed during crystal growth/shrinkage, and this could further impact the edge plane mobility. These processes could also be influenced by the presence of Ni–sulfide clusters at interfaces. In short, while it is the balance of edge-plane energies that determine the final shape of the MoS_2 crystals, the ability and rate of the various crystal surfaces to accommodate growth or shrinkage appear to play a key role here in the evolution of this TMDC material.

4.9 Investigation of Irradiation Effects from the Electron Beam

Beam irradiation can cause radiolysis, heating and/or knock-on damage in TMDCs.[141–143] As mentioned in the main text, we performed additional control experiments to assess the influence of the beam on the crystallization and growth processes of the ATM precursor. First, the effects of electron beam exposure on the amorphous ATM precursor with 5 nm Ni were studied at room temperature (Figure 49a-h). Two distinct positions were identified on the sample. For Position 1, the electron beam was kept OFF until an image was to be captured, which was at a regular interval of 5 min at 20 °C (Figure 49a-d). Position 2 was continuously illuminated by the beam (dose rate of 478 mA/cm^2) for 15 min, with images being recorded at an interval of 5 min (Figure 49e-h). Both cases are visually identical, and the continuous beam exposure did not cause crystallization of the amorphous precursor to occur. The TEM chip was then heated to 200 °C at a rate of (2 °C/s), and the sample was illuminated continuously for another 15 min at 200 °C. This temperature was intentionally chosen to be below the MoS_2 crystallization temperature of ~400 °C to determine if local illumination resulted in crystallization at a lower temperature.[119,123,124] No MoS_2 crystallization was observed during the continuous beam exposure, as shown in Figure 49i-l.

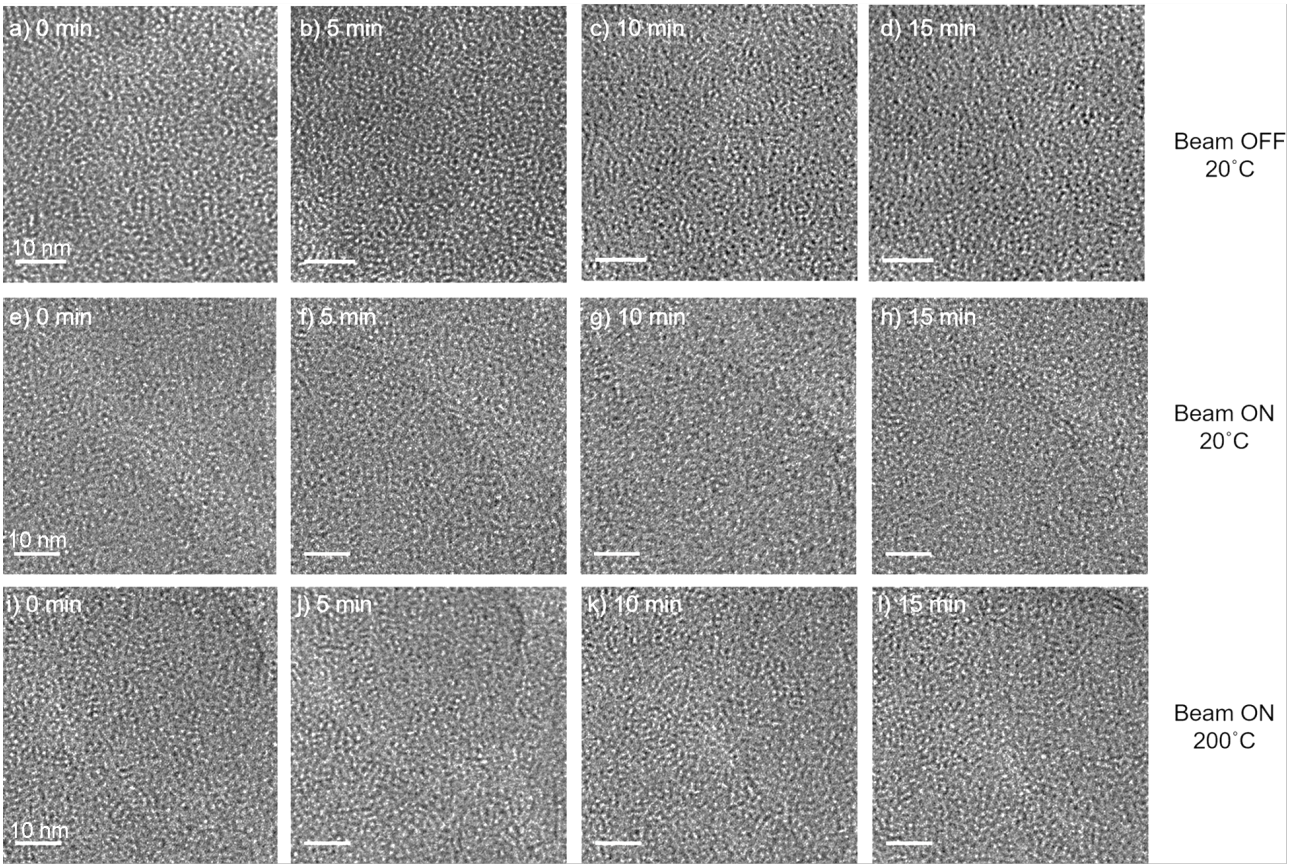

Figure 49 Control experiments with ATM precursor deposited on a 5 nm Ni film exposed to an electron beam. (a-d) Images recorded every 5 min at 20 °C at position 1, where the beam was blanked between image recording. (e-h) Images recorded at position 2 at 20 °C during which the beam continuously illuminated the sample. (i-l) Images recorded at 200 °C during continuous beam exposure. There is no noticeable influence of the beam on crystallization under these conditions.

The possible influence of the beam on the growth processes of the MoS_2 crystals was also assessed. The precursor was heated to 400 °C to allow for initial crystallization and formation of vertically aligned MoS_2 crystals, followed by cooling down to room temperature. Cooling to room temperature was necessary to isolate the influence of electron beam effects from temperature effects; prior work has used such control experiments at room temperature as a stability criterion as well.[119] The sample was then continuously illuminated for 15 min, and Figure 50 shows that the electron beam induced no significant changes in the crystallinity during this period. Similar results were obtained after heating to 800 °C and cooling to room temperature (Figure 50e-h). While it is

difficult to decouple temperature-induced effects from possible beam effects at higher temperatures due to the significant influence of temperature on growth processes, these results strongly suggest that temperature plays the dominant role in the crystallization and growth of this material and that any possible beam effects do not change our conclusions.

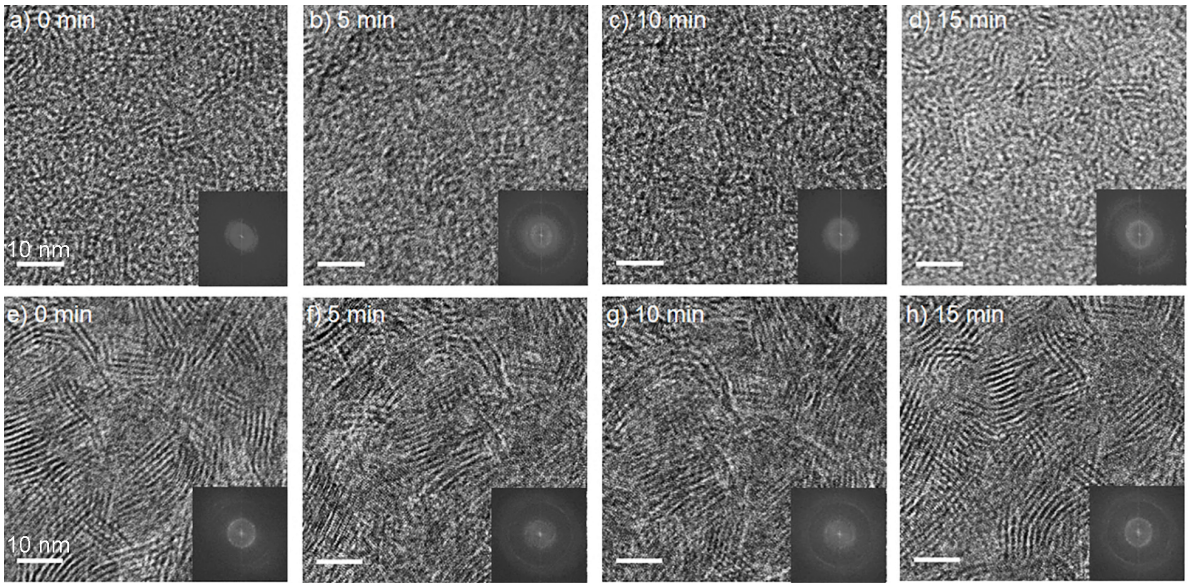

Figure 50 Continuous beam exposure of MoS_2 crystals formed from ATM precursor on 5 nm Ni under different conditions. (a-d) Images under continuous beam exposure after heating to 400 °C and cooling to 20 °C. (e-h) Images under continuous beam exposure after heating to 800 °C and cooling to 20 °C. Data are not presented at higher temperatures because of significant thermal drift and the difficulty in deconvolution of possible beam effects.

4.10 Solution Doping with Other Transition Metals and their Influence on the Crystallization Dynamics

All the experiments discussed so far have utilized a thin film of Ni as a substrate on which MoS_2 thin films are grown. However, for precise control of Ni concentration and optimization of the morphology of the resulting MoS_2 film, solution doping of the MoS_2 precursor using Ni salts is the preferred method. One-pot hydrothermal synthesis of Ni-doped MoS_2 is commonly used to fabricate the activated Ni-MoS_2 catalyst complexes.[144–146] Ni solution doping also allows for use of very low concentrations of Ni species to be added to the precursor solution, an important

measure taken to prevent the formation of large NiS_x islands. This is important to control the surface roughness and grain boundaries across the MoS_2 thin film, especially for its few-layer optoelectronic applications.

Figure 51 shows GIXRD curves for four samples – pure MoS_2, 1:2 Ni: MoS_2, 1:1 Ni:MoS_2 and 2:1 Ni:MoS_2 (5 wt.% solution). All samples were prepared identically otherwise following the spin coating method utilized for preparation of *ex situ* samples discussed in section X. With increasing concentration of Ni, the FWHM of the (0002) peak or the crystallite size of the horizontally aligned MoS_2 crystals increases. From these data, it is clear that when dissolved in solution, the Ni similarly alters the MoS2 crystallization pathways as the Ni thin films. These samples likely showed larger MoS_2 crystallites due to the presence of NiS_x clusters around the grain boundaries, as suggested by Brunken *et al.*[114]

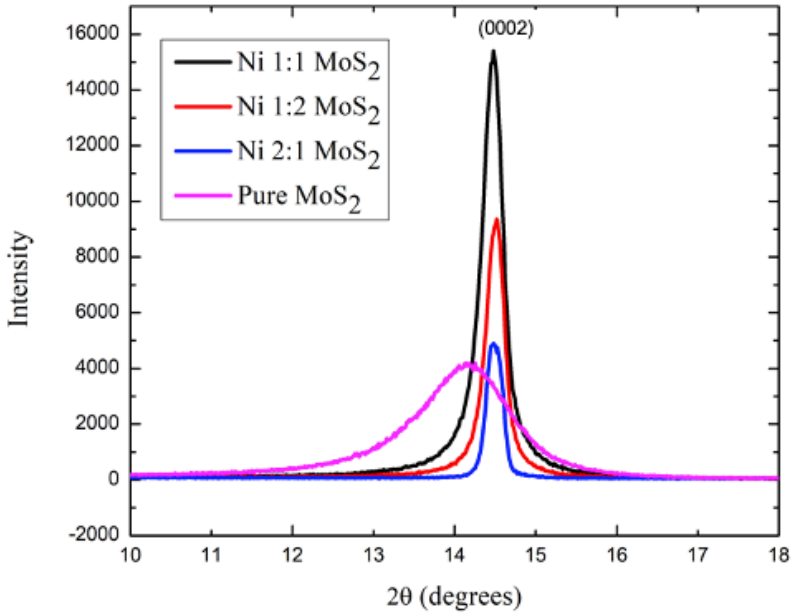

Figure 51 Solution doped Ni-MoS_2 a) GIXRD curves showing the (0002) MoS_2 peak for pristine and solution doped MoS_2 with different concentrations of Ni – 1:1 Ni: MoS_2, 1:2 Ni:MoS_2 and 2:1 Ni:MoS_2. Increasing concentration of Ni results in progressively lower FWHM of the crystalline MoS_2 peak which confirms that the addition of Ni results in increased MoS_2 crystallite size even for these solution doped samples.

A series of other transitions metals were also studied via their introduction into the MoS_2 precursor solution. Figure 52a shows the GIXRD curves for pristine MoS_2 films and those doped with Fe, Co, Ni, or Cu in solution. The FWHM of the (0002) MoS_2 peak is significantly narrower than that of the pristine MoS_2 for the Ni-doped MoS_2, while it is broader for the Co-doped MoS_2, implying worse crystalline properties for that sample. The SEM images (Figure 52b-e) show that the morphology of these films is different. The Fe doped MoS_2 shows several ~ 1-5 µm FeS_x islands, while the others show a more uniform morphology. These results show that the nature of the transition metal used could alter the crystallization pathways to different extents, with Ni showing clear benefits in promoting MoS_2 crystallization.

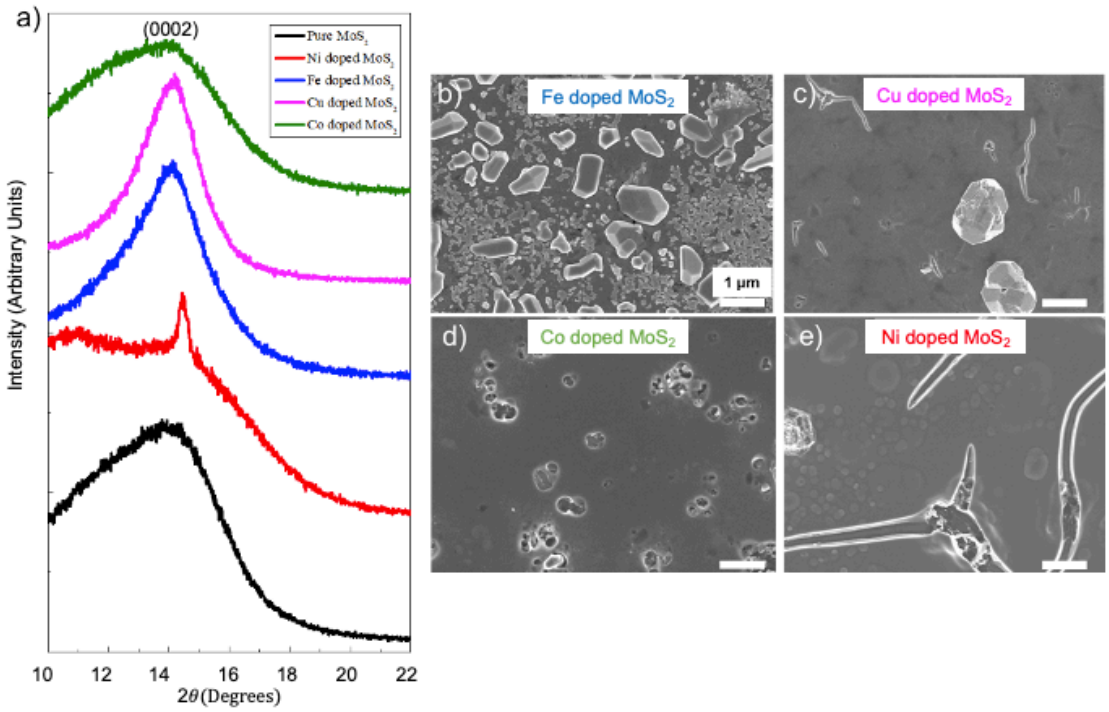

Figure 52 Solution doping MoS_2 with different transition metals GIXRD curves for pristine and solution doped MoS_2 with Ni, Co, Fe, and Cu. SEM images for b) Fe c) Cu d) Co e) Ni-doped MoS_2. he morphology varies distinctly between the samples.

4.11 Conclusions

This study elucidated the dynamic evolution of MoS_2 crystals during crystallization and growth from a solid-state precursor, and it showed how additions of small amounts of another transition metal influence this process. The combination of *in situ* and *ex situ* measurements provided strong evidence that Ni alters MoS_2 crystal growth. These results will help to fill a knowledge gap that exists regarding the engineering of TMDC materials: prior work has provided an understanding of the atomic-scale structure of active TMDCs for catalysis and optoelectronic applications, but the best pathways to synthesize and engineer these materials are not always clear. In particular, understanding the effects of Ni on MoS_2 crystallization and growth at the nanoscale, as presented herein, could enable the design of synthetic pathways for MoS_2-based systems, as well as other few-layer TMDCs. These findings provide a basis for future engineering of MoS_2 grain size and morphology *via* the addition of Ni and other transition metals, which could be important for a range of applications, including HER catalysis and next-generation electronic and optical devices. Future work could explore detailed atomic-scale information regarding the presence of Ni atoms within the MoS_2 lattice, along with the correlation of observed dynamics to energetic barriers through simulations. This will enable a fundamental understanding of the mechanisms through which Ni may alter MoS_2 edge plane mobility.

CHAPTER 5. Selective Growth of MoS_2 Crystals on Patterned Metal Thin Films

5.1 Introduction

As shown in Chapter 4, interfacing MoS_2 with other metals can significantly alter the nucleation and growth pathways of MoS_2 thin films. Several studies have demonstrated the use of different metals as seeds for the growth of TMDC large-area single crystals through CVD.[147–160] Unlike catalysis where TMDC nanoparticles with activated edge sites are preferred, optoelectronic devices with TMDC crystals are negatively affected by the presence of grain boundaries which serve as scattering sites for electrons. Hence, even with the increased particle size, the few-layered spun-coat Ni-MoS_2 thin-film synthesized through thermolysis of the $(NH_4)_2MoS_4$ precursor solution did not demonstrate improved electronic properties.

For optimized device performance, the synthesis of wafer-scale of single-crystalline TMDCs at controlled locations is important. This has been previously demonstrated through the use of metallic seed crystals. For instance, 10-50 μm wide WS_2 crystals have been nucleated using precisely positioned array of circular Au seeds, 20 nm thick and 4 μm in diameter, as shown in Figure 53a.[154] The Au particles/films are postulated to allow the onset of nucleation of WS_2 crystals (Figure 53b) due to a lowered nucleation barrier across the Au-SiO_2 interface. The free energy needed for the heterogeneous nucleation can be expressed through equation *(5)*:

$$\boldsymbol{\Delta G_{Hetero} = \Delta G_{Homo} * f(\theta)} \qquad \textit{(5)}$$

where $f(\theta) = 1/2 - 3/4 \cos\theta + 1/4 \cos^3\theta$, ΔG_{Homo} is the free energy needed for the homogeneous nucleation and θ is the contact angle between the nucleation site and the material being grown.[161] Heterogeneous nucleation across a seeding atom could allow for conditions where $0 < f(\theta) \leq 1$, implying that the incoming atoms from the precursor preferentially nucleate from the seed's edge. This possibly is also the reason why we can grow MoS_2 at lower temperature in the presence of

seeding promoters like Perylene-3,4,9,10-tetracarboxylic acid tetrapotassium salt (PTAS), Copper(II) hexadecafluoro phthalocyanine ($F_{16}CuPc$), etc., but with less spatial control.[162] Without the presence of a seed, nucleation is random, and as a result, the crystal size is smaller (Figure 53c). On the other hand, the spatial control of these Au-seeded single WS_2 is crystals higher with the introduction of the Au seeds. A combination of multilayer and single-layer WS_2 can be seen due to relative ease of formation of multilayers around the Au seed (Figure 53d-f).

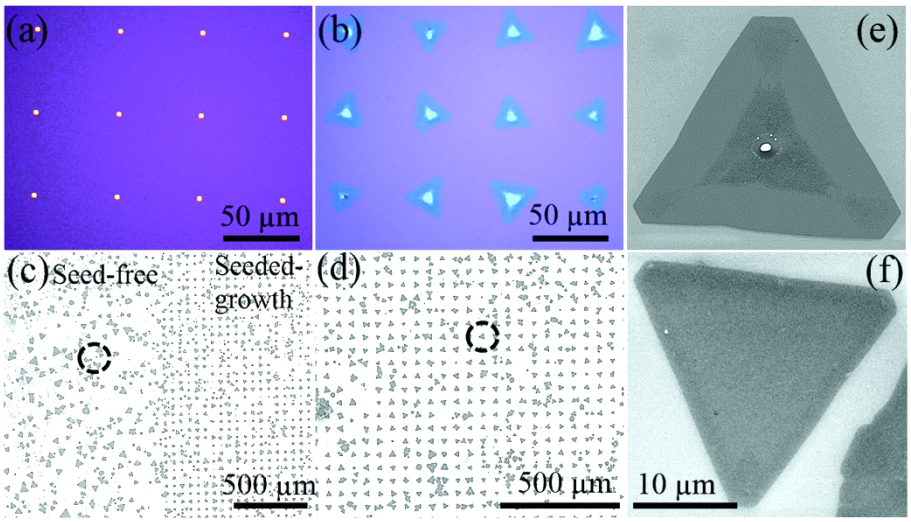

Figure 53 Growth of Au seeded WS_2 atomic layers. Typical optical micrographs of (a) lithography patterned Au islands, and (b) WS_2 domains grown from Au seeds. Typical low magnification SEM micrographs of WS_2 domains from (c) randomly grown, and (d) arrayed regions. Reproduced by permission of The Royal Society of Chemistry from reference[154].

Several other studies have shown this seeding behavior with different metal atoms. While metals like Cr/Ti, Au, Ni, and Cr allow for seeded growth of different TMDC layers, other metals like pure Pd do not.[148] This implies that the nature of the metal-TMDC interface and the relative cohesive (TMDC to TMDC) *vs*. adhesive (metal to TMDC) energies play an important role in assisting this seeding process. Li *et al.* highlight this importance with cross-section TEM images of the Au seed and MoS_2 interface (Figure 54).[152] They postulate the onset of nucleation from the Au–SiO_2 interface, where the layers then grow along the Au seed via atomic diffusion to finally

form an encapsulated MoS_2 shell. DFT calculations reveal that the deposition of MoS_2 on Au-decorated SiO_2 is a thermodynamically favorable process, as has been widely proven in recent studies on 2D material synthesis.

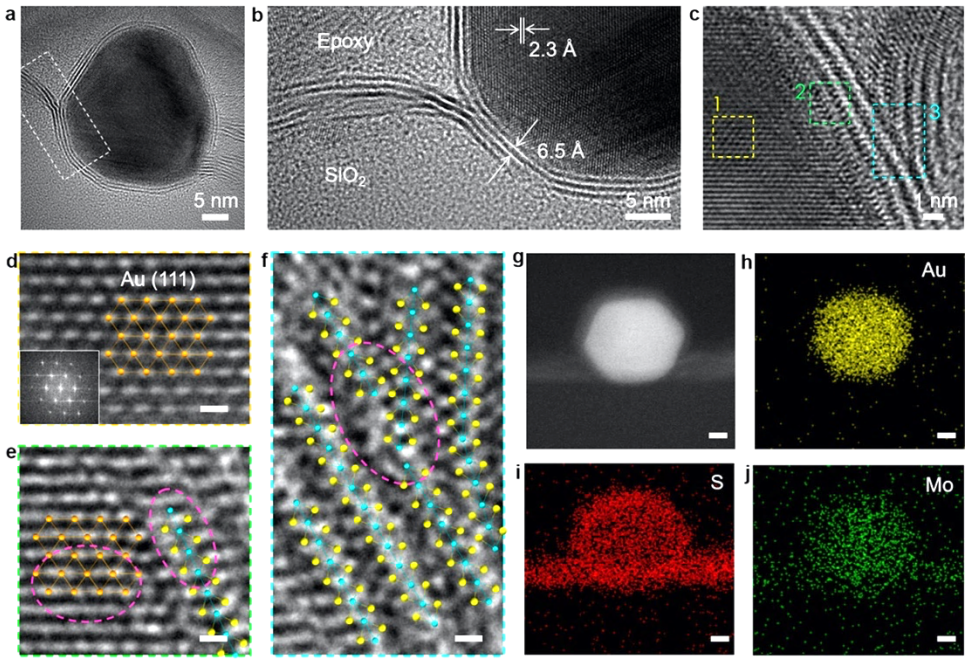

Figure 54 TEM visualization of the seeding role of Au nanoparticles (a, b) Cross-section TEM images of the MoS_2-encapsulated Au seed. (b) Dotted region in (a). (c) High-resolution TEM images showing the bifurcation of a MoS_2 shell and planar sheet. (d–f) Atomic structures corresponding to dotted regions 1–3 in (c), respectively. The fast Fourier transform (FFT) pattern inset in (d) indicates the (111) plane of Au, and the pink dotted circles in (e) and (f) indicate the observation of lattice distortion. Scale bar: 0.25 nm. (g–j) STEM image (g) of the encapsulated Au seed and the corresponding EDS maps (h–j). Scale bar: 10 nm. Adapted with permission from reference[152] Copyright 2018 American Chemical Society.

This research seeks to further combine the knowledge of seeding TMDC growth with metals and altering crystallization pathways during growth as shown in the Ni-assisted MoS_2 growth demonstrated in Chapter 4. In this study, a combination of knowledge from these experiments and previous studies is used to selectively grow MoS_2 on Ni channels, while inhibiting growth on Au contacts. Unlike Au seeding in previously discussed papers, this study shows that MoS_2 preferentially grows on Ni rather than on Au or the SiO_2/Si substrate. It is important to note

that this is in contrast to the DFT calculations of surface energy discussed earlier.[152] This unique selectivity across a repeatable array of Ni-Au patterns allows for the possibility of single-step synthesis of wafer-scale patterning of MoS_2 in a back-gated transistor configuration with MoS_2 selectively deposited over the Ni channels, and with Au contacts to the channel fabricated with virtually no photoresist residue across the interface, as there are no photolithographic steps in between. We show below that this behavior is highly dependent on the concentration of the precursor in the gas phase, and at higher concentrations, the selectivity is not as pronounced because the vapor phase reactants saturate the surface sites.

5.2 CVD Growth of Single-Crystalline MoS_2 on Evaporated Ni and Au

First, to investigate the influence of Ni and Au on the morphology of the CVD grown MoS_2 single crystals, control samples with 1 nm Ni and 20 nm Au thin films on SiO_2/Si substrates were fabricated and compared to that on bare SiO_2/Si substrates (thermally grown oxide, 300 nm thick). The experimental methods section discusses this procedure in greater detail (Section 2.2.2). Figure 55a shows the resulting MoS_2 crystals with a domain size of ~1-5 μm and single to few-layered thickness. The process resulted in random and very high nucleation density of crystals across the substrate. Hence, the domain size is limited in this process. The yellow rectangle highlights the region from where the Raman spectrum (SiO_2 without Ni) is captured (Figure 55c). On the other hand, Figure 55b makes it undoubtedly clear that Ni has a significant impact on reducing nucleation density and increasing the domain size of these crystals. The crystals have an altered morphology with thicker, more randomly oriented edges. This could be due to the presence of liquid NiS_x or Ni decorated edges with enhanced mobility, as discussed previously in Chapter 4. With ~20 μm domain sizes, this enhanced mobility across the edges results in ~10 times larger

crystal sizes consistent with the *in situ* TEM observations with Ni-doped $(NH_4)_2MoS_4$ thin films (Figure 40). Strong Raman peaks seen in Figure 55c confirm the presence of crystalline MoS_2 and the PL spectrum shows the presence of few-layer MoS_2 (Figure 55d). The black dots seen across the rest of the SiO_2/Si wafer (Figure 55b) are likely NiS_x regions. This can be expected because the sulfur vapor pressure is maintained to be significantly greater than that of MoO_3 and the 1 nm Ni thin film across the surface is exposed to this sulfur vapor during the CVD process. The Raman spectrum captured over the black dots (orange rectangle region, orange curve in Figure 55c) suggests that these are not crystalline MoS_2 particles. Care was taken to reduce the sulfur vapor pressure (lesser sulfur powder used) in the furnace for the subsequent runs discussed hereafter.

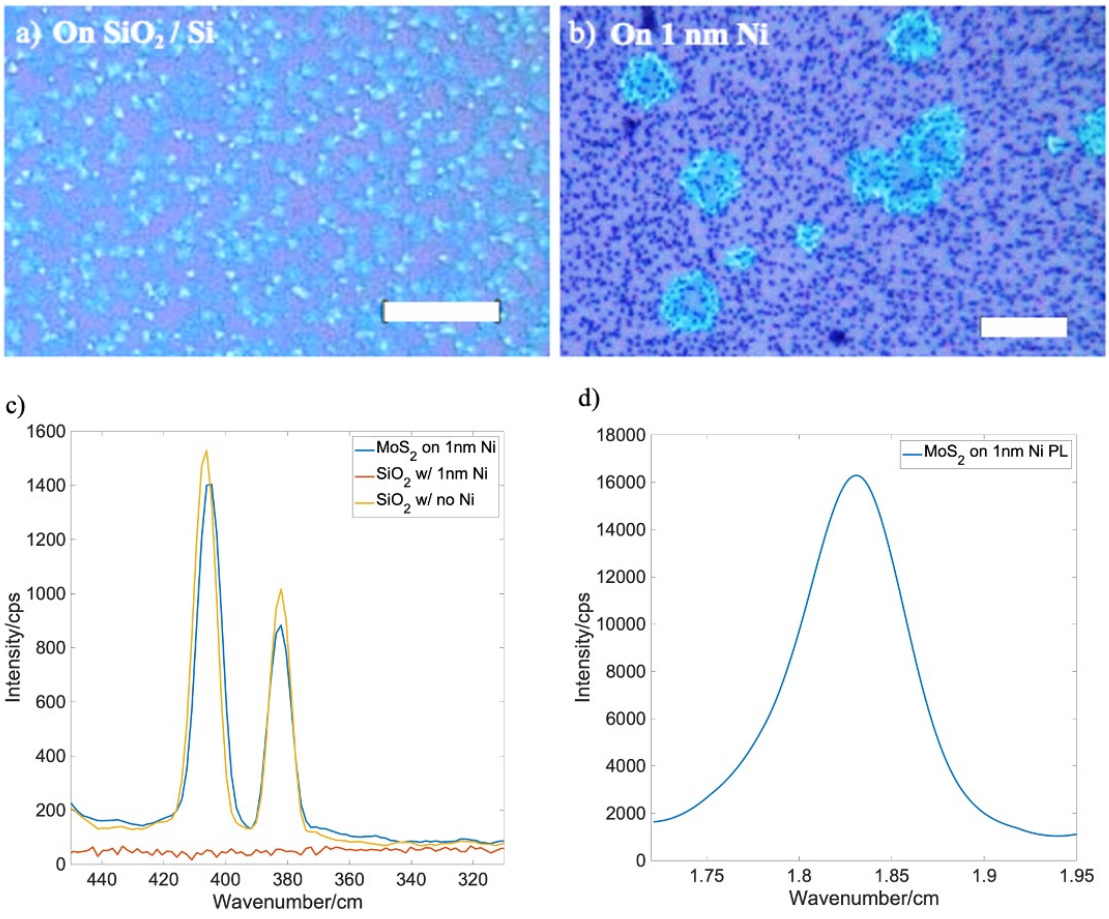

Figure 55 CVD grown MoS_2 on a) 300 nm SiO_2 on Si substrate and b) 1nm Ni evaporated onto SiO_2/Si substrates. Several small crystals of single crystalline, few-layer MoS_2 are visible on the SiO_2/Si substrates while a few, larger

crystalline MoS_2 domains with an altered morphology are obvious on the substrates with 1 nm Ni present. The black dots throughout the surface likely correspond to the NiS_x phase that forms during the sulfidation. Scale bar is 20 µm in length.

When a similar CVD growth process is employed with a 20 nm Au thin film deposited onto SiO_2/Si substrates, the resulting growth is significantly different. No MoS_2 crystals are seen on the 20 nm Au layer (Figure 56a) while several small triangles of MoS_2 can be seen on the SiO_2/Si substrate. It is interesting to note that the Au – SiO_2 interface features a continuous MoS_2 layer. It is possible that the Au layer seeds grow by reducing the nucleation barrier for the MoS_2 crystals, but Mo and S atoms prefer to diffuse and laterally grow over the SiO_2/Si substrate. This could be due to slower diffusion of S atoms into the Au film compared to lateral surface diffusion, or due to lowered surface energy after the dangling bonds on the Au layer are saturated with S atoms.

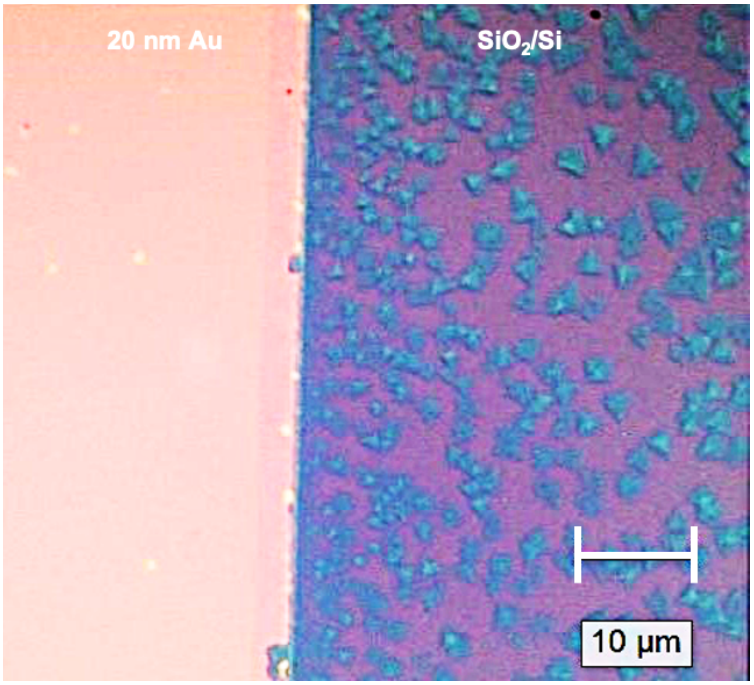

Figure 56 CVD grown MoS_2 on 20 nm Au deposited onto a SiO_2/Si substrate. The image shows the interface of Au/SiO_2 with the Au film on the left and the substrate on the right. MoS_2 triangles are evident on the substrate but no MoS_2 grows on the Au. The interface has a continuous layer of MoS_2 suggesting that Au allows for a lower barrier to nucleation but MoS_2 prefers to grow on the SiO_2/Si substrate.

From the results so far, it is clear that MoS_2 prefers to grow on SiO_2 compared to Au and that Ni alters the crystallization mechanism of MoS_2 during growth. However, it is important to investigate the effects of both Au and Ni together on the same sample when exposed to similar concentrations of S and MoO_3 to understand the nature of selectivity during growth. For this purpose, another array of circular 20 nm Au and 2 nm Ni patterns was deposited onto SiO_2/Si substrates using optical lithography. Figure 57 shows the magnified view of two such circles separated by the SiO_2/Si. This configuration allows us to investigate the influence of the Ni, Au, SiO_2, and Ni-SiO_2, Au-SiO_2 interfaces on MoS_2 growth, all at once. In this case, under careful control of the MoO_3 and S vapor pressures, selective growth of crystalline MoS_2 can be caused to occur only onto the patterned Ni regions. Several small domains can be seen over the Ni thin film possibly because of multiple layers of MoS_2 nucleating and growing over the Ni film. The Raman spectra obtained across the different rectangular regions (highlighted in Figure 57a) are shown in Figure 57b. MoS_2 peaks can be seen only for the Ni circle but not for the Au circle or the SiO_2/Si substrate.

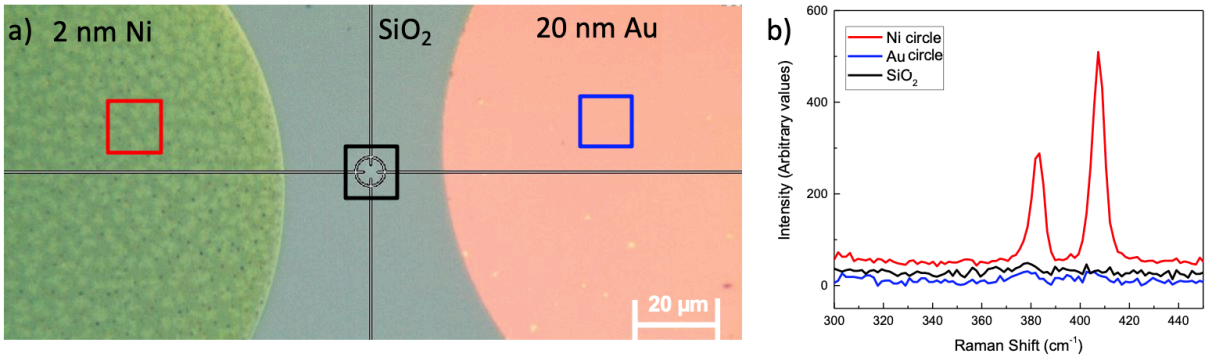

Figure 57 CVD grown MoS_2 on a patterned circular array of 2 nm Ni and 20 nm Au deposited onto a SiO_2/Si substratea) Magnified image of two such circles featuring 2 nm Ni (green) and 20 nm Au (pink) circles separated by the substrate. b) Raman spectra obtained across the different regions highlighted by the rectangles in a) – Ni circle (red), Au circle (blue), and SiO_2 (black).

It is important to note that only in a specific range of MoO_3 and S vapor phase concentration could this selectivity be observed, which manifested as differing growth behavior at different regions of the substrate. When lower concentrations of the precursors (Zone I) were utilized, there was only enough MoS_2 to nucleate and saturate all surface sites on the Ni film. At higher precursor concentrations (Zone III), it was favorable for the incoming MoS_2 atoms to saturate all surface sites available than to form thicker islands on the Ni film. Hence, crystalline MoS_2 was observed on the Au, Ni as well as SiO_2/Si substrate in this region. Finally, in the intermediate concentration region (Zone II), MoS_2 preferred to nucleate and grow on the Ni regions, followed by Au regions. This concentration dependence of selectivity is shown in Figure 58, and the subsequent discussion is focused on observations from the low concentration region, or the region with high growth selectivity. The substrate in Figure 58 represents patterned Ni channels and Au contacts for a back-gated transistors architecture, as discussed in the next section.

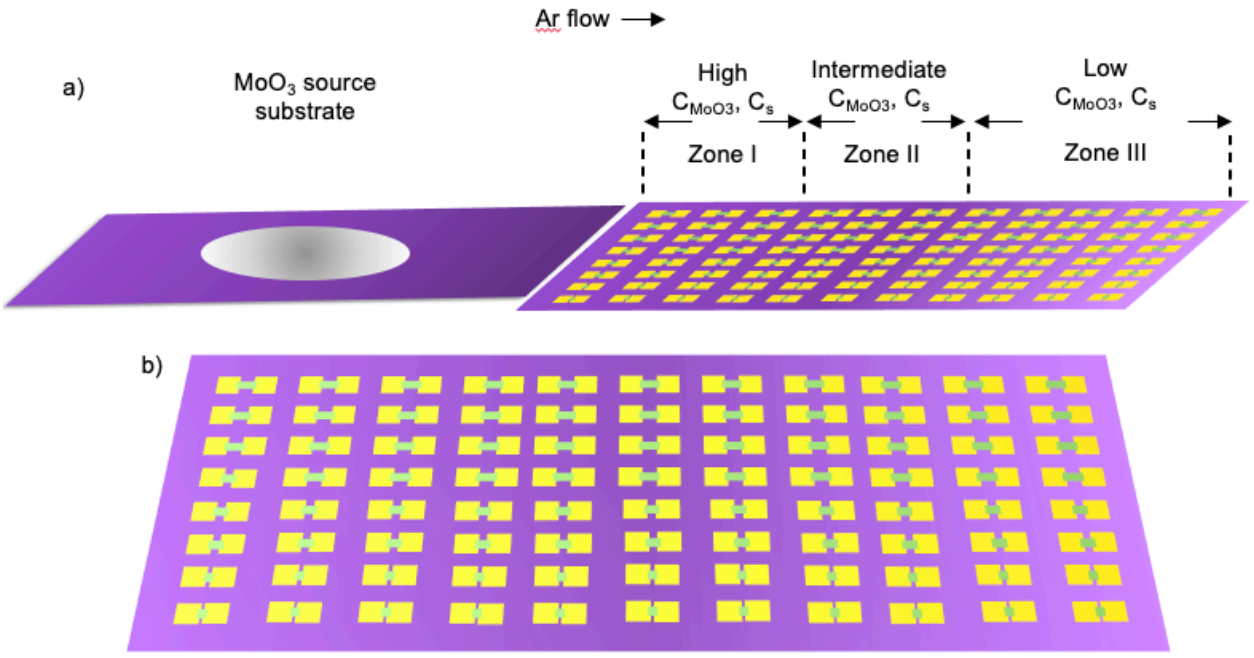

Figure 58 Illustration showing variation in precursor concentration of the patterned substrate during CVD. MoO_3 powder is spread onto a 300 nm SiO_2/Si wafer (source substrate) and the patterned substrate is placed next to it. The lateral distance from the MoO_3 substrate controls the precursor concentration variation. Closer to the source, C_{MoO3}

and C_s are higher, while they are lower away from it. b) Plan view of the patterned Au (yellow) and Ni (green) thin films with varying channel lengths normal to the direction of Ar flow. The drawings are not to scale and have been enlarged to illustrate details.

5.3 Bottom-up Fabrication of MoS_2 Film on Patterned Ni-Au Layers

The control samples show that selective growth of crystalline MoS_2 over the Ni region is possible in Zone III, when Ni and Au regions are not overlapping. The next logical goal was to determine if this selectivity was still valid when the Ni and Au thin film were deposited on the same sample in the configuration of a back-gated transistor. In this study, photolithographically patterned 100×100 μm^2 Au contacts were fabricated over Ni channels with varying widths (5 μm, 10 μm, and 20 μm). An interface of 10 μm between the channel and contacts was intentionally added to allow for greater chemical bonding and hence lower interfacial resistance to electron injection, as discussed in Section 3.

Figure 59a shows an optical image of one such pre-patterned SiO_2/Si substrate after MoS_2 was grown on it using CVD. This sample had 2 nm Au contacts and 2 nm Ni regions over the channel. This deposited structure is in the Zone I region of the growth configuration, with a medium vapor phase concentration of Mo and S precursors. Yet, it is clear from the Raman spectra (Figure 59b) that MoS_2 only grows on the Ni region. Similarly, in Zone III, crystalline and relatively weak MoS_2 peaks are obtained only over the Ni channel (Figure 59c-d). It is important to note that only 2 nm Au was deposited onto the contacts in this case, unlike the 20 nm Au film in Figure 56-57. This was done to limit the formation of Au-Ni-S complexes, as discussed later in this section.

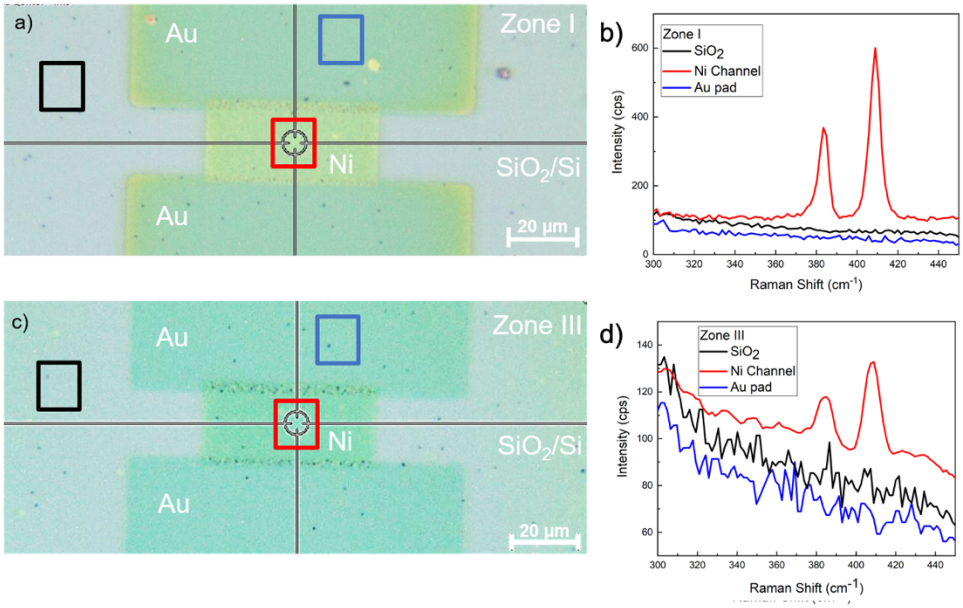

Figure 59 Selective growth of MoS_2 on a pre-patterned Ni channel and Au contacts a) CVD grown MoS_2 in the Zone I region over a Ni channel contacted by Au pads. The highlighted rectangles show the regions from which b) Raman spectra were acquired. Crystalline MoS_2 is present only over the Ni channel. c) CVD grown MoS_2 in Zone III on the same substrate, and d) Raman spectra obtained from the different regions in c.

To understand the variation in concentration of the MoS_2 precursors across the different zones, Raman spectra were obtained from a fixed row along the array of Ni-Au pattern but with concentrations in Zone I, II, and III range respectively. The results are shown in Figure 60. In Zone I, a thick MoS_2 film can be seen with a strong yellow contrast across the channel (Figure 60a). In Zone II, the contrast is weaker implying lesser intensity of MoS_2, as is expected due to decreased precursor concentration in this region (Figure 60b). Finally, in Zone III, a thinner MoS_2 film can be seen over the channel with a weak contrast (Figure 60c). For each case, the Raman spectra confirm the presence of crystalline MoS_2, even in the ultra-thin Zone III region (Figure 60d). The intensity of the MoS_2 peak progressively decreases across the regions, as expected. It is important to comment on the black dots observed only in the region where the Au is interfaced with the Ni film. They could be due to the formation of Au-Ni-S complexes, but further XPS mapping over this region would be needed to confirm the nature of this phase.

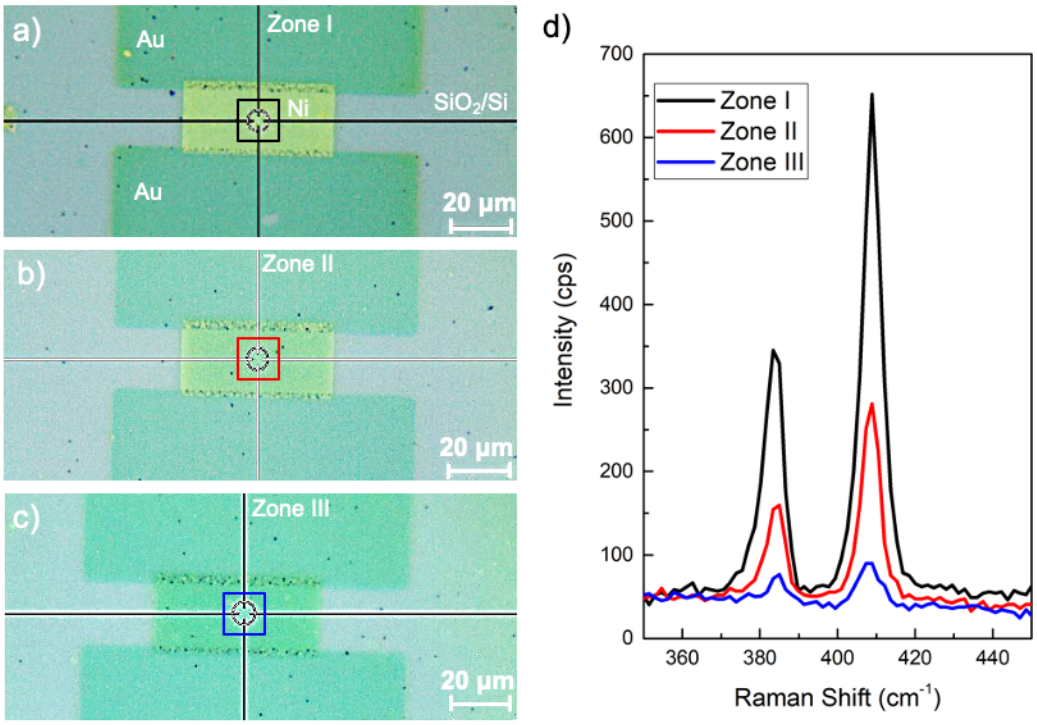

Figure 60 CVD grown MoS_2 across different zones and precursor concentrations. a) Zone I b) Zone II and c) Zone III regions over the pre-patterned substrate with 2 nm Ni and 2 nm Au pads. d) Raman spectra obtained from the highlighted rectangles in each of the Ni regions.

To highlight this selectivity of MoS_2 growth, a high-resolution Raman map was captured across the patterned films using the sample from Zone III. The map is placed over the optical image from this patterned sample in Figure 61. Crystalline MoS_2 is present only over the Ni channel, not over the Au or the SiO_2 regions. The higher intensity in some regions could be due to multiple layers of MoS_2 nucleating over these regions. PL spectra obtained from this region showed no significant peaks, but it is not clear whether that is due to Ni species quenching the PL response or if it is due to the presence of polycrystalline, few-layered MoS_2.

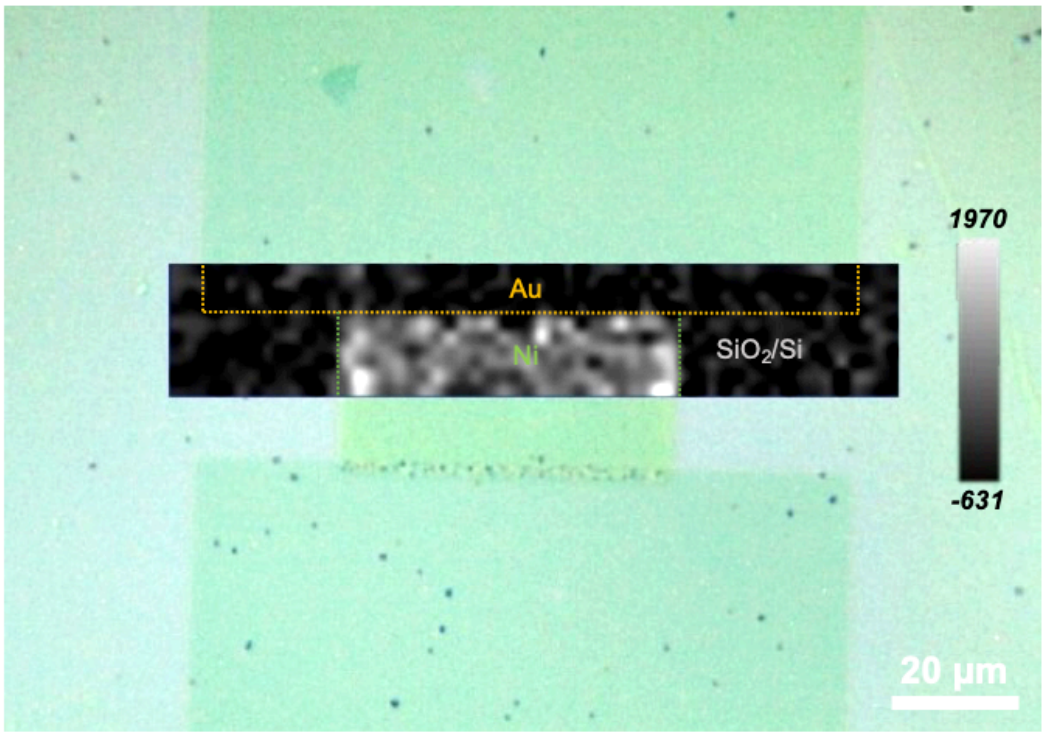

Figure 61 Raman intensity mapping of a region across the Au-Ni-SiO_2 interface with MoS_2 grown on patterned films in the Zone III region. Only the Ni region has predominantly crystalline MoS_2 implying successful selective growth of MoS_2 over the Ni channel.

Finally, it is important to highlight the significance of choosing the optimal Au-Ni interface width (the region where the Au and Ni films overlap) and Au layer thickness. When thicker Au (20 nm) contacts were interfaced with 2 nm Ni but over a wider length (10 µm), the selectivity was lost and MoS_2 appeared to nucleate only over the Au contacts (Figure 62). A distinctly transformed zone (black rectangle) forms in the region next to the Au-Ni interface region, possibly due to phase transformations at the Au-Ni interface. The Raman spectrum (Figure 62b) from this region shows an intense Raman peak indicating a stronger affinity of the incoming MoS_2 species for this transformed region. Further chemical analysis is required to understand the chemical nature, and the role that the underlying phase plays in controlling the nucleation of MoS_2 crystallites. The red rectangle in Figure 62a highlights the region where Ni and Au contacts overlap, and the Raman spectra (Figure 62b) obtained from this region shows a relatively weak

MoS_2 peak compared to the transformed zone. Finally, no crystalline MoS_2 is observed over the Ni channel indicating that the selectivity of the Ni channel is completely lost on changing the interface width (blue rectangle, Figure 62a-b). It could be possible that the incoming Mo and S atoms prefer to nucleate over the Au-Ni interface and transformed regions due to significantly altered surface energies. Additionally, this pattern is obtained from the Zone III region where the Mo-S precursor concentration may not be high enough to saturate the surface of the Ni thin film after it has nucleated on the Au-Ni-transformed regions. Figure 62c shows that these characteristics of the transformed Au-Ni regions are obtained over larger areas in Zone III as well.

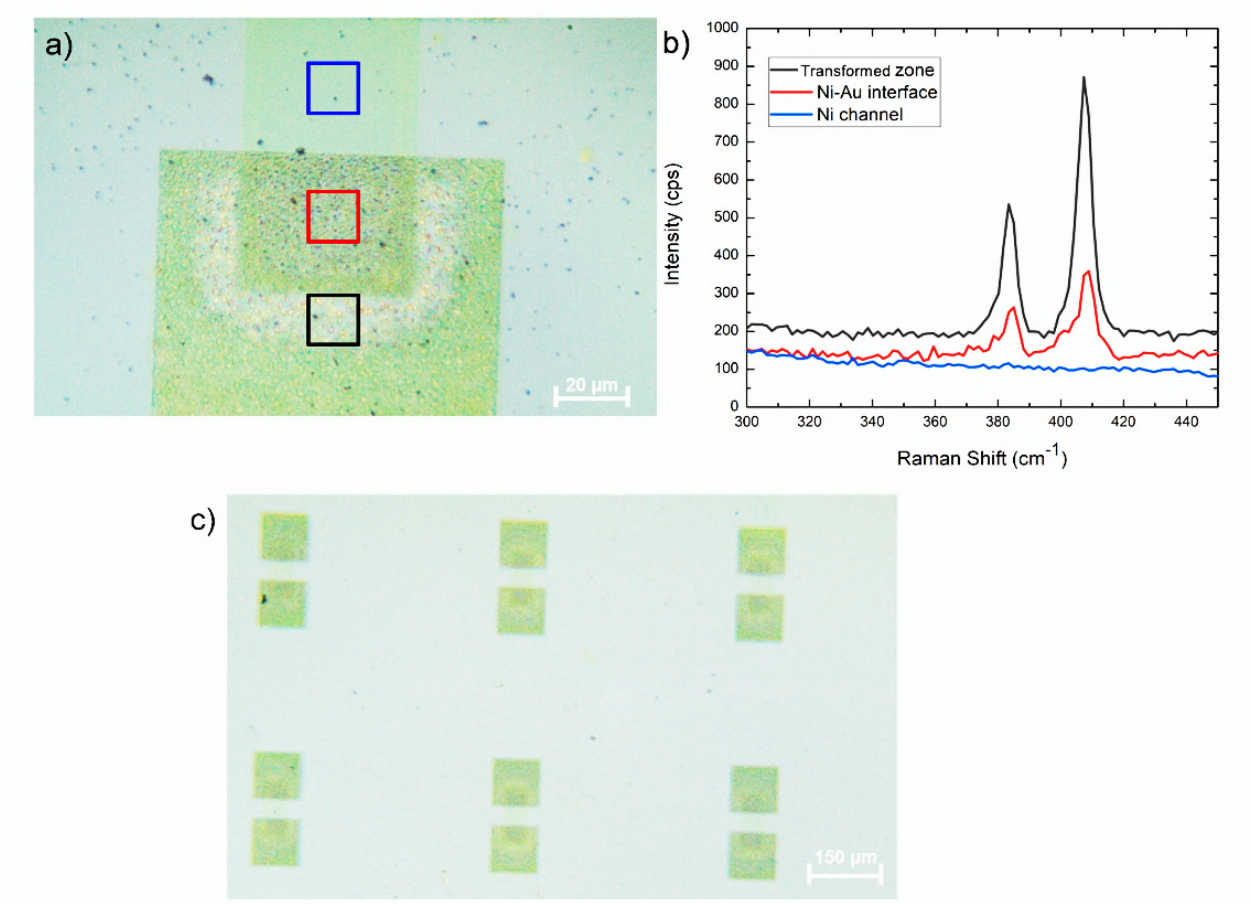

Figure 62 Effect of increasing Au-Ni overlap width in altering MoS_2 growth. a) Optical images from a pre-patterned region in Zone III. The rectangles highlight the chemically different regions – Ni channel, Ni-Au interface region, and Au transformed region. b) Raman spectra obtained from these regions show that crystalline MoS_2 is present only over the Ni-Au and the transformed regions but not over the Ni channel. c) Low magnification image of Ni-Au patterns across a larger area in Zone III, phase transformations are visible across all the patterns.

Based on the equilibrium Au-Ni phase diagram (Figure 63), it is possible that in the Au-Ni interface region, a phase transformation could be resulting in the formation of different Au-Ni phases. The highest temperature during the CVD process was 700 ºC. For the patterned substrates shown in Figure 62, 2 nm Au and 2 nm Ni were used. Ideally, the concentration of Au and Ni atoms in the interface region should correspond to ~ 50 at. % region in the phase diagram. The transformation at this temperature could correspond to a phase segregation (orange circles in Figure 63) resulting in Ni-rich and Au-rich phases over the interface region at 700 ºC which then further transform to form Au-Ni-S complexes on reaction with S. This hypothesis assumes that a reaction between the Au-Ni-S does not take place earlier because the S vapor is controlled to release when the furnace is at 700 ºC. However, near the edges of this region, the concentration of Au is significantly higher, relative to Ni. This region corresponds to the shaded area on the right side of this phase diagram. On cooling to room temperature, this region likely forms pure Au and pure Ni phases. The transformed zone (in Figure 62) features large Au particles that likely grew in size due to diffusion and coalescence of Au atoms from the region surrounding it. Hence it is referred to as the depleted zone. Again, further analysis using XPS would be needed to understand the chemical nature of the transformations involved, but it is clear that the chemical nature of the surface and the selectivity for MoS_2 growth are significantly affected by the presence of different metallic phases.

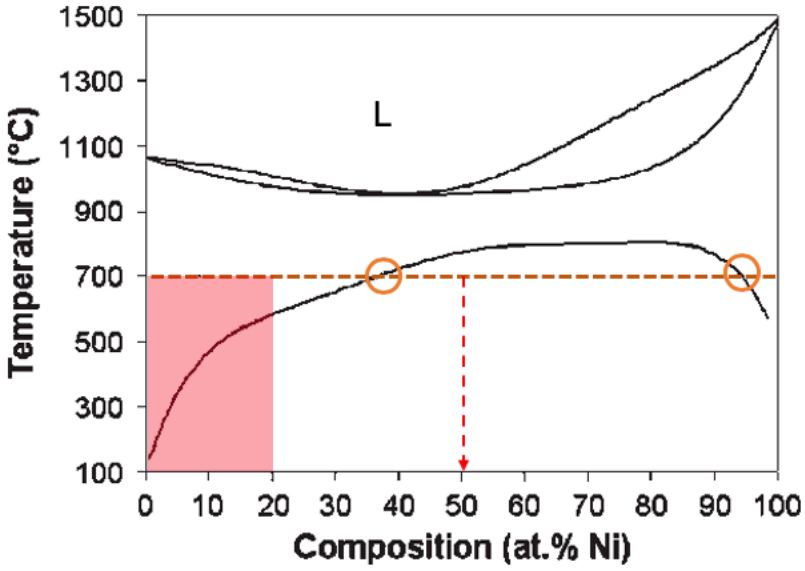

Figure 63 Binary phase diagram for Au-Ni. Adapted from reference [128].

5.4 Understanding the Au-Ni-MoS_2 Interface via AFM

To further understand the morphology of MoS_2 crystals across the Ni channel, an AFM map of the Ni-SiO_2 interface was obtained across the three regions. Figure 64 shows the presence of several small crystallites, possibly of MoS_2. The RMS surface roughness over the Ni channel is 8.5 nm (Zone I), 6.2 nm (Zone II), and 11.1 nm (Zone III). The step heights were obtained as a line scan across the Ni-SiO_2 interface and are shown as insets in the figures – 38.3 nm (Zone I), 23.3 nm (Zone II), and 19.4 nm (Zone III). Some MoS_2 crystallites (< 100 nm) can be observed over the SiO_2 region in Zone I and Zone II, but significantly smaller specks are observed in Zone III, confirming the greater selectivity of growth in this region. It also highlights the increasing layer thickness of MoS_2 over the Ni region going from Zone III to I as expected due to increasing precursor concentration. Note that the data shows the presence of a non-uniform, polycrystalline MoS_2 layer. Further analysis is required to confirm if a continuous film of MoS_2 lies underneath these crystallites but is not accessible by the AFM tip (the tip radius is 8 nm in this study).

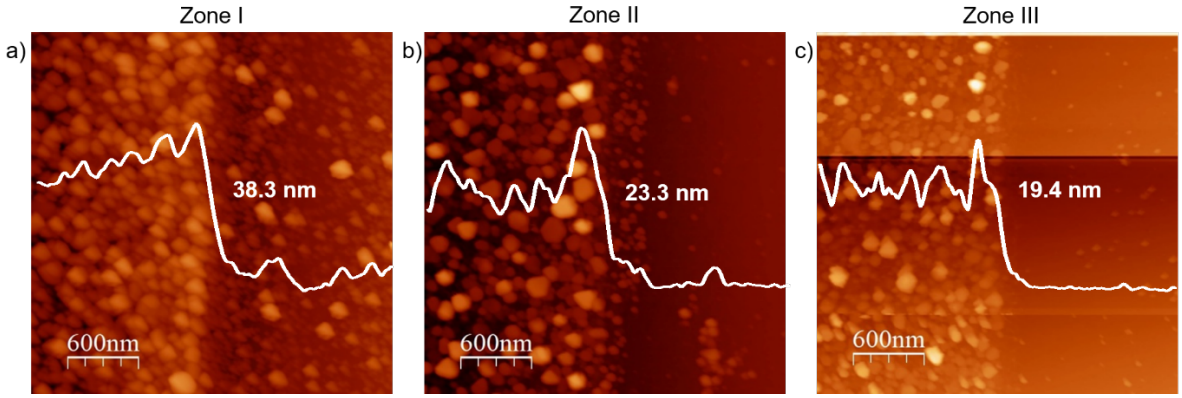

Figure 64 AFM images of the Ni (left) - SiO_2 (right) interface a) Several small crystallites are visible across the Ni channels as well some on the SiO_2 in Zone I. b) The selectivity considerably improves with fewer and more dispersed MoS_2 crystallites forming over the Ni channel, and practically none on the SiO_2 region in Zone II. c) The crystallites are smaller and more selectively grown in the Ni region in Zone III.

5.5 Engineering Growth of MoS_2 on Ni-Graphene Substrates

Graphene has been used as a growth substrate to enable van der Waals epitaxial (vdWE) growth of MoS_2.[163] vdWE allows for growth of crystalline overlayers without the lattice matching constraints or strain-induced defects that conventional epitaxy requires.[164–166] vdWE has also been shown to lower the temperature of crystalline growth (400 ºC) for MoS_2 crystals grown on graphene layers.[128] Similarly, formation of liquid NiS_x islands via van der Waals rheotaxy (vdWR) has shown to result in larger MoS_2 as previously discussed in Section 4.8.[111,167]

In this work, the nucleation of TMDC crystals on a thin film of Ni/graphene was investigated. A monolayer graphene film was transferred using conventional PMMA transfer process from a graphene/Cu foil to a SiO_2/Si substrate, following which 1 nm Ni thin film was evaporated on the graphene film. MoS_2 crystallites were grown via CVD on Ni/graphene substrates to understand the effects of combining vdWE and vdWR in templating and controlling the growth

kinetics of MoS_2 crystals. In particular, the ability of graphene to template crystals as the Ni atoms allowed for greater interface mobility during growth was investigated.

Figure 65a shows the growth of MoS_2 on transferred monolayer graphene on a SiO_2/Si substrate. Because of the PMMA based transfer process, some wrinkles and polymer residues could be introduced, highlighted by the red arrows. MoS_2 prefers to nucleate on these energetically active edge sites of graphene and has been demonstrated in previous studies as well.[163,168] However, a film of MoS_2 is still present across the relatively flat regions of graphene. The higher intensity of the Raman peaks of MoS_2 obtained from the surface steps compared to the flat regions confirms the preferential nucleation of crystalline MoS_2, resulting in the formation of the crossed pattern that is seen across the sample (Figure 65c).

On the other hand, the preferential nucleation of MoS_2 on the wrinkled graphene is completely absent when a 2 nm Ni film is added between the two. Figure 65b shows the optical image obtained from a MoS_2/Ni/graphene sample. A more conformal film (light blue contrast) is observed through the sample despite the obvious presence of wrinkles and polymer residues in certain regions. The black dots likely correspond to NiS_x and are similar to the ones observed earlier during the patterned growth of MoS_2 on Ni films in Section 5.2. The Raman spectra (Figure 65c) obtained from this region shows a relatively weak peak, suggesting the presence of a thinner crystalline MoS_2 layer, while the broad PL peak suggests that the MoS_2 could be thicker than a monolayer and/or polycrystalline. It is thus clear that the addition of metal atoms is important not only to control the chemical nature of the surface but also the growth trajectories of epitaxial van der Waals heterostructures.

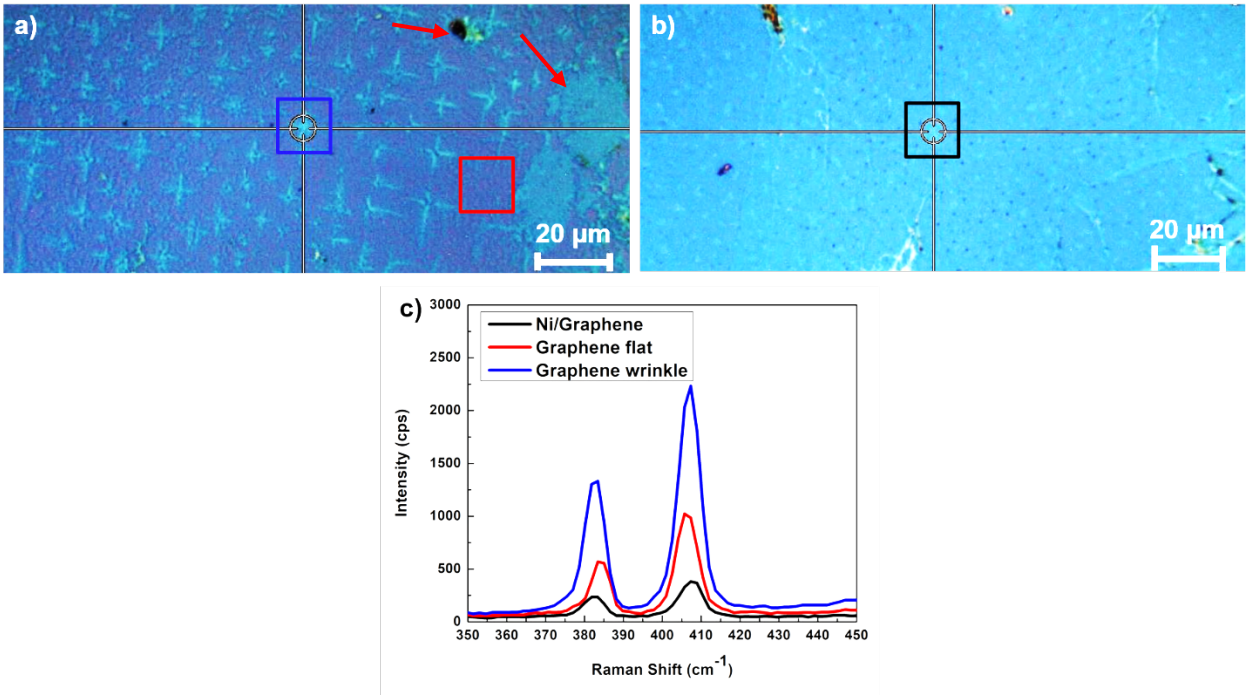

Figure 65 Effect of Ni/Graphene on MoS_2 growth via CVD. a) Optical image obtained from the MoS_2/Graphene sample. The transferred graphene features several wrinkles and regions with polymer residues. b) Optical image obtained from the MoS_2/Ni/graphene sample after growth. In the presence of Ni, preferential nucleation is no longer observed. c) Raman spectra obtained from different surface sites on the two samples. The MoS_2 film is thinner on the Ni due as indicated by the weaker Raman peak.

5.6 Conclusions and Implications for TMDC growth

This study enabled important insights into the role of surface chemistry and the nature of the substrate during the synthesis of crystalline MoS_2 films. Insight from our prior *in situ* TEM investigation of Ni-MoS_2 thin films in Chapter 4 enabled selective growth of MoS_2 crystals over Ni thin films. Ni films alter the surface affinity for Mo and S atoms during CVD growth, allowing for selective growth of MoS_2 crystals. In contrast, Au atoms only seeded MoS_2 growth, and once MoS_2 crystals seeded from the edges of Au thin film, they preferred to grow laterally over the surrounding SiO_2 substrate. These findings were combined to demonstrate the bottom-up fabrication of a back-gated transistor architecture with Au films as the contacts and Ni films over the channel. Under optimal conditions, crystalline MoS_2 could be caused to grow only over the Ni channel without growing on the Au contacts or the SiO_2/Si substrate. This bottom-up approach

could open pathways for more direct fabrication of MoS_2 transistors with no intermediate photolithography steps required after MoS_2 growth, reducing the contamination from photoresist residues across the metal-MoS_2 interface. Finally, this study also demonstrated the role of Ni atoms in allowing for epitaxial growth of large-area MoS_2 films templated with graphene underneath. Future work is needed to precisely control the layer thickness and morphology of single-crystalline MoS_2 over patterned substrates. The role of Ni and other metal atoms in influencing the electronic properties of such patterned transistor architectures also needs to be explored.

CHAPTER 6. Conclusions and Future Outlook

Today, a vast array of TMDCs exist, and the number of layered materials only keeps growing with the discovery of other binary and ternary chalcogenides. Yet, very little is understood of the phase transformations during the growth of these materials, as well as during the operation of devices fabricated with them. This Ph.D. dissertation has aimed to improve our understanding of the structural and chemical transformations in MoS_2 upon interfacing with a variety of materials. Using powerful insights from *in situ* characterization techniques like XPS, TEM, Raman spectroscopy, and XRD, this work has highlighted the importance of understanding these interfacial reactions in greater detail to allow for better design of a range of MoS_2 applications, from energy storage to optoelectronic devices.

As was seen in the *in situ* XPS study, contacting different crystallographic sites of the MoS_2 crystal can result in different chemical transformations, depending on the nature of the material interfaced. The surface oxide on edge planes passivates them in some cases, and the thermodynamically predicted reactions may not even occur. This work demonstrated the importance of performing *in situ* experiments to investigate phase transformations that take place upon interfacing the desired contact metals with underlying TMDCs before making a device. It was also observed that the addition of reactive metal species can significantly alter the growth pathways of MoS_2 crystals, leading to larger resulting crystals. This knowledge was then used to selectively fabricate crystalline MoS_2 on pre-patterned Ni films while inhibiting growth on Au contacts or the SiO_2/Si substrate. This work highlights the role of following a bottom-up approach to materials development, where the growth dynamics were engineered to control the final morphology of the nanostructure. Future work should be dedicated to exploring the role of different metals on the optoelectronic properties of these selectively patterned transistor structures.

Based on the findings in this dissertation, there are a few promising areas to pursue in the future. One exciting area to explore further could be low-temperature synthesis of 2D materials enabled by liquid-phase epitaxy. In Section 5.5, we reported that a combination of van der Waals epitaxy and liquid-phase epitaxy or rheotaxy could enable the wafer-scale growth of few-layered MoS_2 on Ni/graphene substrates. While this work and previous studies[163,168] have shown that small (~10 μm) single-crystalline domains of MoS_2 can nucleate preferably on graphene surface steps, deposition of a Ni layer on the graphene substrates allowed for wafer-scale growth of MoS_2 (the size was limited to ~1 cm^2 due to the dimensions of the transferred graphene). A detailed investigation of the role of different crystalline substrates (Si, Ge, GaAs, etc.) in templating the overlayers and reducing the crystallization temperature could be performed via *in situ* TEM. This approach could address problems of integrating TMDCs in the regular semiconducting fabrication process steps because of temperature or environmental limitations, in turn lowering the cost or retooling requirements for commercial applications.

Another exciting area would be to use dopant atoms to bond with the active edge sites of these TMDC crystals so as to stabilize them under ambient conditions. Currently, the crystals tend to degrade via physisorption of O atoms starting at S vacancies or etch pits when stored outside of protective conditions.[163,168] However, as the *in situ* XPS studies in Chapter 3 showed, certain metal atoms (like Ni) can react with chemically-active edge sites before they are passivated in the presence of ambient oxygen. Thus, *in situ* deposition of metal atoms while the vertically aligned MoS_2 film is being synthesized could open new pathways for stabilizing this material, as well as modulating properties. This could open possibilities of stabilizing other useful TMDCs like TiS_2, which degrades to TiO_2 under ambient conditions.[169] Additionally, an atomic resolution *in situ* STEM study of metal-doped TMDC systems during heating or biasing could yield important

insight into the kinetic pathways of phase transformations and metal atom diffusion. Understanding these pathways could allow engineering of metal-decorated edges of TMDC crystals, which may be considerably larger than conventional TMDC crystals formed with hydrothermal methods.[144-145] Overall, significant progress can be made in the future with a greater focus on understanding transformation pathways in metal-TMDC systems *in situ*, and then using the knowledge to engineer these nanostructures.

References

(1) Chhowalla, M.; Shin, H. S.; Eda, G.; Li, L. J.; Loh, K. P.; Zhang, H. The Chemistry of Two-Dimensional Layered Transition Metal Dichalcogenide Nanosheets. *Nature Chem.* **2013**, 5 (4), 263–275. https://doi.org/10.1038/nchem.1589.

(2) Novoselov, K. S.; Jiang, D.; Schedin, F.; Booth, T. J.; Khotkevich, V. V.; Morozov, S. V.; Geim, A. K. Two-Dimensional Atomic Crystals. *Proc. Natl. Acad. Sci. U. S. A.* **2005**, *102* (30), 10451–10453. https://doi.org/10.1073/pnas.0502848102.

(3) Radisavljevic, B.; Radenovic, A.; Brivio, J.; Giacometti, V.; Kis, A. Single-Layer MoS_2 Transistors. *Nat. Nanotechnol.* **2011**, *6* (3), 147–150. https://doi.org/10.1038/nnano.2010.279.

(4) Wilson, J. A.; Yoffe, A. D. The Transition Metal Dichalcogenides Discussion and Interpretation of the Observed Optical, Electrical and Structural Properties. *Adv. Phys.* **1969**, *18* (73), 193–335. https://doi.org/10.1080/00018736900101307.

(5) Joensen, P.; Frindt, R. F.; Morrison, S. R. Single-Layer MoS_2. *Mater. Res. Bull.* **1986**, *21* (4), 457–461. https://doi.org/10.1016/0025-5408(86)90011-5.

(6) Frindt, R. F. Single Crystals of MoS_2 Several Molecular Layers Thick. *J. Appl. Phys.* **1966**, *37* (4), 1928–1929. https://doi.org/10.1063/1.1708627.

(7) Manzeli, S.; Ovchinnikov, D.; Pasquier, D.; Yazyev, O. V.; Kis, A. 2D Transition Metal Dichalcogenides. *Nature Rev. Mater.* **2017**; *2* (8), 1–15. https://doi.org/10.1038/natrevmats.

(8) Hu, T.; Li, R.; Dong, J. A New (2 × 1) Dimerized Structure of Monolayer 1T-Molybdenum Disulfide, Studied from First Principles Calculations. *J. Chem. Phys.* **2013**, *139* (17), 174702. https://doi.org/10.1063/1.4827082.

(9) Mak, K. F.; Lee, C.; Hone, J.; Shan, J.; Heinz, T. F. Atomically Thin MoS_2 : A New Direct-Gap Semiconductor. *Phys. Rev. Lett.* **2010,** *105* (13), 136805. https://doi.org/10.1103/PhysRevLett.105.136805.

(10) Schulman, D. S.; Arnold, A. J.; Das, S. Contact Engineering for 2D Materials and Devices. *Chem. Soc. Rev.* **2018**, *47* (9), 3037–3058. https://doi.org/10.1039/c7cs00828g.

(11) Guo, Y.; Robertson, J. Band Engineering in Transition Metal Dichalcogenides: Stacked versus Lateral Heterostructures. *Appl. Phys. Lett.* **2016**, 108 (23), 233104. https://doi.org/10.1063/1.4953169.

(12) Gusakova, J.; Wang, X.; Shiau, L. L.; Krivosheeva, A.; Shaposhnikov, V.; Borisenko, V.; Gusakov, V.; Tay, B. K. Electronic Properties of Bulk and Monolayer TMDs: Theoretical Study Within DFT Framework (GVJ-2e Method). *Phys. Status Solidi Appl. Mater. Sci.* **2017**, *214* (12), 1700218. https://doi.org/10.1002/pssa.201700218.

(13) Han, Melinda Y., et al. Energy band-gap engineering of graphene nanoribbons. *Phys. Rev. Lett.* **2007**, 98 (20) 206805. https://doi.org/10.1103/PhysRevLett.98.206805.

(14) Coletti, C.; Riedl, C.; Lee, D. S.; Krauss, B.; Patthey, L.; Von Klitzing, K.; Smet, J. H.; Starke, U. Charge Neutrality and Band-Gap Tuning of Epitaxial Graphene on SiC by Molecular Doping. *Phys. Rev. B - Condens. Matter Mater. Phys.* **2010**, *81* (23).

https://doi.org/10.1103/PhysRevB.81.235401.

(15) Banhart, F.; Kotakoski, J.; Krasheninnikov, A. V. Structural Defects in Graphene. *ACS Nano* **2011**, *5* (1), 26–41. https://doi.org/10.1021/nn102598m.

(16) Murphy, D. W.; Trumbore, F. A. Metal Chalcogenides as Reversible Electrodes in Nonaqueous Lithium Batteries. *J. Cryst. Growth* **1977**, *39* (1), 185–199. https://doi.org/10.1016/0022-0248(77)90165-8.

(17) Hodes, G. Painted, Polycrystalline Thin Film Photoelectrodes for Photoelectrochemical Solar Cells. *J. Electrochem. Soc.* **1980**, *127* (10), 2252. https://doi.org/10.1149/1.2129386.

(18) Kautek, W.; Gobrecht, J.; Gerischer, H. Applicability of Semiconducting Layered Materials for Electrochemical Solar Energy Conversion. *Berichte der Bunsengesellschaft/Physical Chem. Chem. Phys.* **1980**, *84* (10), 1034–1040. https://doi.org/10.1002/bbpc.19800841021.

(19) Tributsch, H. Solar Energy-Assisted Electrochemical Splitting of Water: Some Energetical, Kinetical and Catalytical Considerations Verified on MoS_2 Layer Crystal Surfaces. *Zeitschrift fur Naturforsch. - Sect. A J. Phys. Sci.* **1977**, *32* (9), 972–985. https://doi.org/10.1515/zna-1977-0911.

(20) Furimsky, E. Role of MoS_2 and WS_2 in Hydrodesulfurization. *Catal. Rev.* **1980**, *22* (3), 371–400. https://doi.org/10.1080/03602458008067538.

(21) Sarkar, D.; Liu, W.; Xie, X.; Anselmo, A. C.; Mitragotri, S.; Banerjee, K. MoS_2 Field-Effect Transistor for next-Generation Label-Free Biosensors. *ACS Nano* **2014**, *8* (4), 3992–4003. https://doi.org/10.1021/nn5009148.

(22) Fan, X.; Xu, P.; Zhou, D.; Sun, Y.; Li, Y. C.; Nguyen, M. A. T.; Terrones, M.; Mallouk, T. E. Fast and Efficient Preparation of Exfoliated 2H MoS_2 Nanosheets by Sonication-Assisted Lithium Intercalation and Infrared Laser-Induced 1T to 2H Phase Reversion. *Nano Lett.* **2015**, *15* (9), 5956–5960. https://doi.org/10.1021/acs.nanolett.5b02091.

(23) Tang, Q.; Jiang, D. E. Stabilization and Band-Gap Tuning of the 1T-MoS_2 Monolayer by Covalent Functionalization. *Chem. Mater.* **2015**, *27* (10), 3743–3748. https://doi.org/10.1021/acs.chemmater.5b00986.

(24) Splendiani, A.; Sun, L.; Zhang, Y.; Li, T.; Kim, J.; Chim, C. Y.; Galli, G.; Wang, F. Emerging Photoluminescence in Monolayer MoS_2. *Nano Lett.* **2010**, *10* (4), 1271–1275. https://doi.org/10.1021/nl903868w.

(25) Godefroo, S.; Hayne, M.; Jivanescu, M.; Stesmans, A.; Zacharias, M.; Lebedev, O. I.; Van Tendeloo, G.; Moshchalkov, V. V. Classification and Control of the Origin of Photoluminescence from Si Nanocrystals. *Nat. Nanotechnol.* **2008**, *3* (3), 174–178. https://doi.org/10.1038/nnano.2008.7.

(26) Nirmal, M.; Brus, L. Luminescence Photophysics in Semiconductor Nanocrystals. *Acc. of Chem. Res.* **1999**, 407–414. https://doi.org/10.1021/ar9700320.

(27) Kondekar, N. P.; Boebinger, M. G.; Woods, E. V.; McDowell, M. T. *In situ* XPS Investigation of Transformations at Crystallographically Oriented MoS_2 Interfaces. *ACS Appl. Mater. Interfaces* **2017**, *9* (37), 32394–32404. https://doi.org/10.1021/acsami.7b10230.

(28) Jaramillo, T. F.; Jørgensen, K. P.; Bonde, J.; Nielsen, J. H.; Horch, S.; Chorkendorff, I. Identification of Active Edge Sites for Electrochemical H2 Evolution from MoS_2 Nanocatalysts. *Science.* **2007**, *317* (5834), 100–102. https://doi.org/10.1126/science.1141483.

(29) Kong, D.; Wang, H.; Cha, J. J.; Pasta, M.; Koski, K. J.; Yao, J.; Cui, Y. Synthesis of MoS_2 and $MoSe_2$ Films with Vertically Aligned Layers. *Nano Lett.* **2013**, *13* (3), 1341–1347. https://doi.org/10.1021/nl400258t.

(30) Wang, H.; Lu, Z.; Xu, S.; Kong, D.; Cha, J. J.; Zheng, G.; Hsu, P. C.; Yan, K.; Bradshaw, D.; Prinz, F. B.; Cui, Y. Electrochemical Tuning of Vertically Aligned MoS_2 Nanofilms and Its Application in Improving Hydrogen Evolution Reaction. *Proc. Natl. Acad. Sci. U. S. A.* **2013**, *110* (49), 19701–19706. https://doi.org/10.1073/pnas.1316792110.

(31) Yang, J.; Wang, K.; Zhu, J.; Zhang, C.; Liu, T. Self-Templated Growth of Vertically Aligned 2H-1T MoS_2 for Efficient Electrocatalytic Hydrogen Evolution. *ACS Appl. Mater. Interfaces* **2016**, *8* (46), 31702–31708. https://doi.org/10.1021/acsami.6b11298.

(32) Wang, H.; Tsai, C.; Kong, D.; Chan, K.; Abild-Pedersen, F.; Nørskov, J. K.; Cui, Y. Transition-Metal Doped Edge Sites in Vertically Aligned MoS_2 Catalysts for Enhanced Hydrogen Evolution. *Nano Res.* **2015**, *8* (2), 566–575. https://doi.org/10.1007/s12274-014-0677-7.

(33) Allain, A.; Kang, J.; Banerjee, K.; Kis, A. Electrical Contacts to Two-Dimensional Semiconductors. *Nature Materials*. **2015**, 1195–1205. https://doi.org/10.1038/nmat4452.

(34) Komsa, H. P.; Kotakoski, J.; Kurasch, S.; Lehtinen, O.; Kaiser, U.; Krasheninnikov, A. V. Two-Dimensional Transition Metal Dichalcogenides under Electron Irradiation: Defect Production and Doping. *Phys. Rev. Lett.* **2012**, *109* (3), 035503. https://doi.org/10.1103/PhysRevLett.109.035503.

(35) Chen, Y.; Huang, S.; Ji, X.; Adepalli, K.; Yin, K.; Ling, X.; Wang, X.; Xue, J.; Dresselhaus, M.; Kong, J.; Yildiz, B. Tuning Electronic Structure of Single Layer MoS_2 through Defect and Interface Engineering. *ACS Nano* **2018**, *12* (3), 2569–2579. https://doi.org/10.1021/acsnano.7b08418.

(36) Song, S. H.; Joo, M. K.; Neumann, M.; Kim, H.; Lee, Y. H. Probing Defect Dynamics in Monolayer MoS_2 via Noise Nanospectroscopy. *Nat. Commun.* **2017**, *8* (1), 1–6. https://doi.org/10.1038/s41467-017-02297-3.

(37) McDonnell, S.; Addou, R.; Buie, C.; Wallace, R. M.; Hinkle, C. L. Defect-Dominated Doping and Contact Resistance in MoS_2. *ACS Nano* **2014**, *8* (3), 2880–2888. https://doi.org/10.1021/nn500044q.

(38) Han, S. W.; Hwang, Y. H.; Kim, S. H.; Yun, W. S.; Lee, J. D.; Park, M. G.; Ryu, S.; Park, J. S.; Yoo, D. H.; Yoon, S. P.; Hong, S. C.; Kim, K. S.; Park, Y. S. Controlling Ferromagnetic Easy Axis in a Layered MoS_2 Single Crystal. *Phys. Rev. Lett.* **2013**, *110* (24), 247201. https://doi.org/10.1103/PhysRevLett.110.247201.

(39) Kang, J.; Liu, W.; Sarkar, D.; Jena, D.; Banerjee, K. Computational Study of Metal Contacts to Monolayer Transition-Metal Dichalcogenide Semiconductors. *Phys. Rev. X*. **2014**, *4* (3), 031005. https://doi.org/10.1103/PhysRevX.4.031005.

(40) Zhou, W.; Zou, X.; Najmaei, S.; Liu, Z.; Shi, Y.; Kong, J.; Lou, J.; Ajayan, P. M.; Yakobson, B. I.; Idrobo, J. C. Intrinsic Structural Defects in Monolayer Molybdenum Disulfide. *Nano Lett.* **2013**, *13* (6), 2615–2622. https://doi.org/10.1021/nl4007479.

(41) Huang, M.; Li, S.; Zhang, Z.; Xiong, X.; Li, X.; Wu, Y. Multifunctional High-Performance van Der Waals Heterostructures. *Nat. Nanotechnol.* **2017**, *12* (12), 1148–1154. https://doi.org/10.1038/NNANO.2017.208.

(42) McCreary, K. M.; Hanbicki, A. T.; Robinson, J. T.; Cobas, E.; Culbertson, J. C.; Friedman, A. L.; Jernigan, G. G.; Jonker, B. T. Large-Area Synthesis of Continuous and Uniform MoS_2 Monolayer Films on Graphene. *Adv. Funct. Mater.* **2014**, *24* (41), 6449–6454. https://doi.org/10.1002/adfm.201401511.

(43) Wang, S.; Wang, X.; Warner, J. H. All Chemical Vapor Deposition Growth of MoS_2:H-BN Vertical van Der Waals Heterostructures. *ACS Nano* **2015**, *9* (5), 5246–5254. https://doi.org/10.1021/acsnano.5b00655.

(44) Shan, J.; Li, J.; Chu, X.; Xu, M.; Jin, F.; Fang, X.; Wei, Z.; Wang, X. Enhanced Photoresponse Characteristics of Transistors Using CVD-Grown MoS_2/WS_2 Heterostructures. *Appl. Surf. Sci.* **2018**, *443*, 31–38. https://doi.org/10.1016/j.apsusc.2018.02.244.

(45) Geim, A. K.; Grigorieva, I. V. Van Der Waals Heterostructures. *Nature*. **2013**, *499* (7459), 419–425. https://doi.org/10.1038/nature12385.

(46) Liu, X.; Balla, I.; Bergeron, H.; Hersam, M. C. Point Defects and Grain Boundaries in Rotationally Commensurate MoS_2 on Epitaxial Graphene. *J. Phys. Chem. C* **2016**, *120* (37), 20798–20805. https://doi.org/10.1021/acs.jpcc.6b02073.

(47) Britnell, L.; Ribeiro, R. M.; Eckmann, A.; Jalil, R.; Belle, B. D.; Mishchenko, A.; Kim, Y. J.; Gorbachev, R. V.; Georgiou, T.; Morozov, S. V.; Grigorenko, A. N.; Geim, A. K.; Casiraghi, C.; Castro Neto, A. H.; Novoselov, K. S. Strong Light-Matter Interactions in Heterostructures of Atomically Thin Films. *Science.* **2013**, *340* (6138), 1311–1314. https://doi.org/10.1126/science.1235547.

(48) Casa Software Ltd. The Nature of X-ray Photoelectron Spectra http://www.casaxps.com/help_manual/XPSInformation/IntroductiontoXPS.htm (accessed Apr 9, 2020).

(49) ThermoFisher. Thermo Scientific XPS: What is XPS https://xpssimplified.com/whatisxps.php (accessed Apr 7, 2020).

(50) Wenzel, S.; Randau, S.; Leichtweiß, T.; Weber, D. A.; Sann, J.; Zeier, W. G.; Janek, J. Direct Observation of the Interfacial Instability of the Fast Ionic Conductor $Li_{10}GeP_2S_{12}$ at the Lithium Metal Anode. *Chem. Mater.* **2016**, *28* (7), 2400–2407. https://doi.org/10.1021/acs.chemmater.6b00610.

(51) Leong, W. S.; Nai, C. T.; Thong, J. T. L. What Does Annealing Do to Metal-Graphene Contacts? *Nano Lett.* **2014**, *14* (7), 3840–3847. https://doi.org/10.1021/nl500999r.

(52) Lauf, R. J. Evaluation of Ceramic Insulators for Lithium Electrochemical Reduction Cells. *J. Electrochem. Soc.* **1992**, *139* (8), 2087. https://doi.org/10.1149/1.2221183.

(53) Wenzel, S.; Leichtweiss, T.; Krüger, D.; Sann, J.; Janek, J. Interphase Formation on Lithium

Solid Electrolytes - An *in situ* Approach to Study Interfacial Reactions by Photoelectron Spectroscopy. *Solid State Ionics* **2015**, *28* (7), 98–105. https://doi.org/10.1016/j.ssi.2015.06.001.

(54) NIST X-ray Photoelectron Spectroscopy (XPS) Database Main Search Menu https://srdata.nist.gov/xps/main_search_menu.aspx (accessed May 27, 2020).

(55) Antoni van Leeuwenhoek on the Circulation of the Blood. Latin Text of His 65th Letter to the Royal Society (Sept. 7th 1688). *Facsimile. J. Am. Med. Assoc.* **1963**, *184* (4), 322. https://doi.org/10.1001/jama.1963.03700170114042.

(56) Chung, K.-T.; Liu, J.-K. *Pioneers in Microbiology*; World Scientific, 2017. https://doi.org/10.1142/10288.

(57) DENSsolutions - *In situ* Microscopy Innovative Solutions https://denssolutions.com/ (accessed Apr 9, 2020).

(58) TEM Heating Platform for *in situ* TEM Analysis - Wildfire https://www.axt.com.au/products/in-situ-tem-heating-platform-wildfire/ (accessed Apr 7, 2020).

(59) Optical Lithography - an overview (pdf) | ScienceDirect Topics https://www.sciencedirect.com/topics/materials-science/optical-lithography/pdf (accessed Apr 10, 2020).

(60) Wang, L.; Meric, I.; Huang, P. Y.; Gao, Q.; Gao, Y.; Tran, H.; Taniguchi, T.; Watanabe, K.; Campos, L. M.; Muller, D. A.; Guo, J.; Kim, P.; Hone, J.; Shepard, K. L.; Dean, C. R. One-Dimensional Electrical Contact to a Two-Dimensional Material. *Science.* **2013**, *342* (6158), 614–617. https://doi.org/10.1126/science.1244358.

(61) McDonnell, S.; Smyth, C.; Hinkle, C. L.; Wallace, R. M. MoS_2-Titanium Contact Interface Reactions. *ACS Appl. Mater. Interfaces* **2016**, *8* (12), 8289–8294. https://doi.org/10.1021/acsami.6b00275.

(62) Smyth, C. M.; Addou, R.; McDonnell, S.; Hinkle, C. L.; Wallace, R. M. Contact Metal-MoS_2 Interfacial Reactions and Potential Implications on MoS_2-Based Device Performance. *J. Phys. Chem. C* **2016**, *120* (27), 14719–14729. https://doi.org/10.1021/acs.jpcc.6b04473.

(63) Kondekar, N. P.; Boebinger, M. G.; Woods, E. V.; McDowell, M. T. *In situ* XPS Investigation of Transformations at Crystallographically Oriented MoS_2 Interfaces. *ACS Appl. Mater. Interfaces* **2017**, *9* (37). https://doi.org/10.1021/acsami.7b10230.

(64) Baker, M. A.; Gilmore, R.; Lenardi, C.; Gissler, W. XPS Investigation of Preferential Sputtering of S from MoS_2 and Determination of MoSx Stoichiometry from Mo and S Peak Positions. *Appl. Surf. Sci.* **1999**, *150* (1), 255–262. https://doi.org/10.1016/S0169-4332(99)00253-6.

(65) McDonnell, S.; Addou, R.; Buie, C.; Wallace, R. M.; Hinkle, C. L. Defect-dominated doping and contact resistance in MoS_2. *ACS Nano* **2014**, *8* (3), 2880–2888. https://doi.org/10.1021/nn500044q.

(66) Voiry, D.; Salehi, M.; Silva, R.; Fujita, T.; Chen, M.; Asefa, T.; Shenoy, V. B.; Eda, G.; Chhowalla, M. Conducting MoS_2 Nanosheets as Catalysts for Hydrogen Evolution Reaction. *Nano Lett.* **2013**, *13* (12), 6222–6227. https://doi.org/10.1021/nl403661s.

(67) Wang, L.; Xu, Z.; Wang, W.; Bai, X. Atomic Mechanism of Dynamic Electrochemical Lithiation Processes of MoS_2 Nanosheets. *J. Am. Chem. Soc.* **2014**, *136* (18), 6693–6697. https://doi.org/10.1021/ja501686w.

(68) Son, Y.; Lee, J. S.; Son, Y.; Jang, J. H.; Cho, J. Recent Advances in Lithium Sulfide Cathode Materials and Their Use in Lithium Sulfur Batteries. *Adv. Energy Mater.* **2015**, *5* (16), 1–14. https://doi.org/10.1002/aenm.201500110.

(69) Papageorgopoulos, C. A.; Jaegermann, W. Li Intercalation across and along the van Der Waals Surfaces of MoS_2(0001). *Surf. Sci.* **1995**, *338* (1–3), 83–93. https://doi.org/10.1016/0039-6028(95)00544-7.

(70) Boebinger, M. G.; Xu, M.; Ma, X.; Chen, H.; Unocic, R. R.; McDowell, M. T. Distinct Nanoscale Reaction Pathways in a Sulfide Material for Sodium and Lithium Batteries. *J. Mater. Chem. A* **2017**, *5* (23), 11701–11709. https://doi.org/10.1039/c6ta09195d.

(71) Sacher, E. Asymmetries in Transition Metal XPS Spectra: Metal Nanoparticle Structure, and Interaction with the Graphene-Structured Substrate Surface. *Langmuir* **2010**, *26* (6), 3807–3814. https://doi.org/10.1021/la902678x.

(72) Hubbell, J. H.; Seltzer, S. M. NIST Standard Reference Database 126. https://doi.org/https://dx.doi.org/10.18434/T4D01F.

(73) Lide, D. Standard Thermodynamic Properties of Chemical Substances. *CRC Handb. Chem.* **2007**, *90* (4), 4–42.

(74) Allred, A. L. Electronegativity Values from Thermochemical Data. *J. Inorg. Nucl. Chem.* **1961**, *17* (3–4), 215–221. https://doi.org/10.1016/0022-1902(61)80142-5.

(75) Pankratz, L. B.; Mah, A. D.; Watson, S. W. Thermodynamic Properties of Sulfides. **1987**, 427.

(76) Addou, R.; Colombo, L.; Wallace, R. M. Surface Defects on Natural MoS_2. *ACS Appl. Mater. Interfaces* **2015**, *7* (22), 11921–11929. https://doi.org/10.1021/acsami.5b01778.

(77) Olesinki, R.; Abbaschian, G. J. The Ge− Mo (Germanium-Molybdenum) System. *J. Phase Equilibria* **1987**, *8* (1), 53–56.

(78) McGovern, I. T.; Dietz, E.; Rotermund, H. H.; Bradshaw, A. M.; Braun, W.; Radlik, W.; McGilp, J. F. Soft X-Ray Photoemission Spectroscopy of Metal-Molybdenum Bisulphide Interfaces. *Surf. Sci.* **1985**, *152–153* (PART 2), 1203–1212. https://doi.org/10.1016/0039-6028(85)90540-0.

(79) Baren, M. R. The Ag-Mo (Silver-Molybdenum) System Equilibrium Diagram. *Bulletin of Alloy Phase Diagrams*. **1990**, 11 (6), 548-549.

(80) Spevack, P. A.; McIntyre, N. S. A Raman and XPS Investigation of Supported Molybdenum Oxide Thin Films. 2. Reactions with Hydrogen Sulfide. *J. Phys. Chem.* **1993**, *97* (42), 11031–11036. https://doi.org/10.1021/j100144a021.

(81) Giannazzo, F.; Fisichella, G.; Piazza, A.; Di Franco, S.; Greco, G.; Agnello, S.; Roccaforte, F. Effect of Temperature–Bias Annealing on the Hysteresis and Subthreshold Behavior of Multilayer MoS_2 Transistors. *Phys. Status Solidi - Rapid Res. Lett.* **2016**, *10* (11), 797–801. https://doi.org/10.1002/pssr.201600209.

(82) Liu, W.; Kang, J.; Cao, W.; Sarkar, D.; Khatami, Y.; Jena, D.; Banerjee, K. High-Performance Few-Layer-MoS_2 Field-Effect-Transistor with Record Low Contact-Resistance. In *Technical Digest - International Electron Devices Meeting, IEDM*; **2013**. https://doi.org/10.1109/IEDM.2013.6724660.

(83) Toyama, M.; Ohashi, T.; Matsuura, K.; Shimizu, J.; Muneta, I.; Kakushima, K.; Tsutsui, K.; Wakabayashi, H. Ohmic Contact between Titanium and Sputtered MoS_2 Films Achieved by Forming-Gas Annealing. *Jpn. J. Appl. Phys.* **2018**, *57* (7), 07MA04. https://doi.org/10.7567/JJAP.57.07MA04.

(84) English, C. D.; Shine, G.; Dorgan, V. E.; Saraswat, K. C.; Pop, E. Improved Contacts to MoS_2 Transistors by Ultra-High Vacuum Metal Deposition. *Nano Lett.* **2016**, 16(6), 3824-3830. https://doi.org/10.1021/acs.nanolett.6b01309.

(85) Abraham, M.; Mohney, S. E. Annealed Ag Contacts to MoS_2 Field-Effect Transistors. *J. Appl. Phys.* **2017**, *122* (11), 115306. https://doi.org/10.1063/1.4991961.

(86) Lu, Q.; Fang, C.; Liu, Y.; Shao, Y.; Han, G.; Zhang, J.; Hao, Y. Temperature Dependence of Annealing on the Contact Resistance of MoS_2 with Graphene Electrodes Observed. In *Japanese Journal of Applied Physics*; *Japan Society of Applied Physics*, **2018**, 57, 04FP07. https://doi.org/10.7567/JJAP.57.04FP07.

(87) Chen, K. C.; Lai, S. M.; Wu, B. Y.; Chen, C.; Lin, S. Y. Van Der Waals Epitaxy of Large-Area and Single-Crystalline Gold Films on MoS_2 for Low-Contact-Resistance 2D-3D Interfaces. *ACS Appl. Mater. Interfaces* **2020**, *2020*, 2997–3003. https://doi.org/10.1021/acsanm.0c00262.

(88) Sun, M.; Nelson, A. E.; Adjaye, J. On the Incorporation of Nickel and Cobalt into MoS 2-Edge Structures. *J. Catal.* **2004**, *226* (1), 32–40. https://doi.org/10.1016/j.jcat.2004.05.005.

(89) Pratt, K. C.; Sanders, J. V.; Tamp, N. The Role of Nickel in the Activity of Unsupported Ni-Mo Hydrodesulfurization Catalysts. *J. Catal.* **1980**, *66* (1), 82–92. https://doi.org/10.1016/0021-9517(80)90010-X.

(90) Okamoto, H. Ni-S (Nickel-Sulfur). *J. Phase Equilibria Diffus.* **2009**, *30* (1), 123–123. https://doi.org/10.1007/s11669-008-9430-9.

(91) Regula, M.; Ballif, C.; Lévy, F. *In situ* TEM Observation of Nickel Promoted WS_2 Thin-Film Crystallization. *J. Cryst. Growth* **1998**, *193* (1–2), 109–113. https://doi.org/10.1016/S0022-0248(98)00501-6.

(92) Girleanu, M.; Alphazan, T.; Boudene, Z.; Bonduelle-Skrzypczak, A.; Legens, C.; Gay, A. S.; Copéret, C.; Ersen, O.; Raybaud, P. Magnifying the Morphology Change Induced by a Nickel Promoter in Tungsten(IV) Sulfide Industrial Hydrocracking Catalyst: A HAADF-STEM and DFT Study. *ChemCatChem* **2014**, *6* (6), 1594–1598. https://doi.org/10.1002/cctc.201402115.

(93) Sharifvaghefi, S.; Zheng, Y. Dispersed Ni and Co Promoted MoS_2 Catalysts with Magnetic Greigite as a Core: Performance and Stability in Hydrodesulfurization. *ChemistrySelect* **2017**, *2* (17), 4678–4685. https://doi.org/10.1002/slct.201700851.

(94) Lauritsen, J. V.; Kibsgaard, J.; Olesen, G. H.; Moses, P. G.; Hinnemann, B.; Helveg, S.; Nørskov, J. K.; Clausen, B. S.; Topsøe, H.; Lægsgaard, E.; Besenbacher, F. Location and

Coordination of Promoter Atoms in Co- and Ni-Promoted MoS_2-Based Hydrotreating Catalysts. *J. Catal.* **2007**, *249* (2), 220–233. https://doi.org/10.1016/j.jcat.2007.04.013.

(95) Topsøe, H.; Clausen, B. S.; Massoth, F. E. Hydrotreating Catalysis. *Catalysis*, **1996**, 1–269. https://doi.org/10.1007/978-3-642-61040-0_1.

(96) Sánchez-Delgado, R. A. Organometallic Modeling of the Hydrodesulfurization and Hydrodenitrogenation Reactions; 2002; Vol. 24. https://doi.org/10.1007/0-306-47619-3.

(97) Lukowski, M. A.; Daniel, A. S.; Meng, F.; Forticaux, A.; Li, L.; Jin, S. Enhanced Hydrogen Evolution Catalysis from Chemically Exfoliated Metallic MoS_2 Nanosheets. *J. Am. Chem. Soc.* **2013**, *135* (28), 10274–10277. https://doi.org/10.1021/ja404523s.

(98) Ding, Q.; Song, B.; Xu, P.; Jin, S. Efficient Electrocatalytic and Photoelectrochemical Hydrogen Generation Using MoS_2 and Related Compounds. *Chem*. Elsevier Inc November 10, 2016, pp 699–726. https://doi.org/10.1016/j.chempr.2016.10.007.

(99) Topsøe, N. Y.; Topsøe, H. Characterization of the Structures and Active Sites in Sulfided CoMo Al_2O_3 and NiMo Al_2O_3 Catalysts by NO Chemisorption. *J. Catal.* **1983**, *84* (2), 386–401. https://doi.org/10.1016/0021-9517(83)90010-6.

(100) Walton, A. S.; Lauritsen, J. V.; Topsøe, H.; Besenbacher, F. MoS2 Nanoparticle Morphologies in Hydrodesulfurization Catalysis Studied by Scanning Tunneling Microscopy. *J. Catal.* **2013**, *308*, 306–318. https://doi.org/10.1016/j.jcat.2013.08.017.

(101) Kibsgaard, J.; Tuxen, A.; Knudsen, K. G.; Brorson, M.; Topsøe, H.; Lægsgaard, E.; Lauritsen, J. V.; Besenbacher, F. Comparative Atomic-Scale Analysis of Promotional Effects by Late 3d-Transition Metals in MoS_2 Hydrotreating Catalysts. *J. Catal.* **2010**, *272* (2), 195–203. https://doi.org/10.1016/j.jcat.2010.03.018.

(102) Deepak, F. L.; Esparza, R.; Borges, B.; Lopez-Lozano, X.; Jose-Yacaman, M. Direct Imaging and Identification of Individual Dopant Atoms in MoS_2 and WS_2 Catalysts by Aberration Corrected Scanning Transmission Electron Microscopy. *ACS Catal.* **2011**, *1* (5), 537–543. https://doi.org/10.1021/cs100141p.

(103) Ramos, M.; Torres, B.; Bahena, D.; José-Yacamán, M.; Alvarez-Contreras, L.; Chianelli, R. R. Structural Aspects of Ternary Phase Ni/$MoWS_2$ Catalyst: An Aberration Corrected HRTEM Study. *Mater. Res. Soc. Symp. Proc.* **2013**, *1548*, 19–23. https://doi.org/10.1557/opl.2013.1076.

(104) Shi, Y.; Zhou, Y.; Yang, D. R.; Xu, W. X.; Wang, C.; Wang, F. Bin; Xu, J. J.; Xia, X. H.; Chen, H. Y. Energy Level Engineering of MoS_2 by Transition-Metal Doping for Accelerating Hydrogen Evolution Reaction. *J. Am. Chem. Soc.* **2017**, *139* (43), 15479–15485. https://doi.org/10.1021/jacs.7b08881.

(105) Gong, Y.; Liu, Z.; Lupini, A. R.; Shi, G.; Lin, J.; Najmaei, S.; Lin, Z.; Elías, A. L.; Berkdemir, A.; You, G.; Terrones, H.; Terrones, M.; Vajtai, R.; Pantelides, S. T.; Pennycook, S. J.; Lou, J.; Zhou, W.; Ajayan, P. M. Band Gap Engineering and Layer-by-Layer Mapping of Selenium-Doped Molybdenum Disulfide. *Nano Lett.* **2014**, *14* (2), 442–449. https://doi.org/10.1021/nl4032296.

(106) Yang, L.; Majumdar, K.; Liu, H.; Du, Y.; Wu, H.; Hatzistergos, M.; Hung, P. Y.; Tieckelmann, R.; Tsai, W.; Hobbs, C.; Ye, P. D. Chloride Molecular Doping Technique on

2D Materials: WS_2 and MoS_2. *Nano Lett.* **2014**, *14* (11), 6275–6280. https://doi.org/10.1021/nl502603d.

(107) Mouri, S.; Miyauchi, Y.; Matsuda, K. Tunable Photoluminescence of Monolayer MoS_2 via Chemical Doping. *Nano Lett.* **2013**, *13* (12), 5944–5948. https://doi.org/10.1021/nl403036h.

(108) Laskar, M. R.; Nath, D. N.; Ma, L.; Lee, E. W.; Lee, C. H.; Kent, T.; Yang, Z.; Mishra, R.; Roldan, M. A.; Idrobo, J. C.; Pantelides, S. T.; Pennycook, S. J.; Myers, R. C.; Wu, Y.; Rajan, S. P-Type Doping of MoS_2 Thin Films Using Nb. *Appl. Phys. Lett.* **2014**, *104* (9), 092104. https://doi.org/10.1063/1.4867197.

(109) Zhang, K.; Feng, S.; Wang, J.; Azcatl, A.; Lu, N.; Addou, R.; Wang, N.; Zhou, C.; Lerach, J.; Bojan, V.; Kim, M. J.; Chen, L. Q.; Wallace, R. M.; Terrones, M.; Zhu, J.; Robinson, J. A. Manganese Doping of Monolayer MoS_2 : The Substrate Is Critical. *Nano Lett.* **2015**, *15* (10), 6586–6591. https://doi.org/10.1021/acs.nanolett.5b02315.

(110) Fremes, S. E.; Furukawa, R. D.; Li, R. K.; Weisel, R. D.; Mickle, D. A. G.; Tumiati, L. C. Prolonged Preservation with University of Wisconsin Solution. *J. Surg. Res.* **1991**, *50* (4), 330–334. https://doi.org/10.1016/0022-4804(91)90199-V.

(111) Salitra, G.; Hodes, G.; Klein, E.; Tenne, R. Highly Oriented WSe2 Thin Films Prepared by Selenization of Evaporated WO_3. *Thin Solid Films* **1994**, *245* (1–2), 180–185. https://doi.org/10.1016/0040-6090(94)90896-6.

(112) Gourmelon, E.; Hadouda, H.; Bernede, J. C.; Pouzet, J. High Quality Crystalline MoS_2 Thin Films Obtained on Ni Coated Substrates: Optimization of the Post-Annealing Treatment. *Vacuum* **1997**, *48* (6), 509–514. https://doi.org/10.1016/s0042-207x(97)00025-0.

(113) Sun, H.; Ang, H. M.; Tadé, M. O.; Wang, S. Co_3O_4 Nanocrystals with Predominantly Exposed Facets: Synthesis, Environmental and Energy Applications. *J. Mater. Chem. A* **2013**, *1* (46), 14427–14442. https://doi.org/10.1039/c3ta12960h.

(114) Brunken, S.; Mientus, R.; Ellmer, K. Metal-Sulfide Assisted Rapid Crystallization of Highly (001)-Textured Tungsten Disulphide (WS_2) Films on Metallic Back Contacts. *Phys. Status Solidi Appl. Mater. Sci.* **2012**, *209* (2), 317–322. https://doi.org/10.1002/pssa.201127524.

(115) Ellmer, K.; Seeger, S.; Mientus, R. Rapid Crystallization of WS_2 Films Assisted by a Thin Nickel Layer: An *in situ* Energy-Dispersive X-Ray Diffraction Study. *Phys. Status Solidi Appl. Mater. Sci.* **2006**, *203* (10), 2457–2462. https://doi.org/10.1002/pssa.200622016.

(116) Sang, X.; Li, X.; Zhao, W.; Dong, J.; Rouleau, C. M.; Geohegan, D. B.; Ding, F.; Xiao, K.; Unocic, R. R. *In situ* Edge Engineering in Two-Dimensional Transition Metal Dichalcogenides. *Nat. Commun.* **2018**, *9* (1), 1–7. https://doi.org/10.1038/s41467-018-04435-x.

(117) Chen, Q.; Li, H.; Xu, W.; Wang, S.; Sawada, H.; Allen, C. S.; Kirkland, A. I.; Grossman, J. C.; Warner, J. H. Atomically Flat Zigzag Edges in Monolayer MoS_2 by Thermal Annealing. *Nano Lett.* **2017**, *17* (9), 5502–5507. https://doi.org/10.1021/acs.nanolett.7b02192.

(118) Chen, J.; Zhou, S.; Wen, Y.; Ryu, G. H.; Allen, C.; Lu, Y.; Kirkland, A. I.; Warner, J. H. *In situ* High Temperature Atomic Level Dynamics of Large Inversion Domain Formations in

Monolayer MoS_2. *Nanoscale* **2019**, *11* (4), 1901–1913. https://doi.org/10.1039/c8nr08821g.

(119) Fei, L.; Lei, S.; Zhang, W. B.; Lu, W.; Lin, Z.; Lam, C. H.; Chai, Y.; Wang, Y. Direct TEM Observations of Growth Mechanisms of Two-Dimensional MoS≠ Flakes. *Nat. Commun.* **2016**, *7* (1), 1–7. https://doi.org/10.1038/ncomms12206.

(120) Sang, X.; Li, X.; Geohegan, D. B.; Xiao, K.; Unocic, R. Atomistic Insights into Thermolysis and Growth of Two-Dimensional MoS≠ Using *In situ* Electron Microscopy. *Microsc. Microanal.* **2018**, *24* (S1), 1568–1569. https://doi.org/10.1017/s1431927618008322.

(121) Bayer, B. C.; Kaindl, R.; Monazam, M. R. A.; Susi, T.; Kotakoski, J.; Gupta, T.; Eder, D.; Waldhauser, W.; Meyer, J. C. Atomic-Scale *in situ* Observations of Crystallization and Restructuring Processes in Two-Dimensional MoS≠ Films. *ACS Nano* **2018**, *12* (8), 8758–8769. https://doi.org/10.1021/acsnano.8b04945.

(122) Hansen, L. P.; Johnson, E.; Brorson, M.; Helveg, S. Growth Mechanism for Single- and Multi-Layer MoS≠ Nanocrystals. *J. Phys. Chem. C* **2014**, *118* (39), 22768–22773. https://doi.org/10.1021/jp5069279.

(123) Wang, H. W.; Skeldon, P.; Thompson, G. E.; Wood, G. C. Synthesis and Characterization of Molybdenum Disulphide Formed from Ammonium Tetrathiomolybdate. *J. Mater. Sci.* **1997**, *32* (2), 497–502. https://doi.org/10.1023/A:1018538424373.

(124) Prasad, T.; Diemann, E.; Nuclear, A. M.-J. of I. and; 1973, undefined. Thermal Decomposition of $(NH_4)_2MoO_2S_2$, $(NH_4)_2MoS_4$, $(NH_4)_2WO_2S_2$ and $(NH_4)_2WS_4$. *Elsevier*.

(125) Liu, K. K.; Zhang, W.; Lee, Y. H.; Lin, Y. C.; Chang, M. T.; Su, C. Y.; Chang, C. S.; Li, H.; Shi, Y.; Zhang, H.; Lai, C. S.; Li, L. J. Growth of Large-Area and Highly Crystalline MoS_2 Thin Layers on Insulating Substrates. *Nano Lett.* **2012**, *12* (3), 1538–1544. https://doi.org/10.1021/nl2043612.

(126) Yang, J.; Gu, Y.; Lee, E.; Lee, H.; Park, S. H.; Cho, M. H.; Kim, Y. H.; Kim, Y. H.; Kim, H. Wafer-Scale Synthesis of Thickness-Controllable MoS_2 Films via Solution-Processing Using a Dimethylformamide/n-Butylamine/2-Aminoethanol Solvent System. *Nanoscale* **2015**, *7* (20), 9311–9319. https://doi.org/10.1039/c5nr01486g.

(127) George, A. S.; Mutlu, Z.; Ionescu, R.; Wu, R. J.; Jeong, J. S.; Bay, H. H.; Chai, Y.; Mkhoyan, K. A.; Ozkan, M.; Ozkan, C. S. Wafer Scale Synthesis and High Resolution Structural Characterization of Atomically Thin MoS_2 Layers. *Adv. Funct. Mater.* **2014**, *24* (47), 7461–7466. https://doi.org/10.1002/adfm.201402519.

(128) Kondekar, N.; Boebinger, M. G.; Tian, M.; Kirmani, M. H.; McDowell, M. T. The Effect of Nickel on MoS_2 Growth Revealed with *in situ* Transmission Electron Microscopy. *ACS Nano* **2019**, *13* (6), 7117–7126. https://doi.org/10.1021/acsnano.9b02528.

(129) Feltham, P. On Grain Growth in Metals. *Scr. Metall.* **1969**, *3* (11), 853–854. https://doi.org/10.1016/0036-9748(69)90194-X.

(130) Brorson, M.; Carlsson, A.; Topsøe, H. The Morphology of MoS_2, WS_2, Co-Mo-S, Ni-Mo-S and Ni-W-S Nanoclusters in Hydrodesulfurization Catalysts Revealed by HAADF-STEM. *Catal. Today* **2007**, *123* (1–4), 31–36. https://doi.org/10.1016/j.cattod.2007.01.073.

(131) Byskov, L. S.; Nørskov, J. K.; Clausen, B. S.; Topsøe, H. DFT Calculations of Unpromoted

and Promoted MoS_2-Based Hydrodesulfurization Catalysts. *J. Catal.* **1999**, *187* (1), 109–122. https://doi.org/10.1006/jcat.1999.2598.

(132) Krebs, E.; Silvi, B.; Raybaud, P. Mixed Sites and Promoter Segregation: A DFT Study of the Manifestation of Le Chatelier's Principle for the Co(Ni)MoS Active Phase in Reaction Conditions. *Catal. Today* **2008**, *130* (1), 160–169. https://doi.org/10.1016/j.cattod.2007.06.081.

(133) Ponomarev, E. A.; Tenne, R.; Katty, A.; Lévy-Clément, C. Highly Oriented Photoactive Polycrystalline MoS_2 Layers Obtained by van Der Waals Rheotaxy Technique from Electrochemically Deposited Thin Films. *Sol. Energy Mater. Sol. Cells* **1998**, *52* (1–2), 125–133. https://doi.org/10.1016/S0927-0248(97)00277-8.

(134) Ballif, C.; Regula, M.; Schmid, P. E.; Remškar, M.; Sanjinés, R.; Lévy, F. Preparation and Characterization of Highly Oriented, Photoconducting WS_2 Thin Films. *Appl. Phys. A Mater. Sci. Process.* **1996**, *62* (6), 543–546. https://doi.org/10.1007/s003390050338.

(135) Regula, M.; Ballif, C.; Moser, J. H.; Lévy, F. Structural, Chemical, and Electrical Characterisation of Reactively Sputtered WS_x Thin Films. *Thin Solid Films* **1996**, *280* (1–2), 67–75. https://doi.org/10.1016/0040-6090(95)08206-9.

(136) Tsirlina, T.; Cohen, S.; Cohen, H.; Sapir, L.; Peisach, M.; Tenne, R.; Matthaeus, A.; Tiefenbacher, S.; Jaegermann, W.; Ponomarev, E. A.; Lévy-Clément, C. Growth of Crystalline WSe_2 and WS_2 Films on Amorphous Substrate by Reactive (Van Der Waals) Rheotaxy. *Sol. Energy Mater. Sol. Cells* **1996**, *44* (4), 457–470. https://doi.org/10.1016/S0927-0248(96)00048-7.

(137) Ennaoui, A.; Fiechter, S.; Ellmer, K.; Scheer, R.; Diesner, K. Preparation of Textured and Photoactive 2H-WS_2 Thin Films by Sulfurization of WO3. *Thin Solid Films* **1995**, *261* (1–2), 124–131. https://doi.org/10.1016/S0040-6090(95)06524-5.

(138) Caissel, J. *[Vesico-Sigmoid Fistula after Partial Cystectomy, for Vesical Tumor, Followed by Betatron Irradiation]*., 1987th ed.; Massalski, T. B., Murray, J. L., Bennett, L. H., Baker, H., Kacprzak, L., Eds.; Ohio, 1971; Vol. 77.

(139) Nast, O.; Puzzer, T.; Koschier, L. M.; Sproul, A. B.; Wenham, S. R. Aluminum-Induced Crystallization of Amorphous Silicon on Glass Substrates above and below the Eutectic Temperature. *Appl. Phys. Lett.* **1998**, *73* (22), 3214–3216. https://doi.org/10.1063/1.122722.

(140) Ashtikar, M. S.; Sharma, G. L. Silicide Mediated Low Temperature Crystallization of Hydrogenated Amorphous Silicon in Contact with Aluminum. *J. Appl. Phys.* **1995**, *78* (2), 913–918. https://doi.org/10.1063/1.360722.

(141) Garcia, A.; Raya, A. M.; Mariscal, M. M.; Esparza, R.; Herrera, M.; Molina, S. I.; Scavello, G.; Galindo, P. L.; Jose-Yacaman, M.; Ponce, A. Analysis of Electron Beam Damage of Exfoliated MoS_2 Sheets and Quantitative HAADF-STEM Imaging. *Ultramicroscopy* **2014**, *146*, 33–38. https://doi.org/10.1016/j.ultramic.2014.05.004.

(142) Zan, R.; Ramasse, Q. M.; Jalil, R.; Georgiou, T.; Bangert, U.; Novoselov, K. S. Control of Radiation Damage in MoS_2 by Graphene Encapsulation. *ACS Nano* **2013**, *7* (11), 10167–10174. https://doi.org/10.1021/nn4044035.

(143) Algara-Siller, G.; Kurasch, S.; Sedighi, M.; Lehtinen, O.; Kaiser, U. The Pristine Atomic Structure of MoS_2 Monolayer Protected from Electron Radiation Damage by Graphene. *Appl. Phys. Lett.* **2013**, *103* (20), 203107. https://doi.org/10.1063/1.4830036.

(144) Cui, W.; Ge, C.; Xing, Z.; Asiri, A. M.; Sun, X. Ni_xS_y-MoS_2 Hybrid Microspheres: One-Pot Hydrothermal Synthesis and Their Application as a Novel Hydrogen Evolution Reaction Electrocatalyst with Enhanced Activity. *Electrochim. Acta* **2014**, *137*, 504–510. https://doi.org/10.1016/j.electacta.2014.06.035.

(145) Yoosuk, B.; Kim, J. H.; Song, C.; Ngamcharussrivichai, C.; Prasassarakich, P. Highly Active MoS_2, $CoMoS_2$ and $NiMoS_2$ Unsupported Catalysts Prepared by Hydrothermal Synthesis for Hydrodesulfurization of 4,6-Dimethyldibenzothiophene. *Catal. Today* **2008**, *130* (1), 14–23. https://doi.org/10.1016/j.cattod.2007.07.003.

(146) Hansen, L. P.; Ramasse, Q. M.; Kisielowski, C.; Brorson, M.; Johnson, E.; Topsøe, H.; Helveg, S. Atomic-Scale Edge Structures on Industrial-Style MoS_2 Nanocatalysts. *Angew. Chemie - Int. Ed.* **2011**, *50* (43), 10153–10156. https://doi.org/10.1002/anie.201103745.

(147) Miseikis, V.; Bianco, F.; David, J.; Gemmi, M.; Pellegrini, V.; Romagnoli, M.; Coletti, C. Deterministic Patterned Growth of High-Mobility Large-Crystal Graphene: A Path towards Wafer Scale Integration. *2D Mater.* **2017**, *4* (2). https://doi.org/10.1088/2053-1583/aa5481.

(148) Su, G.; Hadjiev, V. G.; Loya, P. E.; Zhang, J.; Lei, S.; Maharjan, S.; Dong, P.; M. Ajayan, P.; Lou, J.; Peng, H. Chemical Vapor Deposition of Thin Crystals of Layered Semiconductor SnS_2 for Fast Photodetection Application. *Nano Lett.* **2015**, *15* (1), 506–513. https://doi.org/10.1021/nl503857r.

(149) Sun, D.; Nguyen, A. E.; Barroso, D.; Zhang, X.; Preciado, E.; Bobek, S.; Klee, V.; Mann, J.; Bartels, L. Chemical Vapor Deposition Growth of a Periodic Array of Single-Layer MoS_2 Islands via Lithographic Patterning of an SiO_2/Si Substrate. *2D Mater.* **2015**, *2* (4), 045014. https://doi.org/10.1088/2053-1583/2/4/045014.

(150) Yu, Q.; Jauregui, L. A.; Wu, W.; Colby, R.; Tian, J.; Su, Z.; Cao, H.; Liu, Z.; Pandey, D.; Wei, D.; Chung, T. F.; Peng, P.; Guisinger, N. P.; Stach, E. A.; Bao, J.; Pei, S. S.; Chen, Y. P. Control and Characterization of Individual Grains and Grain Boundaries in Graphene Grown by Chemical Vapour Deposition. *Nat. Mater.* **2011**, *10* (6), 443–449. https://doi.org/10.1038/nmat3010.

(151) Wu, W.; Jauregui, L. A.; Su, Z.; Liu, Z.; Bao, J.; Chen, Y. P.; Yu, Q. Growth of Single Crystal Graphene Arrays by Locally Controlling Nucleation on Polycrystalline Cu Using Chemical Vapor Deposition. *Adv. Mater.* **2011**, *23* (42), 4898–4903. https://doi.org/10.1002/adma.201102456.

(152) Li, Y.; Hao, S.; Distefano, J. G.; Murthy, A. A.; Hanson, E. D.; Xu, Y.; Wolverton, C.; Chen, X.; Dravid, V. P. Site-Specific Positioning and Patterning of MoS_2 Monolayers: The Role of Au Seeding. *ACS Nano* **2018**, *12* (9), 8970–8976. https://doi.org/10.1021/acsnano.8b02409.

(153) Lee, Y.-H.; Zhang, X.-Q.; Zhang, W.; Chang, M.-T.; Lin, C.-T.; Chang, K.-D.; Yu, Y.-C.; Wang, J. T.-W.; Chang, C.-S.; Li, L.-J.; Lin, T.-W. Synthesis of Large-Area MoS_2 Atomic Layers with Chemical Vapor Deposition. *Adv. Mater.* **2012**, *24* (17), 2320–2325. https://doi.org/10.1002/adma.201104798.

(154) Patsha, A.; Sheff, V.; Ismach, A. Seeded-Growth of WS_2 Atomic Layers: The Effect on Chemical and Optical Properties. *Nanoscale* **2019**, *11* (46), 22493–22503. https://doi.org/10.1039/c9nr06515f.

(155) Radovsky, G.; Shalev, T.; Ismach, A. Tuning the Morphology and Chemical Composition of MoS_2 Nanostructures. *J. Mater. Sci.* **2019**, *54* (10), 7768–7779. https://doi.org/10.1007/s10853-019-03437-4.

(156) Najmaei, S.; Liu, Z.; Zhou, W.; Zou, X.; Shi, G.; Lei, S.; Yakobson, B. I.; Idrobo, J. C.; Ajayan, P. M.; Lou, J. Vapour Phase Growth and Grain Boundary Structure of Molybdenum Disulphide Atomic Layers. *Nat. Mater.* **2013**, *12* (8), 754–759. https://doi.org/10.1038/nmat3673.

(157) Yun, S. J.; Chae, S. H.; Kim, H.; Park, J. C.; Park, J. H.; Han, G. H.; Lee, J. S.; Kim, S. M.; Oh, H. M.; Seok, J.; Jeong, M. S.; Kim, K. K.; Lee, Y. H. Synthesis of Centimeter-Scale Monolayer Tungsten Disulfide Film on Gold Foils. *ACS Nano* **2015**, *9* (5), 5510–5519. https://doi.org/10.1021/acsnano.5b01529.

(158) Bersch, B. M.; Eichfeld, S. M.; Lin, Y.-C.; Zhang, K.; Bhimanapati, G. R.; Piasecki, A. F.; III, M. L.; Robinson, J. A. Selective-Area Growth and Controlled Substrate Coupling of Transition Metal Dichalcogenides. *2D Mater.* **2017**, *4* (2), 025083. https://doi.org/10.1088/2053-1583/AA6BEB.

(159) Wang, Z.; Huang, Q.; Chen, P.; Guo, S.; Liu, X.; Liang, X.; Wang, L. Metal Induced Growth of Transition Metal Dichalcogenides at Controlled Locations. *Sci. Rep.* **2016**, *6* (1), 1–7. https://doi.org/10.1038/srep38394.

(160) Cain, J. D.; Shi, F.; Wu, J.; Dravid, V. P. Growth Mechanism of Transition Metal Dichalcogenide Monolayers: The Role of Self-Seeding Fullerene Nuclei. *ACS Nano* **2016**, *10* (5), 5440–5445. https://doi.org/10.1021/acsnano.6b01705.

(161) D.A. Poster; K.E Easterling. Precipitation Growth. In *Phase Transformations in Metals and Alloys*; Chapman & Hall, 1992; p 281.

(162) Ling, X.; Lee, Y. H.; Lin, Y.; Fang, W.; Yu, L.; Dresselhaus, M. S.; Kong, J. Role of the Seeding Promoter in MoS_2 Growth by Chemical Vapor Deposition. *Nano Lett.* **2014**, *14* (2), 464–472. https://doi.org/10.1021/nl4033704.

(163) Shi, Y.; Zhou, W.; Lu, A. Y.; Fang, W.; Lee, Y. H.; Hsu, A. L.; Kim, S. M.; Kim, K. K.; Yang, H. Y.; Li, L. J.; Idrobo, J. C.; Kong, J. Van Der Waals Epitaxy of MoS_2 Layers Using Graphene as Growth Templates. *Nano Lett.* **2012**, *12* (6), 2784–2791. https://doi.org/10.1021/nl204562j.

(164) Koma, A.; Sunouchi, K.; Miyajima, T. Fabrication and Characterization of Heterostructures with Subnanometer Thickness. *Microelectron. Eng.* **1984**, *2* (1–3), 129–136. https://doi.org/10.1016/0167-9317(84)90057-1.

(165) Saiki, K.; Ueno, K.; Shimada, T.; Koma, A. Application of Van Der Waals Epitaxy to Highly Heterogeneous Systems. *J. Cryst. Growth* **1989**, *95* (1–4), 603–606. https://doi.org/10.1016/0022-0248(89)90475-2.

(166) Jaegermann, W.; Klein, A.; Pettenkofer, C. Electronic Properties of Van Der Waals-Epitaxy Films and Interfaces. *Electron Spectroscopies Applied to Low-Dimensional Materials.*

2002, 317–402. https://doi.org/10.1007/0-306-47126-4_7.

(167) Galun, E.; Cohen, H.; Margulis, L.; Vilan, A.; Tsirlina, T.; Hodes, G.; Tenne, R.; Hershfinkel, M.; Jaegermann, W.; Ellmer, K. Crystallization of Layered Metal-Dichalcogenides Films on Amorphous Substrates. *Appl. Phys. Lett.* **1995**, *67*, 3474. https://doi.org/10.1063/1.115251.

(168) Kim, S. J.; Kwon, O.; Kim, D. W.; Kim, J.; Jung, H. T. Influence of Graphene Thickness and Grain Boundaries on MoS_2 Wrinkle Nanostructures. *Phys. Chem. Chem. Phys.* **2018**, *20* (25), 17000–17008. https://doi.org/10.1039/c8cp02460j.

(169) Thompson, A.H. Method of making titanium disulfide. **1978** U.S. Patent 4,069,301.